THE UNIVERSITY OF CHICAGO

ENVIRONMENTAL EFFECTS ON ULTRAFAST ELECTRONIC DYNAMICS IN BIOLOGICAL AND SYNTHETIC LIGHT HARVESTING

A DISSERTATION SUBMITTED TO
THE FACULTY OF THE DIVISION OF THE PHYSICAL SCIENCES
IN CANDIDACY FOR THE DEGREE OF
DOCTOR OF PHILOSOPHY

DEPARTMENT OF CHEMISTRY

BY
JOHN P. OTTO

CHICAGO, ILLINOIS
JUNE 2018

To my infinitely supportive parents and siblings

TABLE OF CONTENTS

LIST OF FIGURES

LIST OF TABLES

ACKNOWLEDGMENTS

I would like to thank my thesis committee, Profs. Andrei Tokmakoff and Bozhi Tian, and in particular my advisor, Prof. Greg Engel. Greg, you have led me to be a far better scientist than I could have been on my own, and the research presented in this dissertation would not have been possible without your continued advice and support. Thank you.

My path through graduate school was made easier by the great example provided by the senior students I worked with. Lili Wang taught me how to be picky enough to get the instruments working correctly. Moira Flanagan, Pete Dahlberg, and Ved Singh all set a high bar to live up to as a member of the Engel group.

I've greatly enjoyed being able to work with a number of postdocs in the group. Marco Allodi was extremely helpful on the FMO project and has been a wonderful source of advice on navigating grad school. Brian Rolczynski has been an unfailing source of positivity in the face of my complaining, for which I owe him a great deal. I would be remiss to not also thank Cheng "Wave" Wang and Graham Griffin for their help along the way.

I am lucky to have started my graduate career in the Engel group with three outstanding students, Sara Massey, Nick Williams and Po-Chieh Ting. Working alongside the three of you for the past five years has been an experience I am unlikely to ever forget, and one I certainly won't regret.

The other members of the Engel group I've worked with have contributed in many ways to making my time here both productive and enjoyable. In no particular order, I'd like to thank Ryan, Richard, Sara, Sarah, Polina, Lawson, Jake, Elizabeth, Shu Hao, Haibin, Subha, Hunter, Kirk, Graham N., Lane, Karen, Brenda, and Pegg for their roles in making the Engel group the place that it is.

Through the course of my graduate work, I have had a number of wonderful collaborators. Rafael Saer and Bob Blankenship were very helpful on the FMO project, and think I can safely say that I learned most of what I know about photosynthesis from Bob's textbook. On the cavitand project, Igor Pochorovsi, Zhenan Bao, Sam Blau and Alan Aspuru Guzik

were all vital, and Melanie Chiu deserves special thanks for helping to push that through to publication. I have had the pleasure of working with Paul Cunningham and Joe Melinger from the Naval Research Lab on the DNA project, and should thank the Vannevar Bush Faculty Fellowship and the Laboratory University Collaboration Initiative for enabling that connection.

My undergraduate research advisor, Dr. Brad Parsons, deserves thanks for pointing me in the direction of nonlinear spectroscopy and for encouraging me to attend grad school in the first place.

I have made a number of great friends while in Chicago, without whom I never would have made it this far. Tom Kuntz, Dan Reid, Mzuri Handlin, Nicole James and Dmitriy Dolzhnikov all deserve special thanks. I hope I can be the positive influence in your lives that you have been in mine.

Finally, none of this would have been possible were it not for the decades of support and encouragement from my parents and siblings. Mom, Dad, Paul (+Liz) and Hannah, I would never have dreamed of being where I am today were it not for you.

ABSTRACT

The world's energy requirements are always increasing, but sunlight provides more than sufficient energy to sustain humanity's energetic needs for decades to come. In developing future generations of light harvesting materials, scientists can turn to biology to provide design rules for efficient and robust methods of converting sunlight to address these requirements. Photosynthetic antenna complexes demonstrate remarkable efficiency and resilience, including capabilities to regulate light harvesting activity in the presence of hazards such as oxidizing agents. Through control of the environment surrounding chromophores, these complexes exercise incredible control of electronic dynamics to a level not yet achievable in manmade systems. In this dissertation I investigate biological and manmade approaches to controlling electronic dynamics via external processes on the scaffolds that hold chromophores in place. These investigations use two-dimensional electronic spectroscopy to correlate excitation energy with emission and absorption at later times as a probe of electronic couplings and dynamics on the femtosecond to nanosecond timescale. In the course of this study, I identify a potential redox protection mechanism in the Fenna-Matthews-Olson light harvesting complex arising from a structural motif repurposed from redox enzymes. Moving to synthetic light harvesting structures, I observe how nuclear motion can limit energy transfer outside the bounds predicted by Förster theory in a temperature-controlled resorcin[4]arene molecular switch. In a study of vibronically coupled cyanine dimers bound to DNA, I found evidence for multi-mode vibrational coupling that may lead to new paths for efficient energy transfer, and I propose new experiments making use of DNA nanostructures to explore this area further. Combined, these observations will lead to new designs for light harvesting materials that can help to meet future energy generation requirements.

CHAPTER 1

INTRODUCTION

1.1 Overview

The total human energy expenditure as of 2011 was 15 TW [1], with projected use of around 45 TW by 2100 [2]. By comparison, the earth receives as much as 120,000 TW at any given time from the sun. As we look to develop methods for harnessing this energy, scientists can take cues from existing approaches to fast track the design process. Photosynthetic organisms have a variety of light harvesting motifs that we can learn from, and photosynthesis accounts for a total solar energy use of 130 TW, 5 TW of which is on land [1]. The initial steps of light harvesting in photosynthesis take place largely in pigment-protein complexes—protein structures that hold chlorophyll and other chromophores in fixed orientations, leading to coupling and energy transfer beyond what would occur were the molecules simply in solution [3]. In these complexes, it is the chemical environment surrounding chromophores (sometimes referred to as the "bath" in contrast to the chromophore "system") that drive electronic dynamics. Understanding this interaction is the focus of my research.

By understanding the role of environmental effects on electronic dynamics, I hope to inform the design of future synthetic light harvesting systems. Future designs based on this understanding will avoid unwanted competition from vibrational relaxation processes and provide a path towards regulating energy transfer through the use of the molecular environment surrounding chromophores. This work involves study both of biomolecules and synthetic systems intended to replicate various parameters present in biological systems. This introductory chapter provides background information on the light harvesting step of photosynthesis from a physical chemistry perspective, as well as spectroscopic background necessary as prerequisite material to the later chapters. Chapter 2 describes the study of a potential redox regulation mechanism in the Fenna-Matthews-Olson pigment-protein complex from the green sulfur bacterium *Chlorobium tepidum*. Chapter 3 discusses vibronic

dynamics of BODIPY-based dyes attached to a temperature-controlled cavitand molecular switch, specifically investigating how vibrational dynamics interact with electronic energy transfer. Chapter 4 investigates vibronic coupling in an H-type DNA-bound cyanine homodimer. Chapter 5 describes a future directions proposal and is followed by an overall conclusion that summarizes the lessons learned in the course of these studies.

1.2 Theoretical Descriptions of Energy Transfer

One of the simplest descriptions of electronic interactions between molecules is through the point dipole approximation. This approach approximates each molecule in terms of a vector, which describes the change in charge density between one electronic state and another (the "transition dipole"). Interactions between molecules in this formalism are determined by the relative distance and orientation of these transition dipoles. Energy transfer that takes place through this coupling is known as Förster resonance energy transfer (FRET) [4, 5]. In general, the transfer rate from chromophore A to chromophore B can be described by Fermi's golden rule,

$$k_{AB} \propto |\langle \psi'_A \psi_B | V | \psi_A \psi'_B \rangle|^2 \tag{1.1}$$

Where ψ'_i describes the excited state of chromophore i and the coupling, V, is the coupling between the transition dipoles of chromophores A and B,

$$V = \frac{1}{R^3}[\hat{\mu}_A \cdot \hat{\mu}_B - 3(\hat{\mu}_A \cdot \mathbf{u}_R)(\hat{\mu}_B \cdot \mathbf{u}_R)] \tag{1.2}$$

Where $\hat{\mu}_i$ is the dipole operator on chromophore i and $\mathbf{u}_R$ is the unit vector in the direction that connects the two chromophores. Combined with Fermi's golden rule, this coupling leads to the $k_{AB} \propto \frac{1}{R^6}$ rate dependence for which FRET is known [6]. The second-order perturbative description of the electronic dipole coupling described by Förster theory describes energy transfer dynamics on the several nanometer scale well, but breaks down under short distances and stronger interchromophore coupling.

When chromophores are held with some rigidity in close enough proximity to one another, they are at times better described by delocalized electronic states (made from a linear combination of molecular states) rather than as truly independent chromophores. Relaxation between these delocalized states can be described via Redfield theory [7], originally used to describe the coupling of spins in nuclear magnetic resonance (NMR) spectroscopy. Given delocalized excited states of the form $|M\rangle = \sum_m c_m^{(M)} |m\rangle$, where the delocalized state is a linear combination of localized states $|m\rangle$, relaxation between states $|M\rangle$ and $|N\rangle$ has the rate

$$k_{M\to N} = 2\gamma_{MN}\tilde{C}^{(re)}(\omega_{MN}) \tag{1.3}$$

where $\omega_{MN} = \frac{\mathcal{E}_M - \mathcal{E}_N}{\hbar}$ describes the energy mismatch between states $|M\rangle$ and $|N\rangle$, γ_{MN} describes the spatial overlap of the delocalized states along with a measure of vibrational correlation

$$\gamma_{MN} = \sum_{m,n} e^{-R_{mn}/R_c} c_m^{(M)} c_m^{(N)} c_n^{(M)} c_n^{(N)} \tag{1.4}$$

and

$$\tilde{C}^{(re)}(\omega_{MN}) = \pi\omega^2\{[1 + n(\omega)]J(\omega) + n(-\omega)J(-\omega)\} \tag{1.5}$$

describes the interaction of the system with its surrounding environment (the protein, in the case of photosynthesis) based on the spectral density $J(\omega)$ and the Bose-Einstein distribution function $n(\omega) = \frac{1}{e^{\hbar\omega/kT}-1}$. $J(\omega < 0) = 0$.

Redfield theory uses a perturbative coupling to the surrounding environment (the "bath"), but in some cases this system-bath coupling must be treated more directly, in an approach called Modified Redfield Theory [8]. This theory has been used to describe excitation energy transfer through photosynthetic proteins such as the Fenna-Matthews-Olson complex and light harvesting complexes LH2 and LHCII [9]. A key point of the Redfield/Modified Redfield approach to describing energy transfer is the coherent, "wave-like" nature that leads to oscillatory dynamics in 2D spectra, such as those reported in [10]. More accurate theoretical representations of coherent and incoherent dynamics can be achieved using non-perturbative

approaches such as Heirarchical Equations of Motion (HEOM) [11].

1.3 Spectroscopic Methods

1.3.1 Abbreviated Theory of Third-Order Nonlinear Spectroscopy

Density Matrix Formalism

Spectroscopy is the study of light interacting with matter and is one of the most sensitive experimental probes of chemical and electronic dynamics available to science. The theory of spectroscopy[1]relies heavily on the quantum mechanics of molecules and (particularly in the condensed phase) *ensembles* of molecules. Individual molecules are best described in terms of wavefunctions, $|\Psi\rangle$, which are solutions to the Schrödinger equation

$$i\hbar\frac{\partial}{\partial t}|\Psi\rangle = \hat{H}|\Psi\rangle \tag{1.6}$$

where $\hat{H}$ describes the Hamiltonian, or energy operator. The overall wavefunction of a system can be described as the linear combination of a set of basis functions $|\psi_j\rangle$, i.e.

$$|\Psi\rangle = \sum_j p_j|\psi_j\rangle. \tag{1.7}$$

Strictly speaking, all chemical behavior can be derived from the wavefunction, but this quickly becomes intractable as one attempts to describe an ensemble of quantum systems instead of individual states. Instead, we describe our systems via a density matrix

$$\rho = \sum_{i,j} p_{ij}|\psi_i\rangle\langle\psi_j| \tag{1.8}$$

1 For a full description of the theory of nonlinear spectroscopy, refer to *Principles of Nonlinear Optical Spectroscopy* by Shaul Mukamel (Oxford University Press, 1995) [12]. A somewhat abbreviated version of the theory can also be found in *Concepts and Methods of 2D Infrared Spectroscopy* by Peter Hamm and Martin Zanni (Cambridge University Press, 2011) [13].

where the p_{ij} term describes the probability associated with the matrix element $|\psi_i\rangle\langle\psi_j|$. Along the diagonal, p_{jj} describes the probability of being in state j, equivalent to $|p_j|^2$ from equation 1.7. Accordingly, $\mathrm{Tr}[\rho] = 1$ for all systems. In the density matrix formalism, the Schrödinger equation is rewritten as the Liouville-Von Neumann equation

$$\frac{\partial}{\partial t}\rho = -\frac{i}{\hbar}[\hat{H}, \rho] \tag{1.9}$$

The density matrix has the advantage of being able to describe *mixed states* in addition to the *pure states* that are described by wavefunctions. A mixed state describes a system composed of a statistical ensemble of quantum states, where the expectation value of measured observables depend on the average of quantum observables. For a density matrix, expectation values for observables can be calculated simply by taking the trace, i.e.

$$\langle \hat{A} \rangle = Tr[\hat{A}\rho] \tag{1.10}$$

The density matrix is particularly useful in a system/bath approach, where one is only interested in certain states and degrees of freedom within a much larger ensemble. We can use a density matrix to describe the system of interest in detail while treating the bath more phenomenologically. This approach is useful for ensemble measurements such as spectroscopy, where the experiment directly measures transitions between exciton states (the system) that exist in a chemical environment that serves to perturb these states (the bath). Third-order spectroscopy allows the measurement not only of the energies of these states (accessible via linear spectroscopy) but also the degree of coupling between them, allowing for a reproduction of the density matrix experimentally.

Nonlinear Response Function

Two-dimensional spectroscopy measures the third order nonlinear polarization response ($P^{(3)}(t)$) of a given system, described by

$$P^{(3)}(t) \propto \int_0^\infty dt_3 \int_0^\infty dt_2 \int_0^\infty dt_1 \, E_3(t-t_3)E_2(t-t_3-t_2)E_1(t-t_3-t_2-t_1)R^{(3)}(t_3,t_2,t_1) \quad (1.11)$$

where E_i describes the time dependent electric field and $R^{(3)}(t_3,t_2,t_1)$ is the response function of the material. The response function is described by

$$\begin{aligned} R^{(3)}(t_3,t_2,t_1) &\propto i\langle\hat{\mu}(t_3+t_2+t_1)[\hat{\mu}(t_2+t_1),[\hat{\mu}(t_1)),[\hat{\mu}(0),\rho(-\infty)]]]\rangle \\ &= i\langle\hat{\mu_3}[\hat{\mu_2},[\hat{\mu_1})[\hat{\mu_0},\rho(-\infty)]]]\rangle \end{aligned} \quad (1.12)$$

where we operate on the density matrix with a dipole operator three times to produce the third-order response. By expanding the nested commutators

$$\begin{aligned} i\langle\hat{\mu_3}[\hat{\mu_2},[\hat{\mu_1})[\hat{\mu_0},\rho(-\infty)]]]\rangle = \\ & i\langle\hat{\mu_3}\hat{\mu_1}\rho(-\infty)\hat{\mu_0}\hat{\mu_2}\rangle - i\langle\hat{\mu_2}\hat{\mu_0}\rho(-\infty)\hat{\mu_1}\hat{\mu_3}\rangle \\ +i\langle\hat{\mu_3}\hat{\mu_2}\rho(-\infty)\hat{\mu_0}\hat{\mu_1}\rangle & - i\langle\hat{\mu_1}\hat{\mu_0}\rho(-\infty)\hat{\mu_2}\hat{\mu_3}\rangle \\ +i\langle\hat{\mu_3}\hat{\mu_0}\rho(-\infty)\hat{\mu_1}\hat{\mu_2}\rangle & - i\langle\hat{\mu_2}\hat{\mu_1}\rho(-\infty)\hat{\mu_0}\hat{\mu_3}\rangle \\ +i\langle\hat{\mu_3}\hat{\mu_2}\hat{\mu_1}\hat{\mu_0}\rho(-\infty)\rangle & - i\langle\rho(-\infty)\hat{\mu_0}\hat{\mu_1}\hat{\mu_2}\hat{\mu_3}\rangle \end{aligned} \quad (1.13)$$

we can see that the response function has four unique terms, each with a conjugate. Rather than keep track of these terms algebraically, it can be easier to understand the molecular response via double-sided Feynman diagrams, which contain the same information. To convert these equations into diagrams, we follow the following conventions [13]:

1. Time increases vertically, with initial states on the bottom and final states on top. Both the initial and final states must be a population (both sides of the density matrix

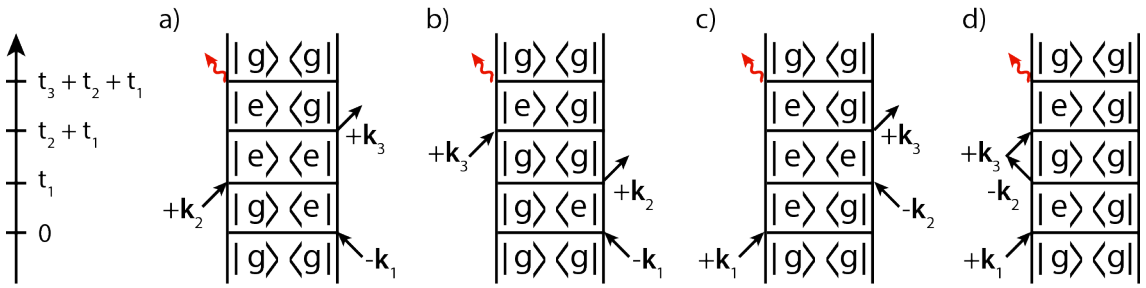

Figure 1.1: Feynman diagrams for a two-state system. Each diagram illustrates one pathway, with a-d corresponding to the left-hand terms in equation 1.13. The pathways shown are a) rephasing stimulated emission, b) rephasing ground state bleach, c) nonrephasing stimulated emission, and d) nonrephasing ground state bleach.

are the same) but the final state need not be the ground state for a valid diagram. The time between the first and second interaction (between 0 and t_1 on the time axis) is called *coherence time*. The second time delay is *waiting time* and the third is *rephasing time*.

2. All interactions with the light field are represented by arrows, with the final emission interaction (the signal) emitting to the top left.

3. Interactions from the right carry a minus sign, so the sign of the resulting signal is $(-1)^n$, where n is the number of arrows on the right side of the diagram.

4. The left vs. right direction of the arrow corresponds to positive vs negative frequencies, i.e. right pointing arrows represent a field oscillating as $e^{-i\omega t+ikr}$, while left pointing arrows epresent a field oscillating as $e^{+i\omega t-ikr}$. The frequency and wavevector of the emitted light (the last arrow) is the sum of the frequencies and wavevectors of the previous arrows.

5. Inward pointing arrows represent excitation of the corresponding ket or bra in the density matrix, while outward pointing arrows represent emission.

1.3.2 Two-Dimensional Electronic Spectroscopy

A study of the Feynman diagrams that correspond to 2D spectral signals tells us a great deal about the technique. The time-resolved nature of this description leads to the experimental requirement light pulses that are short on the timescale of relevant dynamics, in this case on the scale of femtoseconds. The Fourier relationship between time and frequency means that these light pulses must also be broad in frequency, which is useful for meeting the requirement of energetic resonance for transitions between states.important point is that the emitted field frequency and wavevector are the sum total of the frequency and wavevector from previous interactions, meaning that not only does the signal emit at a given frequency, but signals corresponding to the pathways of interest are emitted in a specific direction. Therefore, by controlling the input direction of the first three pulses (leading to the first three interactions with the signal) our emitted signal propagates in a fourth direction, not along any of the input beams. For this reason, 2D spectroscopy (in this configuration) is referred to as "background free."

It is critical to note that multiple Feynman diagrams will often contribute to the same location in the 2D spectrum, as shown in Figure 1.1, where all four signals relevant to a two-state system appear at the same location. The first diagram corresponds to a stimulated emission signal, where the sample is raised into its excited state and then emits back to the ground state. The second corresponds to ground state bleach, where absorption is reduced due to a depletion of ground state population. Both the first and second diagrams are known as "rephasing" pathways, because the coherent oscillations in the first and third time delays occur in opposite directions, leading to a photon echo. The third and fourth diagrams in Figure 1.1 show nonrephasing versions of stimulated emission and ground state bleach, where the first and third time delays feature oscillations propagating in the same direction, leading to a free induction decay rather than an echo. Experimentally, rephasing and nonrephasing pathways can be selected by controlling the order of incidence of the first two interactions, as indicated by the order of the left and right pointing arrows in the diagrams shown.

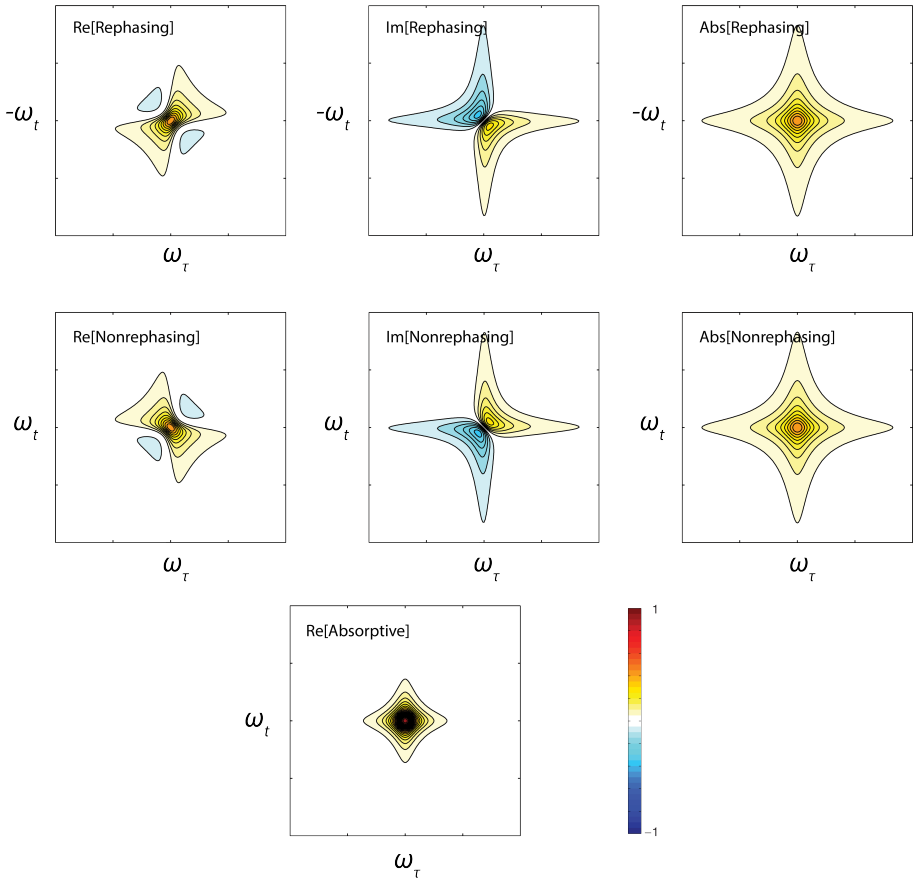

Figure 1.2: Rephasing, nonrephasing, and absorptive 2D spectral lineshapes. Based on a Lorentzian lineshape model described in [13]. Absorptive spectrum is the sum of rephasing and nonrephasing.

While information can be gained by measuring these pathways independently, they can be challenging to interpret as both contain elements of the absorptive and dispersive parts of the response function. Summing the real parts of the complex rephasing and nonrephasing signals creates the purely absorptive signal, which can be easier to interpret and allows for finer resolution, as shown in Figure 1.2.

The two dimensional spectrum shows the correlation between absorption at a given coherence frequency with absorption or emission at a given rephasing frequency after a delay corresponding to the waiting time, T. This correlation provides several pieces of information about the given sample or ensemble of samples. Features in the 2D spectrum are typically described as being on the diagonal (coherence and rephasing energy are the same) or as being

crosspeaks that are above ($\omega_t > \omega_\tau$) or below ($\omega_t < \omega_\tau$) the diagonal. Diagonal features tend to refer to single states, while crosspeaks indicate coupling or energy transfer. Analysis of how these features evolve across waiting time can lead to a map of how energy moves through a system, even in systems with sufficient states for multiple separate pathways to occur [14]. The shape of 2D spectral features inform on the relative influence of discrete subpopulations in the sample ensemble [15]. Static variation (i.e. permanent discrete subpopulations) leads to what is known as inhomogenous broadening, which causes elongation of a feature along the direction of the diagonal in 2D spectra. Spectral features lacking this elongation indicate that fluctuations in the environment lead to a loss of memory of the initial excitation, and this rounding out of the signal is referred to as homogenous broadening. In a homogeneously broadened sample, chromophores explore the distribution of the ensemble prior to being observed in rephasing time [6].

In addition to coupling and transfer between populations and subpopulations in a given sample ensemble, 2D spectroscopy can detect coherent dynamics, where the two sides of the density matrix describe different states. All signals in 2D spectroscopy rely on coherent oscillations in the coherence and rephasing times, but oscillatory dynamics in the waiting time provide a detailed probe of coupling beyond that provided by population dynamics [15]. Oscillations in the waiting time can be caused by coherences between different exciton states (i.e. purely electronic coherence) [10] or between vibronic states that have the same electronic state but different quanta of vibrational excitation [16]. One method of assigning oscillatory dynamics involves Fourier transformation of the entire complex spectral cube along the waiting time dimension, producing what is sometimes referred to as a 3D spectrum [17]. This 3D spectrum contains both positive and negative beating frequencies, which correspond to different Feynman diagrams. Importantly, rephasing and nonrephasing signals leading to positive and negative beating frequencies can occur in different places in the canonical coherence-rephasing 2D spectrum, allowing for assignment of oscillatory features in those locations to separate pathways corresponding to electronic dynamics or to ground or excited

state vibrational motion. More information regarding this approach to analyzing 2D spectra can be found in Chapter 4.

1.3.3 Experimental Approaches to 2D Electronic Spectroscopy

The light pulses used for all ultrafast methods described in this thesis begin in a modelocked Ti:Sapphire oscillator (Coherent Micra), which produces an 80 MHz train of transform-limited 60 nm FWHM pulses centered at 800-810 nm. These pulses are temporally stretched and sent into a regenerative amplifier (regen) cavity (another Ti:Sapphire crystal pumped by a powerful (20 W) 532 nm Q-switched, intracavitdy doubled Nd:YLF laser (Coherent Evolution)). Amplified pulses are ejected from the cavity at 5 kHz and sent to a four-grating compressor, finally producing compressed pulses at 5 kHz but at much higher pulse power (400-600 μJ/pulse). (Stretcher, amplifier and compressor make up Coherent Legend Elite).

Pulses from the regen lack the bandwidth necessary for our experiments, so from here the light is sent to either a noncollinear optical parametric amplifier (NOPA, Light Conversion TOPAS White) or to a homebuilt supercontinuum filamentation setup. The NOPA creates a small amount of continuum light that is combined with 400 nm light (frequency doubled from the original regen output) in a nonlinear crystal, undergoing a difference frequency generation process which generates light from 530-650 nm FWHM. This is compressed to a pulse duration of roughly 12 fs using an SLM based pulse shaper (Biophotonics FemtoJock) combined with a prism pair. In experiments using the GRAPES spectrometer (Chapters 2 and 4), supercontinuum broadband light is generated by focusing in argon (with an optional second focusing step in air), generating light spanning the visible range. This light is filtered depending on the spectral requirements of a given experiment, then compressed using an SLM based pulse shaper (Biophotonics MIIPS Box 640).

There are multiple valid designs for a 2D spectrometer. A traditional approach (used in Chapter 3) is to use a beam splitter to separate an incoming beam into two parts, with one sent to a retroreflector on a movable translation stage as a control of waiting time. The two

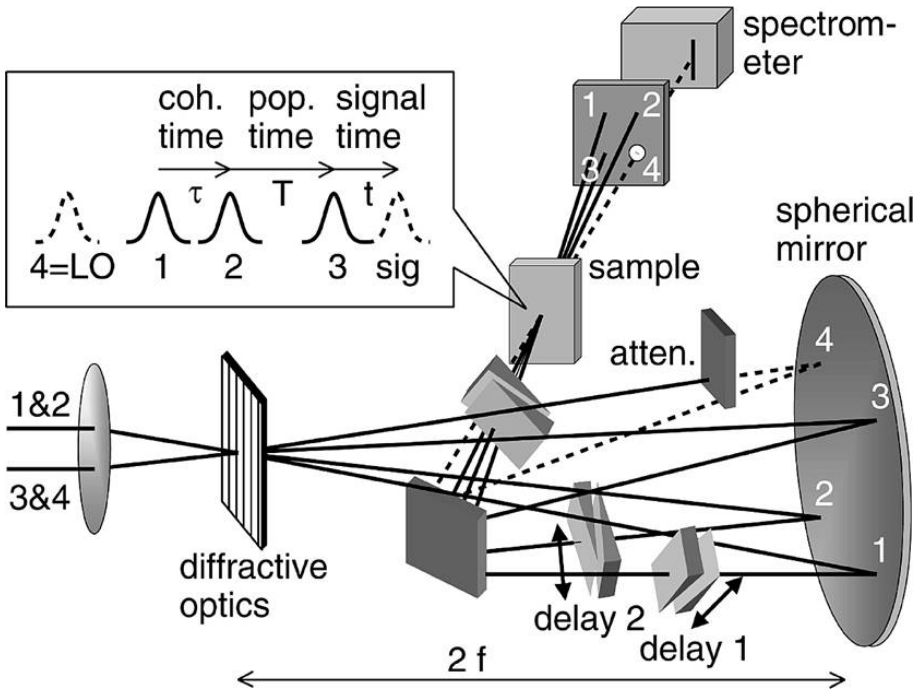

Figure 1.3: A traditional BOXCAR geometry configuration for 2D electronic spectroscopy. Beams 1&2 and 3&4 are split using a diffractive optic to create the four beams used in the experiment, with relative timings controlled via paired glass wedges. Figure from [15], used with permission.

beams are then sent to a diffractive optic, splitting the beams to create four in a BOXCAR geometry. Independent delay of beams 1 and 2 can be accomplished using paired glass wedges. All four beams are sent to a single focusing optic, and after the sample beam 4 (and the co-propagating signal) are directed into an imaging spectrometer (Andor Shamrock) and detected using a CCD array (Andor Newton). An example of such a design can be seen in Figure 1.3.

An alternative approach to the control of 1-2 and 3-4 time delays is through the use of geometrically tilted pulses focused to a line, as is done in GRadient Assisted Photon Echo Spectroscopy (GRAPES). As with the approach described above, 2D timing control begins by splitting an incoming pulse into two, generating the waiting time delay. Each of these resulting beams is sent to a beamsplitter made either of wedged glass (Chapter 2) or a combination of a partially silvered and full silver mirror (Chapter 4), generating separate pulses traveling in a vertically stacked pattern. The first and second reflections from each

beamsplitter are used, creating a shifted BOXCAR geometry. In this configuration, beams 2 and 3 are horizontally aligned with each other, with beam 1 below beam 2 and beam 4 above beam 3. These are made to overlap vertically with flat mirrors and focused using a cylindrical mirror, leading to a line of focus where beam 1 arrives before beam 2 at one end of the line and after beam 2 at the other end. Beam 4 and the copropagating emitted signal are focused through a spatial filter and imaged on a two-dimensional CMOS array (Phantom Miro M310 in Chapter 2 and Andor Neo in Chapter 4).

1.3.4 Data Processing and Analysis

In both versions of 2DES described above, the horizontal camera axis contains wavelength-resolved information on the rephasing axis of the 2D spectrum. This is interpolated to make it linear in frequency, then fourier transformed to produce a signal resolved in rephasing time. The coherence time axis is already resolved in time (either as separate measurements in traditional 2D or as the vertical axis in GRAPES) and does not require Fourier processing to create a time-time plot of the spectrum. The time-time-time cube of recorded GRAPES data does require further processing, however. Because beams 2 and 3 are not tilted relative to one another, the nonrephasing portion of the spectrum (where the beam order at the sample is 2-1-3) is not emitted at the same waiting time. Instead, the waiting time must be shifted to match the angle of beam 1, as shown in Figure 1.4 from [18] Once this data restructuring is complete, Fourier transformation of the coherence and rephasing axes produce a time series of 2D spectra.

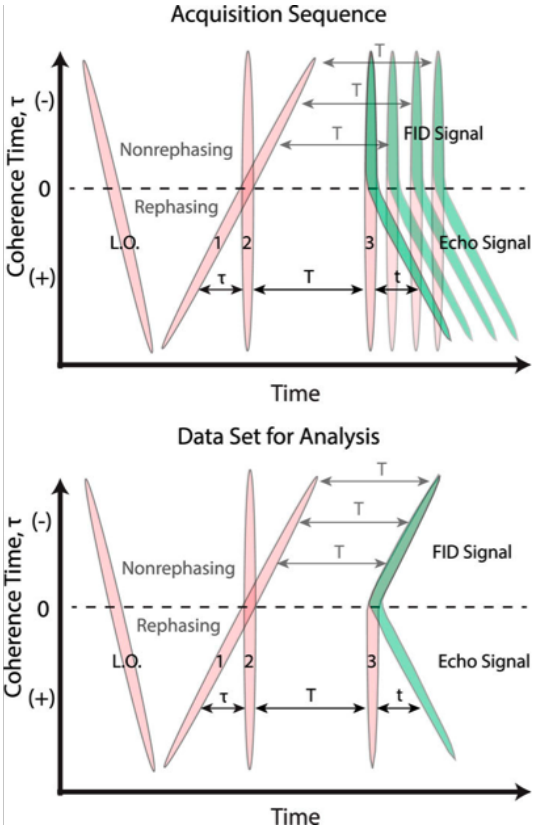

Figure 1.4: Generating Absorptive 2D spectra from the GRAPES instrument. Figure from [18], used with permission.

In highly scattering samples, a number of experimental and post-processing steps can be taken to filter out unwanted contributions and increase the signal-to-noise ratio of the resulting 2D spectra, as illustrated in Figure 1.5. [19] Part A of this figure shows the many scatter contributions that the camera measures along with the desired signal (colored green in the figure). Scatter from beams 3 and 4 interacting can be isolated through the use of a chopper that blocks beams 1 and 2, allowing this contribution to be subtracted directly from the measured camera data. Scatter that does not involve the local oscillator reference (beam 4) occurs at a different position in rephasing time t, and can be filtered out in this domain as shown in part B. The remaining scatter depends on a combination of beams 1 or 2 and beam 4, and as such will oscillate in waiting time T at the optical frequency. Because the signal does not oscillate rapidly in this domain, filtering in the ω_T domain removes this scatter contribution, leaving only the desired signal. A second option for scatter removal that is used in the BOXCAR geometry spectrometer is the combination of a shutter blocking beams 1&2 and one blocking beam 3. This allows for independent measurements of signals I_{1234}, I_{34}, I_{124}, and I_4. The desired signal-LO heterodyne (I_{s4}) with scatter removed can be attained by the equation $I_{s4} = I_{1234} - I_{34} - I_{124} + I_4$.

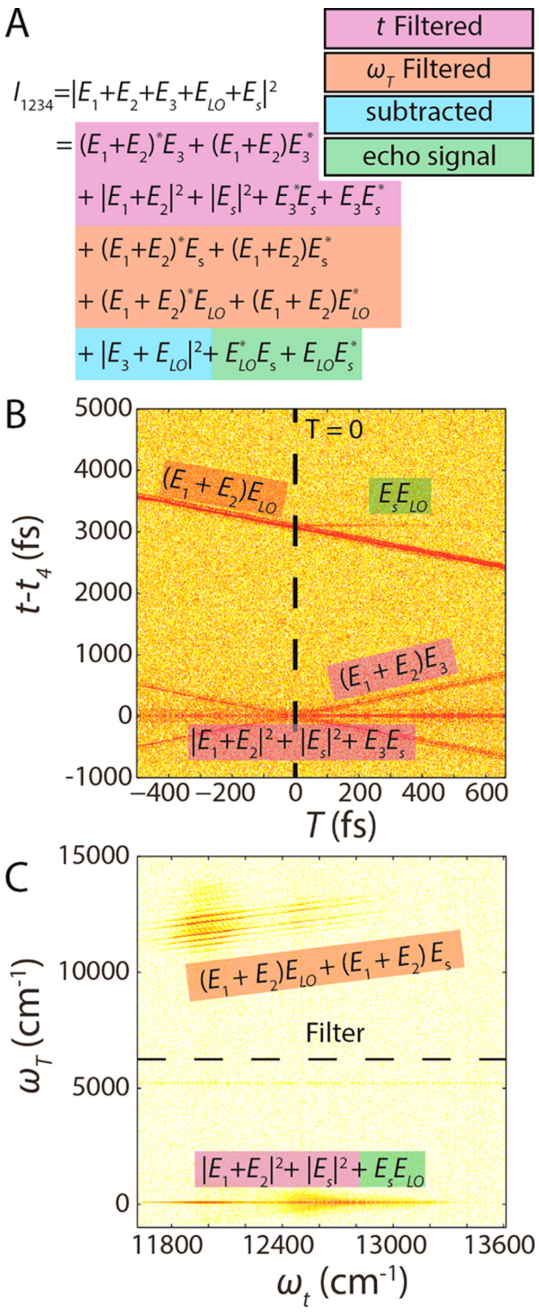

Figure 1.5: Scatter removal in 2D spectroscopy via post processing. Figure from [19], used with permission

REFERENCES

[1] Robert E. Blankenship, David M. Tiede, James Barber, Gary W. Brudvig, Graham Fleming, Maria Ghirardi, M. R. Gunner, Wolfgang Junge, David M. Kramer, Anastasios Melis, Thomas A. Moore, Christopher C. Moser, Daniel G. Nocera, Arthur J. Nozik, Donald R. Ort, William W. Parson, Roger C. Prince, and Richard T. Sayre. Comparing photosynthetic and photovoltaic efficiencies and recognizing the potential for improvement. *Science*, 332(6031):805–809, 2011.

[2] Nathan S. Lewis and Daniel G. Nocera. Powering the planet: Chemical challenges in solar energy utilization. *Proceedings of the National Academy of Sciences*, 103(43):15729–15735, 2006.

[3] Robert E. Blankenship. *Molecular Mechanisms of Photosynthesis*. Wiley/Blackwell, 2013.

[4] T. Förster. Energiewanderung und Fluoreszenz. *Naturwissenschaften*, 33:166–175, June 1946.

[5] T. Förster. *Istanbul Lectures, Part III: Action of Light and Organic Crystals*. Academic Press, New York, 1965.

[6] Abraham Nitzan. *Chemical Dynamics in Condensed Phases: Relaxation, Transfer and Reactions in Condensed Molecular Systems*. Oxford University Press, New York, 2006.

[7] A. G. Redfield. On the theory of relaxation processes. *IBM Journal of Research and Development*, 1(1):19–31, 1957.

[8] Thomas Renger. Theory of excitation energy transfer: from structure to function. *Photosynthesis Research*, 102(2):471–485, 2009.

[9] Yuan-Chung Cheng and Graham R. Fleming. Dynamics of light harvesting in photosynthesis. *Annual Review of Physical Chemistry*, 60(1):241–262, 2009.

[10] Gregory S. Engel, Tessa R. Calhoun, Elizabeth L. Read, Tae-Kyu Ahn, Tomáš Mančal, Yuan-Chung Cheng, Robert E. Blankenship, and Graham R. Fleming. Evidence for wavelike energy transfer through quantum coherence in photosynthetic systems. *Nature*, 446:782, 2007.

[11] Yoshitaka Tanimura. Reduced hierarchy equations of motion approach with drude plus brownian spectral distribution: Probing electron transfer processes by means of two-dimensional correlation spectroscopy. *The Journal of Chemical Physics*, 137(22):22A550, 2012.

[12] Shaul Mukamel. *Principles of nonlinear optical spectroscopy.* New York : Oxford University Press, 1995.

[13] P. Hamm and M. T. Zanni. *Concepts and methods of 2D infrared spectroscopy.* Cambridge University Press, New York, 2011.

[14] Jakub Dostál, Barbora Benešová, and Tobias Brixner. Two-dimensional electronic spectroscopy can fully characterize the population transfer in molecular systems. *The Journal of Chemical Physics*, 145(12):124312, 2016.

[15] Minhaeng Cho. Coherent two-dimensional optical spectroscopy. *Chemical Reviews*, 108(4):1331–1418, 04 2008.

[16] Justin R. Caram, Andrew F. Fidler, and Gregory S. Engel. Excited and ground state vibrational dynamics revealed by two-dimensional electronic spectroscopy. *The Journal of Chemical Physics*, 137(2):024507, 2012.

[17] Daniel B. Turner, Rayomond Dinshaw, Kyung-Koo Lee, Michael S. Belsley, Krystyna E. Wilk, Paul M. G. Curmi, and Gregory D. Scholes. Quantitative investigations of quantum coherence for a light-harvesting protein at conditions simulating photosynthesis. *Physical Chemistry Chemical Physics*, 14:4857–4874, 2012.

[18] Sara H. Sohail, Peter D. Dahlberg, Marco A. Allodi, Sara C. Massey, Po-Chieh Ting, Elizabeth C. Martin, C. Neil Hunter, and Gregory S. Engel. Communication: Broad manifold of excitonic states in light-harvesting complex 1 promotes efficient unidirectional energy transfer in vivo. *The Journal of Chemical Physics*, 147(13):131101, 2017.

[19] Peter D. Dahlberg, Andrew F. Fidler, Justin R. Caram, Phillip D. Long, and Gregory S. Engel. Energy transfer observed in live cells using two-dimensional electronic spectroscopy. *The Journal of Physical Chemistry Letters*, 4(21):3636–3640, 2013.

CHAPTER 2

REDOX CONDITIONS AFFECT ULTRAFAST EXCITON TRANSPORT IN PHOTOSYNTHETIC PIGMENT-PROTEIN COMPLEXES

Pigment-protein complexes in photosynthetic antennae can suffer oxidative damage during solar light harvesting that can ultimately lead to cell death. Understanding how the redox environment of a pigment-protein complex affects energy transport on the ultrafast light-harvesting timescale remains poorly understood. Using two-dimensional electronic spectroscopy, we observe differences in femtosecond energy-transfer processes in the Fenna-Matthews-Olson (FMO) antenna complex under different redox conditions. These differences in the ultrafast dynamics result from changes to the system-bath coupling around specific chromophores, and we identify a highly-conserved tyrosine/tryptophan chain near the chromophores showing the largest changes. We discuss how the mechanism of tyrosine/tryptophan chain oxidation may contribute to these differences in ultrafast dynamics that can moderate energy transfer to downstream complexes where reactive oxygen species are formed. These results highlight the importance of redox conditions on the ultrafast transport of energy in photosynthesis. Tailoring the redox environment may enable energy transport engineering in synthetic light-harvesting systems.

2.1 Pigment-Protein Complexes and Reactive Oxygen Species

Pigment-protein complexes enable the primary steps of photosynthesis, from absorption to charge separation [1, 2]. In the green sulfur bacterium Chlorobaculum tepidum, the tightly-packed chromophores in the Fenna-Matthews-Olson (FMO) complex act as an energetic

The research described in this chapter has been published in: M. A. Allodi*, J. P. Otto*, S. H. Sohail, R. G. Saer, R. E. Wood, B. S. Rolczynski, S. C. Massey, P. C. Ting, R. E. Blankenship, and G. S. Engel. Redox Conditions Affect Ultrafast Exciton Transport in Photosynthetic Pigment-Protein Complexes. *J. Phys. Chem. Lett.* 9(1):89-95, 2018. Reproduced with permission.

funnel, transferring light energy from the chlorosome to the organism's Type I reaction center via Exciton Energy Transfer [3, 4, 5, 6, 7, 8, 9]. Molecular excited states can also supply energy to generate reactive oxygen species (ROS) from molecular oxygen [10]. For example, in GSB, ferredoxin reduced by the reaction center reacts readily with molecular oxygen to produce superoxide [11].

Photosynthetic organisms have evolved protective mechanisms to quench excess excitations to prevent excessive ROS formation [12, 13]. Recent work has shown that excitations in the FMO complex are affected by redox conditions [14] generating questions on what, if any, role FMO may play in protecting GSB from oxidative damage. Strong reducing agents, such as sodium dithionite have long been known to increase the fluorescence yield of FMO [15, 16]. Point mutations replacing two cysteine residues with alanine eliminated this "dithionite effect," suggesting a quenching mechanism that utilizes thiyl radicals on oxidized cysteines [14]. The mutated residues Cys353 and Cys49 are 4.9 Å away from chromophores composing some of the lowest energy excitons, [17] making them well positioned to quench excitations in the FMO complex before they transfer from bacteriochlorophyll site III into the reaction center.

In contrast to the approach taken by photosynthetic organisms to quench excitations before they generate ROS, enzymes that perform redox chemistry in the presence of oxygen have mechanisms to protect the active site of the protein from being damaged after the formation of ROS. Many enzymes have a set of redox-accessible sulfur-containing amino acids, such as cysteine or methionine, near the active site [18], and recent work as also found a complementary mechanism in which a tyrosine/tryptophan (Tyr/Trp) chain several residues long can transport the hole created by oxidation out to the solvent-exposed region of the protein, where it can be reduced by radical scavengers [19, 20, 21, 22]. In these enzymes, this structural moiety provides additional protection to the parts of a protein particularly susceptible to damage from ROS.

In this work, we investigate how the oxidative state of amino acid side chains in the vicin-

ity of chromophore molecules affects the system-bath coupling and therefore also ultrafast energy transfer through a pigment-protein complex. We perform two-dimensional electronic spectroscopy (2DES) [23, 24, 25] measurements on both wild-type complexes and mutant complexes lacking cysteine residues under different redox conditions. The cysteine-mediated mechanism proposed by Orf et al. [14]. quenches excitations on long timescales under oxidizing conditions. Surprisingly, we also find clear differences in the dynamics under different redox conditions in cysteine-lacking C353A/C49A FMO mutants. Because 2DES allows us to observe directly which excitons are affected by redox conditions, we identify that some residues other than cysteine near sites III and IV must change their redox state to affect EET through the FMO complex on the femtosecond (10-15 s) timescale. We identify a Tyr/Trp chain as a structural moiety in the vicinity of sites III and IV that is likely redox sensitive. Oxidation of these residues could affect energy transfer. The FMO complex is a common model system for exciton energy transfer in photosynthetic pigment-protein complexes. We now observe differences in ultrafast energy transfer as a function of redox conditions on the timescales of the initial photosynthetic light harvesting event.

2.2 Sample Preparation and Data Collection

C. tepidum was grown, and FMO was isolated in CAPS (N-cyclohexyl-3-aminopropanesulfonic acid) buffer (pH 10.5) from these cultures as discussed previously [28, 29, 30, 14]. Measurements of the FMO complex are taken by making a mixture of 50% glycerol by volume and CAPS-buffered (pH 10.5) FMO protein. Under "oxidative" conditions, the samples were prepared under ambient conditions; in the "reductive" case, sodium dithionite was added to the protein, buffer, and glycerol mixture until the concentration of sodium dithionite was 10 mmol. The mixture was placed in a 0.2 mm quartz cuvette (Starna) that was coated with SigmaCote (Sigma-Aldrich). The cuvette was loaded into a nitrogen-cooled cryostat (Oxford Instruments) and rapidly cooled to 77 K, forming a glass.

The 2D electronic spectra were acquired using the GRAPES single-shot spectrometer

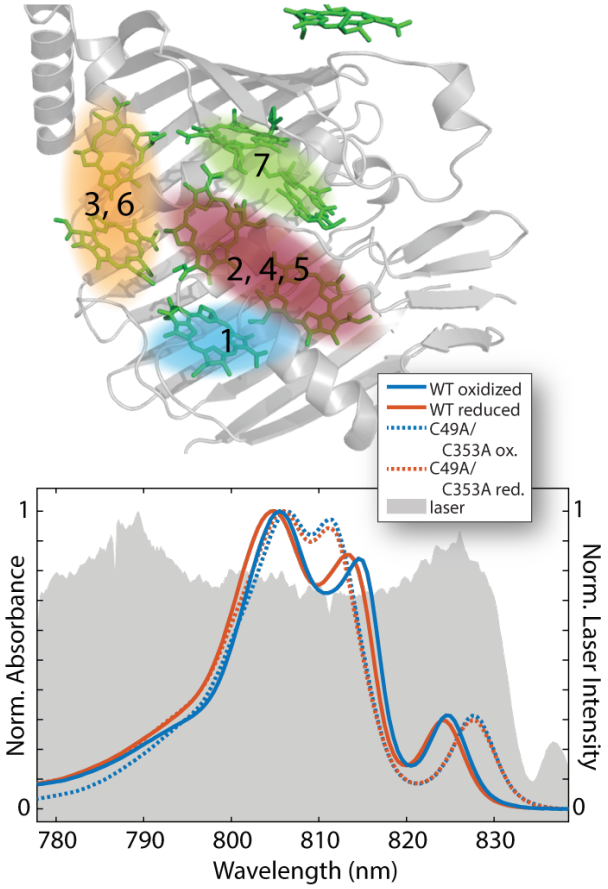

Figure 2.1: *(top)* Structure of the FMO complex with excitons labeled with Arabic numerals. The bacteriochlorophyll molecules are colored green and the positions of the excitons are shown in shaded color. The contribution of different bacteriochlorophyll molecules was taken from Cho et al. 2005.[26] The FMO structure is taken from PDB 3ENI.[27] *(bottom)* Absorption spectra of samples and laser bandwidth. Solid blue lines show oxidized wild-type FMO, solid red show reduced wild-type FMO, and dotted blue and red lines show oxidized and reduced C49A/C353A mutant FMO, respectively. Laser intensity as measured on the same instrument as the 2D data is shown in gray. All absorption spectra are measured at 77K.

described in detail elsewhere [31, 32, 33]. In brief, the output of an ultrafast regenerative amplifier (Legend Elite USP, Coherent) centered at 800 nm and running at a 5 kHz repetition rate was focused through a tube containing 15 psi of Ar gas. The broadened light was focused again in air to produce a spectrum that spans from 775 nm to 840 nm. This bandwidth was compressed to a sub-20 fs laser pulse using a pulse shaper (MIIPS Box 640, Biophotonics Solutions) running a MIIPS algorithm [34]. The beam was split into four beams to form a shifted boxcars geometry. Pulse 1 has a geometric tilt relative to pulses 2 and 3, meaning that different parts of the uniform sample encode different coherence times, with 0.9 fs steps between different coherence times. Beams 1 and 2 are chopped together at 50 Hz and the signal is collected in the -k1 + k2 + k3 phase-matched direction on the slit of an imaging spectrometer (Shamrock, Andor Technologies) and recorded on a CMOS camera (Miro M310, Vision Research). The arrival of pulses 1 and 2 is swept relative to pulse 3 and individual 2DES spectra are recorded at waiting times from -300 fs to +2000 fs with a 0.4 fs spacing. Data are Fourier filtered in the waiting-time domain to remove scattered light, generating a final data set with 10 fs spacing between waiting times. 2D spectra were also acquired at the following fixed waiting times for comparison with previous work between 5 ps and 1 ns. Both the rephasing and non-rephasing Liouville pathways were extracted from the data and added together to create an additional data set representing the purely absorptive portion of the 2D signal [35, 36]. The 2DES data were phased by fitting to separately-acquired pump-probe data using a sum-of-squared-error regression. The centerline slope was determined by fitting a line to brightest probe frequency pixels for each pump frequency across relevant features.

2.3 Results

We performed 2DES measurements at 77 K under two different experimental conditions. In one set of experiments, FMO complexes were handled under ambient atmospheric conditions, which we refer to as oxidative conditions, as previous literature studies have done [14]. In the other set, sodium dithionite was added to a mixture of protein, glycerol, and buffer

to a dithionite concentration of 10 mmol before vitrification. The structure of the FMO complex and the linear absorption spectra of the different samples can be seen in Figure 2.1. Sodium dithionite is a strong reducing agent ($E^{\circ\prime}$ = -1.07 V vs. NHE at pH 10.5 [37]) that reacts with molecular oxygen, effectively removing it from solution. To provide statistically significant measurements of our error, the 2DES data presented are averages of 25 independent 2DES measurements taken on a GRAPES spectrometer [32, 36, 35]. All data presented are normalized to the maximum of the spectrum at zero waiting time (T = 0). Additional information about the experimental methods can be found in the supplemental information. The correlations between excitation and detection wavelength for wild-type FMO under oxidative or reductive conditions are shown in Figure 2.2A-D.

2.3.1 2D Electronic Spectra of wild-type FMO

Since the below-diagonal cross-peak amplitudes result from downhill energy transfer, we compare the intensity of these features under the oxidative and reducing conditions. One major pathway through the FMO complex involves energy transport from exciton 7 to exciton 4, through exciton 2 and finally into exciton 1 [26, 38, 39]. This pathway shows redox-environment-dependent differences in ultrafast dynamics and efficiency of energy transfer. Under oxidized or reduced conditions, the traces in Figure 2.2F, which are taken at the 4-2 cross peak, show differences in both normalized amplitude and dynamics between the reduced and oxidized experiments. The panels in Figure 2.2H and I show energy-transfer cross peaks into exciton 1, demonstrating clear differences in the transport dynamics through the FMO complex. When we fit an exponential decay starting at the peak value of the 4-2 cross peak, this cross peak decays with a 710 fs time constant in the reduced experiment, compared with a 1300 fs time constant in the oxidized experiment. The 4-1 cross peak in the reduced data grows in faster (460 fs reduced v. 492 fs oxidized) and also reaches a larger amplitude (almost 1, Figure 2.2I). Traces corresponding to the remaining features in this pathway are shown in Figure 2.3. All fits can be found in supplemental table 2.3. We

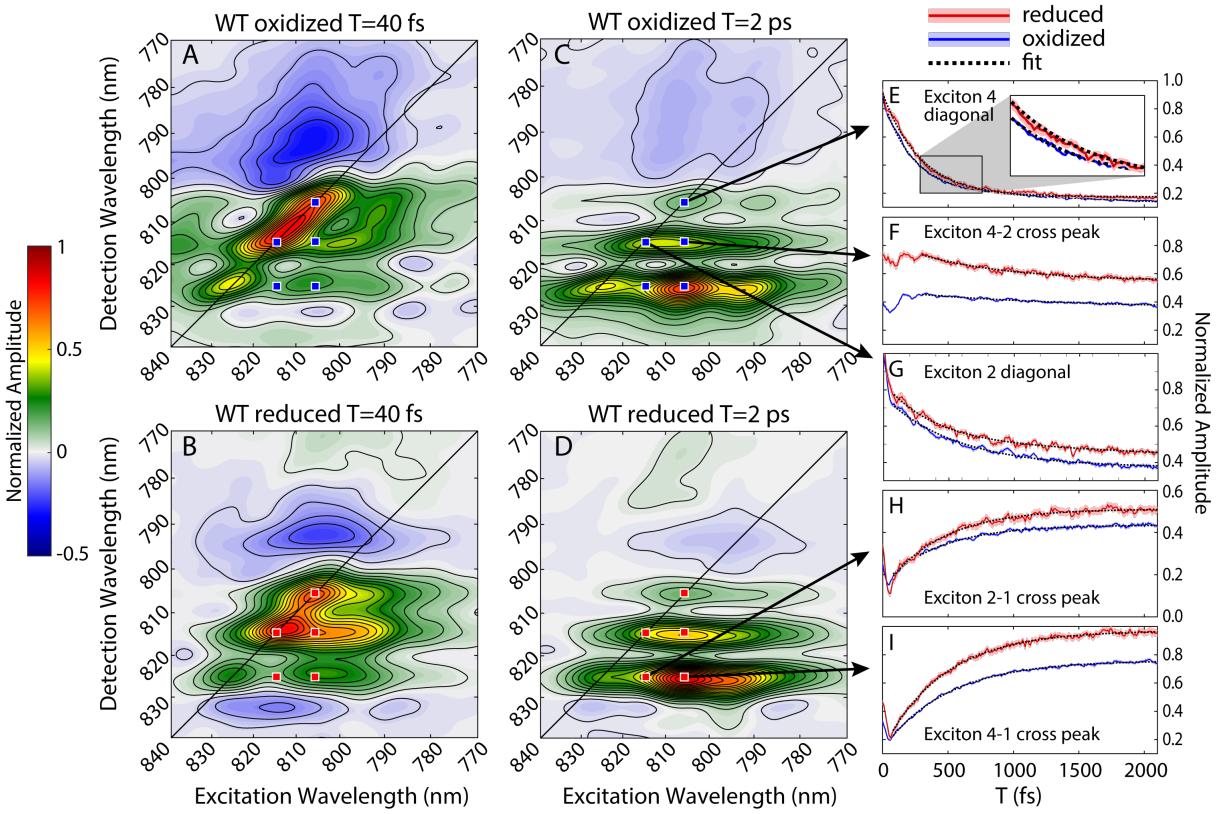

Figure 2.2: Two-dimensional electronic spectra of wild-type FMO showing redox-dependent ultrafast dynamics. (A and B) 2D spectra of FMO at early waiting times. (C and D) 2D spectra at longer waiting times. (E-I) Representative time traces taken at the spots indicated by blue (oxidized) or red (reduced) markers. The dotted black lines shown with the traces were obtained by a least-squares fit to the data. The shading around the colored lines represents the standard error on the mean from 25 independent measurements. The inset in E allows a clear view of the error bars.

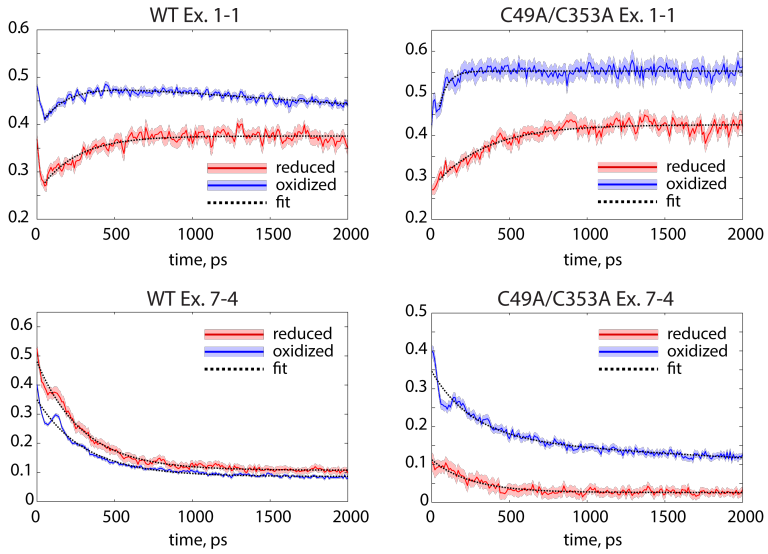

Figure 2.3: Real-valued time traces of Ex. 1-1 and Ex. 7-4 from wild-type and mutant FMO. The shaded error bars shown represent the standard error on the mean for 25 averages.

conclude from these data that the different oxidative conditions affect the energy flow into and out of excitons 2 and 4, which are known to be associated with chromophores at sites III and IV [26].

Looking at the diagonal peak traces, which report on exciton populations, we see evidence that a trap or quenching site affects the ultrafast dynamics. The exciton 4 energy traces, shown in Figure 2.2E, exhibit different dynamics in waiting time; both traces start from similar initial normalized amplitudes, and the excitation in the oxidized experiment decays slightly more quickly than the reduced case. Also, the exciton 2 diagonal features (Figure 2.2G) show the same, but more pronounced, trend as the exciton 4 diagonal features. Some trap or quenching site must be removing excitations faster in the oxidized versus the reduced experiment. The cysteine-mediated quenching certainly contributes to these dynamics, and we confirm that the cysteine-mediated mechanism is still in effect by collecting 2DES spectra at different waiting times between 5 ps and 1 ns. We observe trends in these longtime dynamics consistent with the previous work by Orf et al., see Figure 2.7 [14].

The interactions between the pigments and the protein in the FMO complex determine how energy transport occurs. The protein acts as a scaffold that holds the chromophores in

a fixed position and orientation, thus defining the site energies and coupling that generate the electronic system Hamiltonian. Vibrations within the protein that serves as a bath that couples to the chromophores, giving rise to the spectral density. Quantum mechanically, for there to be energy transfer between exciton states, there must be system-bath coupling [40, 41, 42]. As a result, changes to the spectral densities of the bath affect the interactions of the excitons and their subsequent transport through the FMO complex.

Differences in EET can result from differences in the coupling of the chromophore system to the protein-bath environment or from differences in the chromophores' positions and orientation with respect to each other, thus changing the system Hamiltonian. Changes to the system result in in changes to the exciton peak positions. Small differences can be seen in the linear spectra under oxidizing vs. reducing conditions in Figure 2.1. Since the shifts in the linear spectra are small and that the exciton positions do not change on the timescales of our 2D measurements, we focus our discussion on differences in system-bath coupling.

An analysis of the absorptive 2D lineshape of the FMO complex provides direct evidence for differences in the system-bath coupling, since the time evolution of the lineshape is a direct reporter of the bath spectral densities that modulate the energy of the surrounding excitons [43]. As seen in Figure 2.2A-D, the positive diagonal features around 825 nm, 812 nm, and 805 nm correspond to the energies of excitons 1, 2 and 4 respectively [26, 39]. These positive peaks along the diagonal in both the oxidized and reduced datasets show diagonal elongation at early times corresponding to an inhomogeneous environment surrounding the chromophores. The evolution of these features across waiting time can be seen in Figures 2.4 and 2.5.

The spectral diffusion can be quantified using a centerline slope analysis [44]. In the reduced experiments, this diagonal elongation rapidly disappears; the exciton 1 feature at 825 nm has a decay of the centerline slope of 30 fs, while the exciton 4 feature at 805 nm can be fit with a 160 fs time constant. Plots of the centerline slope can be seen in Figure 2.5. In contrast, the inhomogeneous broadening is larger in the oxidized experiments at early times

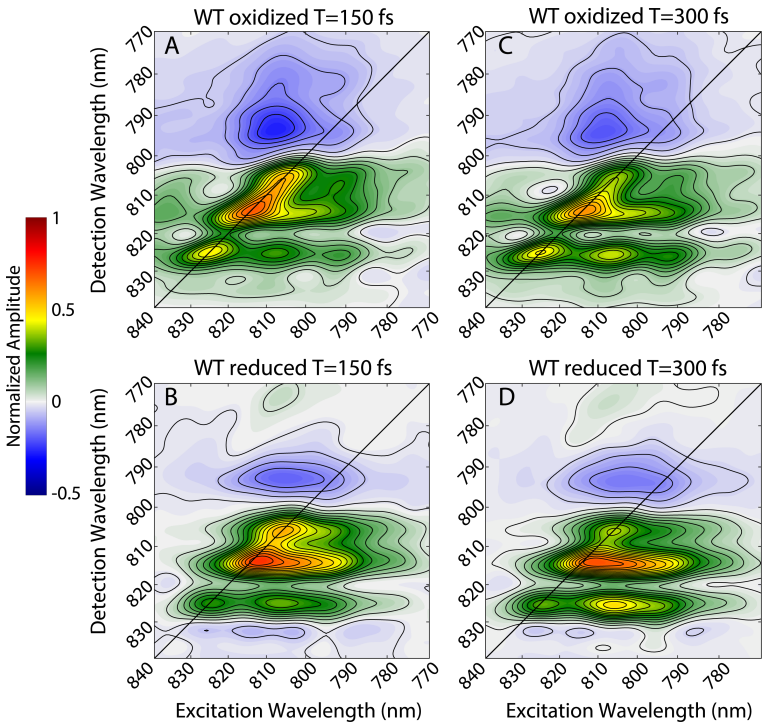

Figure 2.4: 2DES of wild-type FMO at T=150 fs and at T=300 fs show persistence of inhomogeneity. In the exciton 1 feature on the diagonal at 825 nm, clear differences between the two redox conditions can be seen in diagonal elongation, as supported by the centerline slope measurements in Figure 2.5.

and persists over all timescales measured in these experiments.

Centerline slope fit parameters: *(all times in fs)*

Exciton 1	a_1	τ_1	a_2	τ_2
WT reduced	0.2 ± 0.1	30 ± 10	0.067 ± 0.003	3200 ± 500
WT oxidized	0.14 ± 0.02	70 ± 10	0.182 ± 0.003	4800 ± 300
Exciton 4	a_1	τ_1	a_2	τ_2
WT reduced	0.32 ± 0.04	160 ± 20	-	-
WT oxidized	0.34 ± 0.02	900 ± 90	-	-

Table 2.1: Fits to centerline slope decay. Traces are fit to a biexponential of the form $a_1 e^{(-T/\tau_1)} + a_2 e^{(-T/\tau_2)}$ for exciton 1 and an exponential $a_1 e^{(-T/\tau_1)}$ for exciton 4. Error is 95% confidence.

The differences in inhomogeneous broadening shows that oxidative conditions change the local environment around excitons 4, 2, and 1, and affect the system-bath coupling. Under reducing conditions, spectral diffusion produces round lineshapes as the bath effectively solvates the excited-state charge distribution [45]. In contrast, under oxidative conditions, a

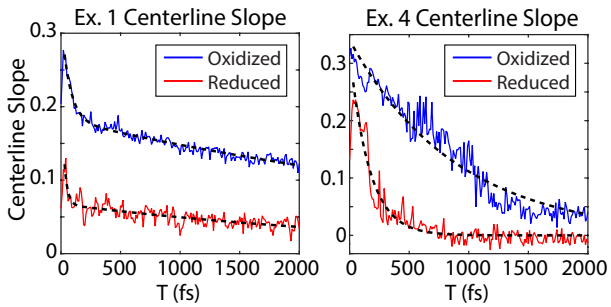

Figure 2.5: Centerline slope decay for two different excitons in wild type FMO. Higher slopes indicate greater inhomogeneous contribution to feature lineshape.

set of different charge distributions around these chromophores produces the inhomogeneous lineshape observed in Figure 2.2 C and D. As such, changes caused by oxidation of the residues around excitons 4, 2, and 1 change the spectral densities of the bath, and this spectral density appears not to solvate the excited-state electron distribution as effectively as under reductive conditions. In addition, because the centerline slope analysis shows that spectral diffusion happens slightly faster at higher-energy excitons in the reduced wild type, we know that the bath is not the same around each exciton. These tailored, different spectral densities likely play a key role in controlling energy transfer through the complex, and further investigation is necessary to understand the role that these differences may play. This mechanism has implications for modeling exciton transport as recent theoretical work has calculated differences in spectral densities around different chromophores [46].

2.3.2 Cysteine-subtracted mutant FMO

To understand if the effects of different redox conditions on EET is related to, or distinct from, the cysteine-mediated mechanism previously discovered in FMO, we performed 2DES measurements on the mutant FMO strain C49A/C353A. If the cysteine-mediated mechanism were the only redox-dependent mechanism that affected EET in the FMO complex, eliminating these cysteines should remove the differences in the dynamics observed in the 2DES measurements of the wild type. However, a comparison between mutant and wild-type 2DES measurements shows that the redox-active cysteines alone cannot be responsible for

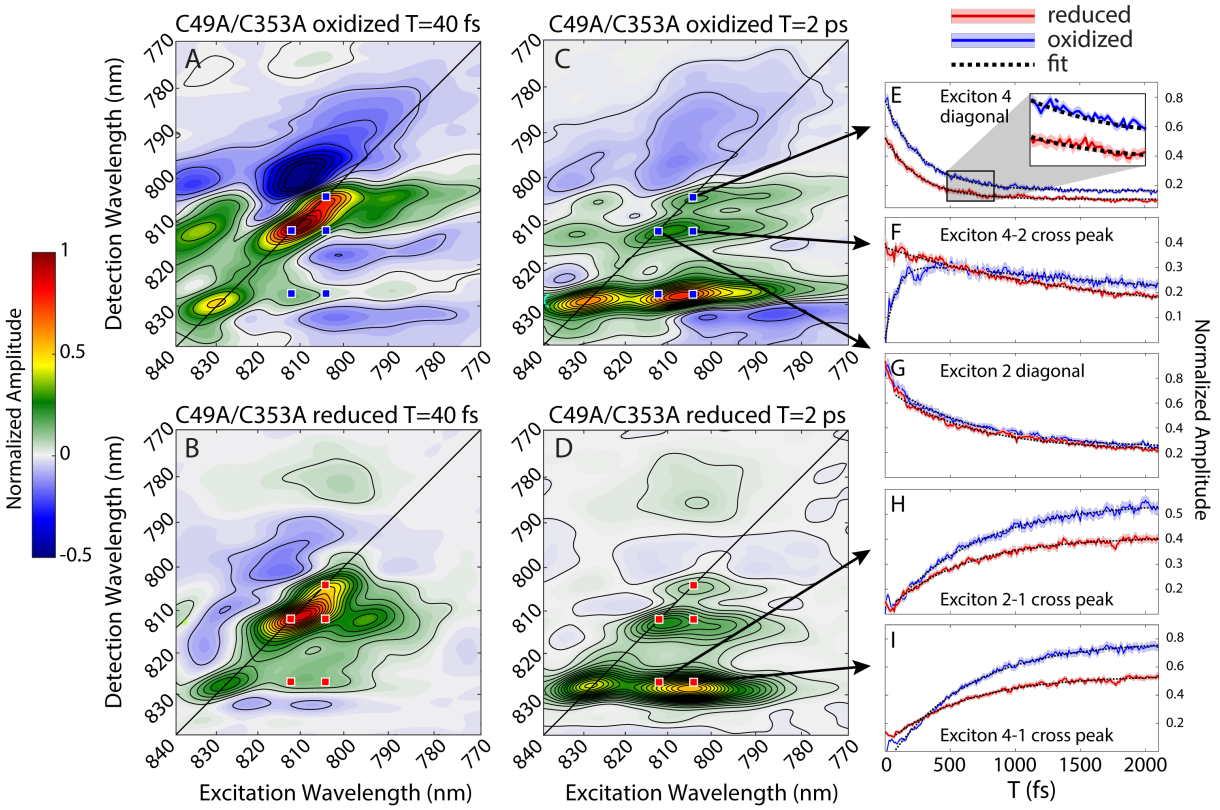

Figure 2.6: Two-dimensional electronic spectra of mutant C49A/C353A FMO showing redox-dependent ultrafast dynamics. (A and B) 2D spectra at early waiting times. (C and D) 2D spectra at longer waiting times. (E-I) Representative time traces taken at the spots indicated by blue (oxidized) or red (reduced) markers. The dotted black lines shown with the traces are a least-squares fit to the data. The shading around the colored lines represents the standard error on the mean from 25 independent measurements. The inset in E allows a clear view of the error bars.

the differences observed in the wild-type spectra.

The redox-dependent differences in the dynamics of the mutant complexes are even larger than those of the wild type complexes. 2DES spectra are presented in Figure 2.6A-D. Figure 2.6E shows that, in the mutant, the decay of the exciton 4 diagonal peak displays different relative amplitudes and time constants, depending on the redox condition, while Figure 2.6G shows that the diagonal peak at exciton 2 displays similar dynamics between the two conditions. As in the wild type, the redox condition affects the dynamics of the 4-2 cross peak in the mutant. While there is still rapid transfer from 4 to 2 followed by decay in the reduced mutant sample, the oxidized mutant sample shows much slower growth followed by decay.

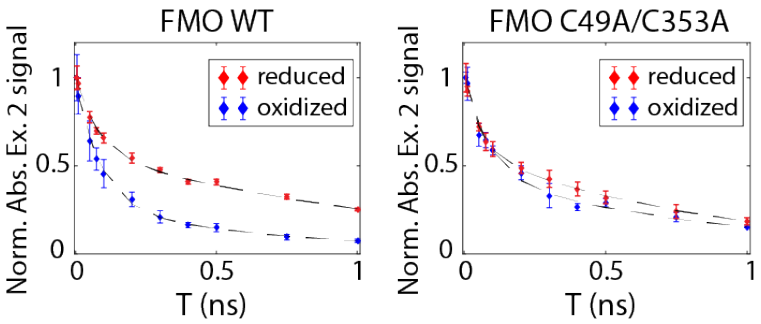

Figure 2.7: Normalized traces from absolute-value 2D spectra (rephasing plus non-rephasing) at longer waiting times. To facilitate comparison with previous time-resolved fluorescence experiments, these points were calculated by summing over the feature corresponding to exciton 2 (815 nm) along the excitation-wavelength axis. Error bars shown are standard error on the mean.

Also, both the 4-1 (Figure 2.6I) and 2-1 (Figure 2.6H) cross peaks show different dynamics to the wild type, as the signals from oxidized complexes grow in faster than those of the reduced complexes. Finally, both the oxidized and reduced experiment show a more inhomogeneous lineshape than in the wild type, with persistent inhomogeneity out to 2 ps (Figure 2.6A-D). These lineshape differences show that the system-bath coupling has meaningfully changed as a result of these mutations. 2DES measurements at long waiting times confirm that the mutant dynamics at long waiting times is the same, in agreement with Orf et al. (Figure 2.7). As a confirmation that differences between mutant and wild-type FMO are not due to phasing error, absolute value traces showing the same trends can be seen in Figure 2.8.

2.4 Tryptophan-Tyrosine Chains

A set of redox-active residues in the vicinity of excitons 4, 2, and 1 would explain the differences observed in the EET pathways in the wild-type and mutant FMO complexes under different redox conditions. Sulfur-containing amino acids, such as cysteine and methionine, are good candidates to play this role as they are well-understood components of the redox proteome that manage protein response to oxidative stress [47]. As the cysteine residues at sites 49 and 353 in FMO are the only sulfur-containing residues in close enough proximity to

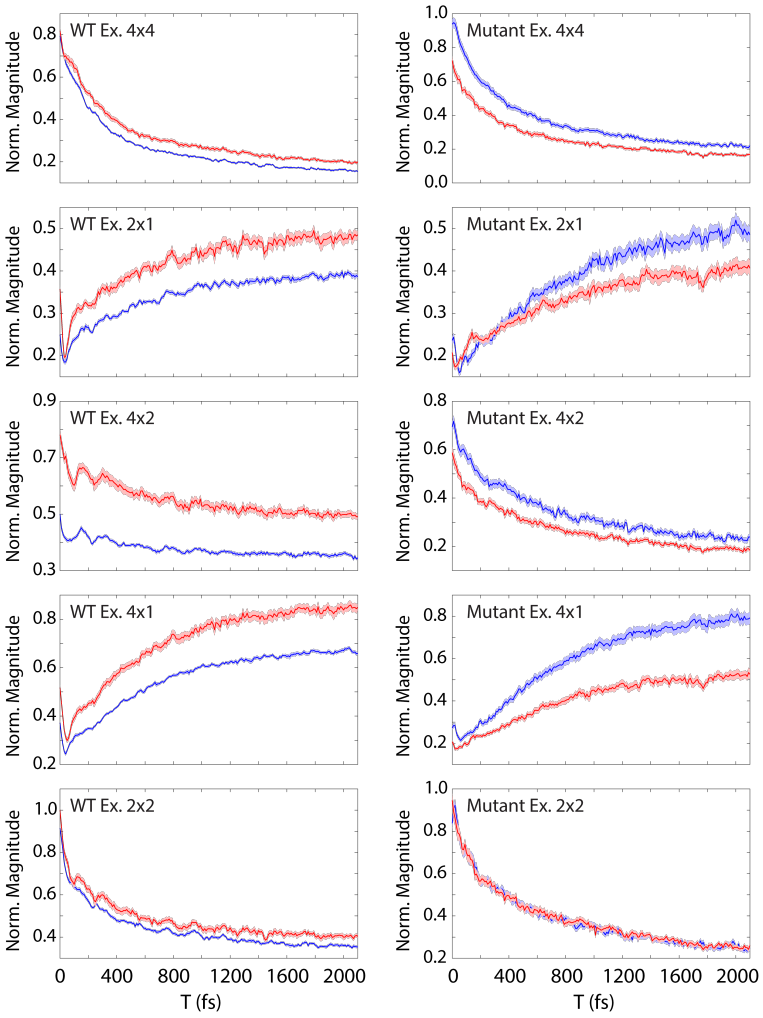

Figure 2.8: Absolute value time traces confirm trends shown in real-value phased data. Data from wild-type FMO are shown on the left, and from the C49A/C353A mutant on the right. Traces are taken at the same locations as in figures 2.2 and 2.6. Note that while cross-peak magnitudes are higher in the reduced wild type, the trend is reversed in the mutant. The shaded error bars shown represent the standard error on the mean for 25 averages.

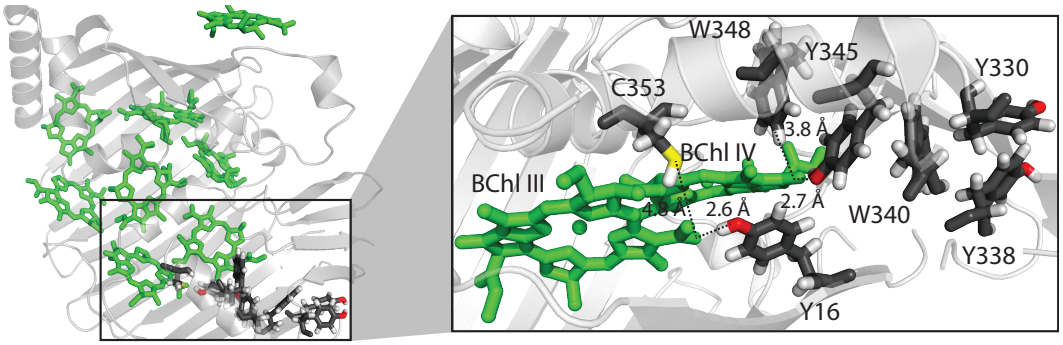

Figure 2.9: Structure of the Fenna-Matthews-Olson complex showing a Tyr/Trp in the vicinity of sites III and IV. The protein backbone is colored gray, while the BChl molecules are colored green with the phytyl tails removed for clarity. The residues of interest are labeled and are colored so that C is black, O is red, and S is yellow. Y345, W348, and C353 are collocated on the same alpha helix. Coordinates are taken from PDB structure 3ENI [27]. The distances reported are heavy-atom distances with hydrogens added.

interact with the chromophores, and our mutants lack the cysteines, oxidation of other redox-sensitive residues, such as tyrosine or tryptophan, provides another possible explanation for the trends observed in the data. Tryptophan and tyrosine molecules in solution at pH 10.5 can be oxidized at potentials around 0.7 V vs. NHE [48], and tryptophan and tyrosine residues in proteins are broadly considered susceptible to oxidation at potentials in the vicinity of 1 V vs. NHE [20]. within reach of superoxide ions generated by reduced ferredoxin [10]. Previous work has shown electron paramagnetic resonance (EPR) signatures consistent with tyrosine radicals in oxidized FMO [16].

As discussed by Gray and Winkler, Tyr/Trp chains, where one end starts in the interior of the protein and the other is solvent accessible, are likely to play a role in protecting proteins from oxidative damage.[20, 21] In the FMO complex, there exists only one chain of tyrosine and tryptophan residues facing into the chromophores, and this chain is in the vicinity of BChl sites III and IV - the sites that contribute to excitons 4, 2, and 1. The six residues (Y16, W348, Y345, W340, Y338, and Y330) in the tyrosine/tryptophan (Tyr/Trp) chain can be seen in Figure 2.9. Situated near site III, an oxidized Tyr/Trp chain could prevent excitations reaching the reaction center. There are six other tryptophan and six other tyrosine residues in the structure. None are in an extended chain, and all but two tryptophan residues (W184

and W239) are completely solvent exposed or more than 4 Åaway from any chromophores.

The presence of a hole along the Tyr/Trp chain will change the electrostatics of these chromophores, thus affecting the system-bath coupling and the transport properties that depend upon it [18, 49]. The differences in electronic structure between the mutant and wild-type complexes also contribute to the differences between their EET dynamics. The changes in electronic structure can be clearly seen as shifts in the peak centers and lineshape in both the linear absorption spectrum (Figure 2.1) and in the 2DES measurements. In the mutants, since the C353 residue is also in this same pocket as the chain, the absence of the large, polarizable sulfur atom is likely to perturb how the Tyr/Trp chain affects the system-bath coupling. Finally, as Figure 2.9 clearly shows, C353, W348, and Y345 all are part of the same alpha helix. In addition, Y16, W348, Y345, W340, Y338 residues are highly conserved across 28 different species of green sulfur bacteria [50], and are as conserved as the C353 residue [14].

There may be other factors that affect the redox-dependent ultrafast dynamics in FMO as well. Two isolated tryptophan residues, W184 and W239, are 3.2 Åand 3.9 Åaway from opposite sides of site VI, the major contributor to exciton 7, meaning that their oxidation could affect the system-bath coupling around that exciton. These residues can be seen in Figure 2.10. Groupings of aromatic residues have been understood to help stabilize protein folding and assist ligand binding [51, 52, 53], and because residue W184 is adjacent to F185, these residues likely play a structural role. In addition, these residues are in the chromophore pocket and not solvent exposed, so there is no way to transfer the strongly oxidizing hole away from the chromophores. However, if they are near site VI to help regulate energy transfer in the presence of ROS, they would be regulating the same major pathway through the FMO complex as the tyrosine-tryptophan chain near site IV. In addition, isolated FMO proteins can form aggregates after being solubilized. Aggregates of other photosynthetic pigment-protein complexes have shown aggregation-dependent quenching based on a charge-transfer mechanism on the ns timescale [54, 55]. However, given the timescales for charge-transfer in

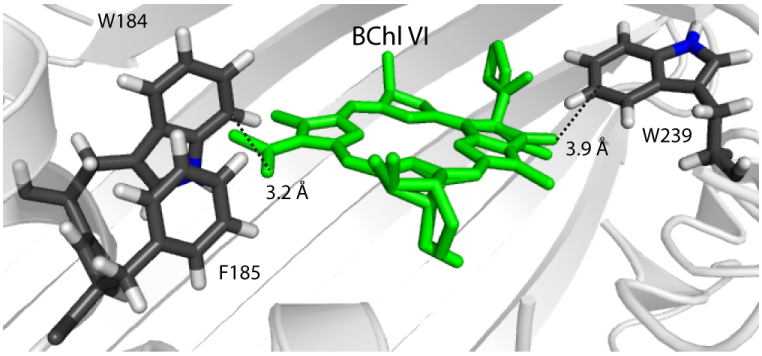

Figure 2.10: The pair of tryptophan residues near BChl site VI. The protein backbone is colored gray, while the BChl molecule is colored green with the phytyl tails removed for clarity. The residues of interest are labeled and are colored so that C is black and O is red. Interactions between W184 and F185 are likely part of the fold-stability of the protein structure. Coordinates are taken from PDB structure 3ENI [27]. The distances reported are heavy-atom distances with hydrogens added.

aggregation-dependent quenching in other complexes, it seems unlikely that this would lead to the significant differences in ultrafast dynamics observed here.

Long-time fit parameters: *(all times in fs, error is 95% confidence)*

WT	a_1	τ_1	a_2	τ_2	χ^2
oxidized	0.72 ± 0.08	90 ± 20	0.27 ± 0.06	800 ± 200	0.14
reduced	0.4 ± 0.1	70 ± 40	0.59 ± 0.05	1200 ± 200	0.69
Mutant	a_1	τ_1	a_2	τ_2	χ^2
oxidized	0.6 ± 0.1	80 ± 40	0.4 ± 0.1	900 ± 200	0.91
reduced	0.45 ± 0.04	53 ± 09	0.59 ± 0.03	870 ± 40	0.26

Table 2.2: Fitting parameters from wild-type and mutant FMO at long waiting time as shown in Fig. 2.7. Traces are fit to a biexponential of the form $a_1 e^{(-T/\tau_1)} + a_2 e^{(-T/\tau_2)}$, using a weighted nonlinear regression. Weights are determined as the inverse variance at each time point. The χ^2 column reports the reduced-χ^2, and reported fit errors are a 95% confidence interval.

Short-time fit parameters: *continued on next page*

Exciton 2-1 cross peak (all times in fs, error is 95% confidence)

WT	a_1	τ_1	a_2	τ_2	χ^2
oxidized	-0.280 ± 0.006	430 ± 20	0.436 ± 0.002	-	1.5
10pt] reduced	-0.382 ± 0.009	440 ± 20	0.512 ± 0.003	-	0.41
Mutant	a_1	τ_1	a_2	τ_2	χ^2
oxidized	-0.459 ± 0.007	660 ± 30	0.548 ± 0.007	-	0.48
reduced	-0.298 ± 0.006	580 ± 30	0.408 ± 0.004	-	0.53

Short-time fit parameters: *continued from previous page*

Exciton 4 diagonal (all times in fs, error is 95% confidence)

WT	a_1	τ_1	a_2	τ_2	χ^2
oxidized	0.634 ± 0.007	220 ± 5	0.238 ± 0.007	4000 ± 300	1.1
reduced	0.734 ± 0.009	288 ± 6	0.176 ± 0.002	-	0.75
Mutant	a_1	τ_1	a_2	τ_2	χ^2
oxidized	0.607 ± 0.009	280 ± 7	0.168 ± 0.002	-	0.91
reduced	0.414 ± 0.007	265 ± 8	0.108 ± 0.002	-	0.62

Exciton 4-2 cross peak (all times in fs, error is 95% confidence)

WT	a_1	τ_1	a_2	τ_2	χ^2
oxidized	0.125 ± 0.008	1300 ± 300	0.35 ± 0.01	-	1.1
reduced	0.29 ± 0.02	710 ± 90	0.546 ± 0.008	-	0.47
Mutant	a_1	τ_1	a_2	τ_2	χ^2
oxidized	-0.31 ± 0.02	87 ± 9	0.324 ± 0.007	6000 ± 600	0.55
reduced	0.27 ± 0.02	1600 ± 200	0.11 ± 0.02	-	0.64

Exciton 4-1 cross peak (all times in fs, error is 95% confidence)

WT	a_1	τ_1	a_2	τ_2	χ^2
oxidized	-0.628 ± 0.004	492 ± 7	0.760 ± 0.002	-	0.90
reduced	-0.842 ± 0.008	460 ± 10	0.971 ± 0.004	-	0.37
Mutant	a_1	τ_1	a_2	τ_2	χ^2
oxidized	-0.880 ± 0.009	610 ± 20	0.782 ± 0.006	-	1.2
reduced	-0.486 ± 0.008	600 ± 20	0.541 ± 0.005	-	0.52

Exciton 2 diagonal (all times in fs, error is 95% confidence)

WT	a_1	τ_1	a_2	τ_2	χ^2
oxidized	0.390 ± 0.008	560 ± 30	0.371 ± 0.005	-	2.5
reduced	0.36 ± 0.01	500 ± 30	0.455 ± 0.005	-	1.2
Mutant	a_1	τ_1	a_2	τ_2	χ^2
oxidized	0.53 ± 0.01	640 ± 30	0.241 ± 0.007	-	0.44
reduced	0.51 ± 0.01	630 ± 40	0.218 ± 0.008	-	1.0

Short-time fit parameters: *continued from previous page*

Exciton 7-4 cross peak (all times in fs, error is 95% confidence)

WT	a_1	τ_1	a_2	τ_2	χ^2
oxidized	0.264 ± 0.007	310 ± 10	0.086 ± 0.002	-	3.3
reduced	0.373 ± 0.07	290 ± 10	0.108 ± 0.002	-	0.41
Mutant	a_1	τ_1	a_2	τ_2	χ^2
oxidized	0.210 ± 0.007	400 ± 30	0.123 ± 0.003	-	1.1
reduced	0.087 ± 0.005	250 ± 20	0.026 ± 0.001	-	0.24

Table 2.3: Fitting parameters from wild-type and mutant FMO time traces at short times. Spectral locations are indicated by pump and probe exciton. Traces with values for τ_1 and τ_2 are fit via unweighted nonlinear regression to a biexponential of the form $a_1 e^{(-T/\tau_1)} + a_2 e^{(-T/\tau_2)}$, while those with only one time constant are fit to an offset exponential $a_1 e^{(-T/\tau_1)} + a_2$. The χ^2 column reports the reduced-χ^2.

2.5 Conclusions

We observe differences in the ultrafast EET in the FMO pigment-protein complex under different redox conditions that result from the presence of optically generated reactive oxygen species. The differences in EET dynamics arise primarily from differences in the system-bath coupling between BChl chromophores and protein residues. Based on recent work by Gray and Winkler [20, 21]. we speculate that the changes in ultrafast EET dynamics are strongly influenced by the redox-active Tyr/Trp chain in the vicinity of two key chromophores that affect the lowest-energy excitons in the system, a mechanism that is distinct from the previously-reported cysteine-mediated quenching mechanism. When the residues surrounding the chromophores are oxidized, they change the electronic environment in which the chromophores sit, ultimately affecting EET through the complex. The most efficient and rapid transfer through the excitonic system occurs under reducing conditions free of oxygen similar to the anaerobic conditions under which FMO operates in nature. While Tyr/Trp chains have been widely studied in enzymes that produce oxidizing intermediates during catalysis, more work needs to be done to understand the role they may play in photosynthetic pigment-protein complexes. Additionally, a redox-sensitive environment

may ultimately provide a useful handle for controlling EET in artificial/synthetic systems for light harvesting and solar-energy conversion.

REFERENCES

[1] Roderick K. Clayton and Betty J. Clayton. B850 pigment-protein complex of rhodopseudomonas sphaeroides: Extinction coefficients, circular dichroism, and the reversible binding of bacteriochlorophyll. *Proceedings of the National Academy of Sciences, USA*, 78(9):5583–5587, 1981.

[2] Zhenfeng Liu, Hanchi Yan, Kebin Wang, Tingyun Kuang, Jiping Zhang, Lulu Gui, Xiaomin An, and Wenrui Chang. Crystal structure of spinach major light-harvesting complex at 2.72 Å resolution. *Nature*, 428(6980):287–292, 2004.

[3] Thomas M. Wahlund, Carl R. Woese, Richard W. Castenholz, and Michael T. Madigan. A thermophilic green sulfur bacterium from New Zealand hot springs, *Chlorobium tepidum* sp. nov. *Archives of Microbiology*, 156(2):81–90, 1991.

[4] Robert E. Blankenship. *Molecular mechanisms of photosynthesis*. Wiley/Blackwell, Chichester, West Sussex, second edition, 2014.

[5] R. E. Fenna and B. W. Matthews. Chlorophyll arrangement in a bacteriochlorophyll protein from *Chlorobium limicola*. *Nature*, 258:573–577, 1975.

[6] Wei Min Zhang, Torsten Meier, Vladimir Chernyak, and Shaul Mukamel. Exciton-migration and three-pulse femtosecond optical spectroscopies of photosynthetic antenna complexes. *Journal of Chemical Physics*, 108(18):7763–7774, 1998.

[7] Dugan Hayes, Gitt Panitchayangkoon, Kelly A. Fransted, Justin R. Caram, Jianzhong Wen, Karl F. Freed, and Gregory S. Engel. Dynamics of electronic dephasing in the Fenna–Matthews–Olson complex. *New Journal of Physics*, 12(6):065042, 2010.

[8] Dugan Hayes and Gregory S. Engel. Extracting the excitonic hamiltonian of the Fenna-Matthews-Olson complex using three-dimensional third-order electronic spectroscopy. *Biophysical Journal*, 100(8):2043–2052, 2011.

[9] Jakub Dostál, Jakub Pšenčík, and Donatas Zigmantas. *In situ* mapping of the energy flow through the entire photosynthetic apparatus. *Nature Chemistry*, 8:715–710, 2016.

[10] Santi Nonell, Cristina Flors, and Ed. *Singlet Oxygen: Applications in Biosciences and Nanosciences*, volume 1. Royal Society of Chemistry, 2016.

[11] W.H. Orme-Johnson and H. Beinert. On the formation of the superoxide anion radical during the reaction of reduced iron-sulfur proteins with oxygen. *Biochemical and Biophysical Research Communications*, 36(6):905 – 911, 1969.

[12] B. Demming-Adams, B. Garab, W.W. Adams III, and Govindjee, editors. *Non-Photochemical Quenching and Energy Dissipation in Plants, Algae and Cyanobacteria*. Advances in Photosynthesis and Respiration. Springer Netherlands, 2014.

[13] Andrew A. Pascal, Zhenfeng Liu, Koen Broess, Bart van Oort, Herbert van Amerongen, Chao Wang, Peter Horton, Bruno Robert, Wenrui Chang, and Alexander Ruban. Molecular basis of photoprotection and control of photosynthetic light-harvesting. *Nature*, 436(7047):134–137, 2005.

[14] G. S. Orf, R. G. Saer, D. M. Niedzwiedzki, H. Zhang, C. L. McIntosh, J. W. Schultz, L. M. Mirica, and R. E. Blankenship. Evidence for a cysteine-mediated mechanism of excitation energy regulation in a photosynthetic antenna complex. *Proceedings of the National Academy of Sciences, USA*, 113(31):E4486–93, 2016.

[15] N. V. Karapetyan, T. Swarthoff, C. P. Rijgersberg, and J. Amesz. Fluorescence emission spectra of cells and subcellular preparations of a green photosynthetic bacterium. Effects of dithionite on the intensity of the emission bands. *Biochimica et Biophysica Acta (BBA) - Bioenergetics*, 593(2):254–260, 1980.

[16] Wenli Zhou, Russell LoBrutto, Su Lin, and Robert E. Blankenship. Redox effects on the bacteriochlorophyll -containing Fenna-Matthews-Olson protein from *Chlorobium tepidum*. *Photosynthesis Research*, 41(1):89–96, 1994.

[17] Rafael Saer, Gregory S. Orf, Xun Lu, Hao Zhang, Matthew J. Cuneo, Dean A. A. Myles, and Robert E. Blankenship. Perturbation of bacteriochlorophyll molecules in Fenna–Matthews–Olson protein complexes through mutagenesis of cysteine residues. *Biochim Biophys Acta - Bioenergetics*, 1857(9):1455–1463, 2016.

[18] Young-Mi Go and Dean P. Jones. The redox proteome. *Journal of Biological Chemistry*, 288(37):26512–26520, 2013.

[19] Corinne Aubert, Marten H. Vos, Paul Mathis, Andre P. M. Eker, and Klaus Brettel. Intraprotein radical transfer during photoactivation of DNA photolyase. *Nature*, 405(6786):586–590, 2000.

[20] Harry B. Gray and Jay R. Winkler. Hole hopping through tyrosine/tryptophan chains protects proteins from oxidative damage. *Proceedings of the National Academy of Sciences, USA*, 112(35):10920–10925, 2015.

[21] Harry B. Gray and Jay R. Winkler. The rise of radicals in bioinorganic chemistry. *Israel Journal of Chemistry*, 56(9-10):640–648, 2016.

[22] C. Shih, A. K. Museth, M. Abrahamsson, A. M. Blanco-Rodriguez, A. J. Di Bilio, J. Sudhamsu, B. R. Crane, K. L. Ronayne, M. Towrie, Jr. Vlcek, A., J. H. Richards, J. R. Winkler, and H. B. Gray. Tryptophan-accelerated electron flow through proteins. *Science*, 320(5884):1760–2, 2008.

[23] D. M. Jonas. Two-dimensional femtosecond spectroscopy. *Annual Review of Physical Chemistry*, 54:425–63, 2003.

[24] Shaul Mukamel. Multidimensional femtosecond correlation spectroscopies of electronic and vibrational excitations. *Annual Review of Physical Chemistry*, 51(1):691–729, 2000.

[25] John D. Hybl, Allison W. Albrecht, Sarah M. Gallagher Faeder, and David M. Jonas. Two-dimensional electronic spectroscopy. *Chemical Physics Letters*, 297(3):307–313, 1998.

[26] Minhaeng Cho, Harsha M. Vaswani, Tobias Brixner, Jens Stenger, and Graham R. Fleming. Exciton analysis in 2D electronic spectroscopy. *Journal of Physical Chemistry B*, 109(21):10542–10556, 2005.

[27] Jianzhong Wen, Hao Zhang, Michael L. Gross, and Robert E. Blankenship. Membrane orientation of the FMO antenna protein from *chlorobaculum tepidum* as determined by mass spectrometry-based footprinting. *Proceedings of the National Academy of Sciences, USA*, 106(15):6134–6139, 2009.

[28] Yi-Fen Li, Wenli Zhou, Robert E. Blankenship, and James P. Allen. Crystal structure of the bacteriochlorophyll a protein from *chlorobium tepidum*. *Journal of Molecular Biology*, 271(3):456 – 471, 1997.

[29] Paolo D. Gerola and John M. Olson. A new bacteriochlorophyll a-protein complex associated with chlorosomes of green sulfur bacteria. *Biochimica et Biophysica Acta (BBA) - Bioenergetics*, 848(1):69 – 76, 1986.

[30] Jianzhong Wen, Hao Zhang, Michael L. Gross, and Robert E. Blankenship. Native electrospray mass spectrometry reveals the nature and stoichiometry of pigments in the FMO photosynthetic antenna protein. *Biochemistry*, 50(17):3502–3511, 2011.

[31] Elad Harel, Andrew F. Fidler, and Gregory S. Engel. Real-time mapping of electronic structure with single-shot two-dimensional electronic spectroscopy. *Proceedings of the National Academy of Sciences*, 107(38):16444–16447, 2010.

[32] Elad Harel, Andrew F. Fidler, and Gregory S. Engel. Single-shot gradient-assisted photon echo electronic spectroscopy. *Journal of Physical Chemistry A*, 115(16):3787–3796, 2011.

[33] Peter D. Dahlberg, Andrew F. Fidler, Justin R. Caram, Phillip D. Long, and Gregory S. Engel. Energy transfer observed in live cells using two-dimensional electronic spectroscopy. *The Journal of Physical Chemistry Letters*, 4(21):3636–3640, 2013.

[34] VV Lozovoy, I Pastirk, and M Dantus. Multiphoton intrapulse interference. 4. characterization of the phase of ultrashort laser pulses. *Opt. Lett.*, 29:775–777, 2004.

[35] S.H. Sohail, P. D. Dahlberg, M. A. Allodi, P.C. Ting, S.C. Massey, E.C. Martin, C.N. Hunter, and G. S. Engel. Communication: Broad manifold of excitonic states in light-harvesting complex 1 promotes efficient unidirectional energy transfer *in vivo*. *Journal of Chemical Physics*, 147:131101, 2017.

[36] P. D. Dahlberg, P.C. Ting, S.C. Massey, M. A. Allodi, E. C. Martin, C. N. Hunter, and G. S. Engel. Mapping the ultrafast flow of harvested solar energy in living photosynthetic cells. *Nature Communications*, 8:988, 2017.

[37] Stephen G. Mayhew. The redox potential of dithionite and SO_2 from equilibrium reactions with flavodoxins, methyl viologen and hydrogen plus hydrogenase. *European Journal of Biochemistry*, 85(2):535–547, 1978.

[38] Tobias Brixner, Jens Stenger, Harsha M. Vaswani, Minhaeng Cho, Robert E. Blankenship, and Graham R. Fleming. Two-dimensional spectroscopy of electronic couplings in photosynthesis. *Nature*, 434(7033):625–628, 2005.

[39] Erling Thyrhaug, Karel Žídek, Jakub Dostál, David Bína, and Donatas Zigmantas. Exciton structure and energy transfer in the Fenna–Matthews–Olson complex. *Journal of Physical Chemistry Letters*, 7(9):1653–1660, 2016.

[40] Ramamurti Shankar. *Principles of Quantum Mechanics*. Springer, 2012.

[41] S. Mukamel. *Principles of nonlinear optical spectroscopy*. Oxford series in optical and imaging sciences. Oxford University Press, New York, 1995.

[42] Seth Lloyd, Vazrik Chiloyan, Yongjie Hu, Samuel Huberman, Zi-Wen Liu, and Gang Chen. No energy transport without discord. arXiv, 2015.

[43] Andrew F Fidler, Justin R Caram, Dugan Hayes, and Gregory S Engel. Towards a coherent picture of excitonic coherence in the Fenna–Matthews–Olson complex. *Journal of Physics B: Atomic, Molecular and Optical Physics*, 45(15):154013, 2012.

[44] Emily E. Fenn and M. D. Fayer. Extracting 2D IR frequency-frequency correlation functions from two component systems. *Journal of Chemical Physics*, 135(7):074502, 2011.

[45] Graham R. Fleming and Minhaeng Cho. Chromophore-solvent dynamics. *Annual Review of Physical Chemistry*, 47(1):109–134, 1996.

[46] Mi Kyung Lee and David F. Coker. Modeling electronic-nuclear interactions for excitation energy transfer processes in light-harvesting complexes. *Journal of Physical Chemistry Letters*, 7(16):3171–3178, 2016.

[47] Michael J. Davies. The oxidative environment and protein damage. *Biochim Biophys Acta - Proteins Proteomics*, 1703(2):93–109, 2005.

[48] Cecilia Tommos, Jack J. Skalicky, Denis L. Pilloud, A. Joshua Wand, and P. Leslie Dutton. *De Novo* proteins as models of radical enzymes. *Biochemistry*, 38(29):9495–9507, 1999.

[49] E. R. Stadtman and R. L. Levine. Free radical-mediated oxidation of free amino acids and amino acid residues in proteins. *Amino Acids*, 25(3):207–218, 2003.

[50] Stéphanie Valleau, Romain A. Studer, Florian Häse, Christoph Kreisbeck, Rafael G. Saer, Robert E. Blankenship, Eugene I. Shakhnovich, and Alán Aspuru-Guzik. Absence of selection for quantum coherence in the Fenna–Matthews–Olson complex: A combined evolutionary and excitonic study. *ACS Central Science*, 3(10):1086–1095, 2017.

[51] S Karlin and P Bucher. Correlation analysis of amino acid usage in protein classes. *Proceedings of the National Academy of Sciences, USA*, 89(24):12165–12169, 1992.

[52] SK Burley and GA Petsko. Aromatic-aromatic interaction: a mechanism of protein structure stabilization. *Science*, 229(4708):23–28, 1985.

[53] Esteban Lanzarotti, Rolf R. Biekofsky, Darío A. Estrin, Marcelo A. Marti, and Adrián G. Turjanski. Aromatic–aromatic interactions in proteins: Beyond the dimer. *Journal of Chemical Information and Modeling*, 51(7):1623–1633, 2011.

[54] Matteo Ballottari, Julien Girardon, Nico Betterle, Tomas Morosinotto, and Roberto Bassi. Identification of the chromophores involved in aggregation-dependent energy quenching of the monomeric Photosystem II antenna protein Lhcb5. *Journal of Biological Chemistry*, 285(36):28309–28321, 2010.

[55] Matteo Ballottari, Julien Girardon, Luca Dall'Osto, and Roberto Bassi. Evolution and functional properties of photosystem II light harvesting complexes in eukaryotes. *Biochim Biophys Acta - Bioenergetics*, 1817(1):143–157, 2012.

CHAPTER 3

DISENTANGLEMENT OF EXCITED-STATE DYNAMICS WITH IMPLICATIONS FOR FRET MEASUREMENTS: TWO-DIMENSIONAL ELECTRONIC SPECTROSCOPY OF A BODIPY-FUNCTIONALIZED CAVITAND

Förster Resonance Energy Transfer (FRET) is the incoherent transfer of an electronic excitation from a donor fluorophore to a nearby acceptor. FRET has been applied as a probe of local chromophore environments and distances on the nanoscale by extrapolating transfer efficiencies from standard experimental parameters, such as fluorescence intensities or lifetimes. Competition from nonradiative relaxation processes is often assumed to be constant in these extrapolations, but in actuality, this competition depends on the donor and acceptor environments and can, therefore, be affected by conformational changes. To study the effects of nonradiative relaxation on FRET dynamics, we perform two dimensional electronic spectroscopy (2DES) on a pair of azaboraindacene (BODIPY) dyes, attached to opposite arms of a resorcin[4]arene cavitand. Temperature-induced switching between two equilibrium conformations, *vase* at 294 K to *kite* at 193 K, increases the donor-acceptor distance from 0.5 nm to 3 nm, affecting both FRET efficiency and nonradiative relaxation. By disentangling different dynamics based on lifetimes extracted from a series of 2D spectra, we independently observe nonradiative relaxation, Förster energy transfer (FRET), and residual fluorescence from the donor in both *vase* to *kite* conformations. We observe changes in both FRET rate and nonradiative relaxation when the molecule switches from *vase* to *kite*, and measure a significantly greater difference in transfer efficiency between conformations than would be determined by standard lifetime-based measurements. These observations show

The research described in this chapter has been published in: J. P. Otto*, L. Wang*, I. Pochorovski, S. M. Blau, A. Aspuru-Guzik, Z. Bao, G. S. Engel, and M. Chiu. Disentanglement of excited-state dynamics with implications for FRET measurements: Two-dimensional electronic spectroscopy of a BODIPY-functionalized cavitand. *Chem. Sci.* 9(15):3694-3703, 2018. Reproduced with permission.

that changes in competing nonradiative processes must be taken into account when highly accurate measurements of FRET efficiency are desired.

3.1 Förster Resonance Energy Transfer

Förster Resonance Energy Transfer (FRET) moves an excitation nonradiatively from a donor fluorophore to a nearby acceptor via dipole-dipole interactions [1, 2]. FRET can be elegantly described by readily accessible experimental parameters, such as the distance between chromophores (R), the fluorescence spectrum of the donor, and the absorption spectrum of the acceptor [3]. The mechanism's well known R^{-6} distance dependence has led to widespread application [4, 5] of FRET as a spectroscopic measure of distances on the single nanometer scale [6, 7]. In particular, FRET is often used to probe interactions between biomolecules such as proteins [7, 8, 9, 10, 11] and DNA [12, 13, 14, 15] and to image those interactions within cells [16, 17, 18, 19, 20, 21, 22]. An extensive array [9, 15, 23, 24, 25, 26, 27, 28, 29] of donor-acceptor pairs have been developed for these purposes.

In Förster's model, the coupling between the donor and acceptor electronic states is treated as a second order perturbation in the electronic coupling. The interaction is governed by the transition dipole moments of the excited electronic states. The coupling is sufficiently weak (and the transfer rate therefore sufficiently slow) that the donor relaxes to thermal vibrational equilibrium in its electronic excited state before transfer can occur. Although no absorption or emission occurs in the transfer itself (FRET is nonradiative), the same transition dipoles that are responsible for donor emission and acceptor absorption also drive the transfer, so resonance can be determined by absorption and emission spectra, and transfer competes with donor fluorescence and nonradiative relaxation.

Experimentally, FRET efficiency can be determined by photon counts of donor or acceptor fluorescence or by changes in the donor's decay lifetime [21, 30]. The latter approach is often preferred due to relative immunity to cross-talk and concentration artifacts, [8, 20, 23] and is based on kinetic competition of decay processes, leading to equations for efficiency

such as

$$E = 1 - \frac{\tau_{DA}}{\tau_D} = \frac{1}{1 + (R/R_0)^6} \tag{3.1}$$

where τ_D and τ_{DA} are measured lifetimes of the donor alone and in the presence of the acceptor, R is the donor-acceptor distance, and R_0 is the distance at which the transfer rate is equal to τ_D, corresponding to 50% transfer [10, 22]. The donor lifetime depends on the relative rates of competing processes as

$$\frac{1}{\tau_D} = k_D = k_{D,f} + k_{D,nr} \tag{3.2}$$

$$\frac{1}{\tau_{DA}} = k_{DA} = k_{D,f} + k_{D,nr} + k_{tr} \tag{3.3}$$

where $k_{D,f}$, $k_{D,nr}$, and k_{tr} correspond to fluorescence, nonradiative relaxation, and energy transfer. Lifetime based FRET determinations of this nature rely on assumptions that all processes involved are in kinetic competition, and that processes other than FRET, i.e. nonradiative relaxation, behave similarly for the donor regardless of the donor-acceptor distance [31]. However, local solvation conditions and system-bath coupling can change as molecular conformation changes. Such changes can break the assumptions above and frustrate accurate measurement of FRET efficiency. We demonstrate this scenario using 2D electronic spectroscopy and show how nonradiative processes affect FRET measurements.

To investigate the interactions between nonradiative relaxation and FRET, we sought a pair of chromophores that undergo both excited-state processes. Moreover, we sought a means of exerting control over both the distance separating the chromophore pair and the vibrational bath that defines the local environment of each chromophore. Quinoxaline-bridged resorcin[4]arene cavitands emerged as ideal molecular scaffolds for fulfilling the latter requirement, as these conformational switches can be toggled between a pursed *vase* state and a ringent *kite* state using various external stimuli, including temperature [32, 33]. Due to solvation-related entropic effects, the cavitand exists in the *vase* conformation at room

temperature and above; conformational switching commences at *ca.* 223 K, and at 193 K, only the *kite* conformation is observed [34]. To adapt this scaffold for our studies, we sought to append each of a pair of chromophores to opposing walls of the cavitand [35, 36, 37]. We selected a pair of arylethynyl-functionalized azaboraindacene (BODIPY) chromophores for this purpose because they exhibit the requisite photophysical properties [38, 39, 40], and because both a donor and an acceptor chromophore are conveniently accessible from a single, divergent synthetic route [41].

Given the ability of 2DES measurements to elucidate ultrafast transfer and relaxation dynamics in both biological [42, 43, 44] and synthetic [45, 46, 47] systems, we sought to study the BODIPY-functionalized cavitand using this technique. By separating the signal based on time dynamics, we disentangle three relaxation pathways (nonradiative relaxation, energy transfer, and residual fluorescence) and isolate their lineshapes from the donor in both conformations (kite at 193 K and *vase* at 294 K). Based on our signal isolation analysis, we observe that the contribution of nonradiative relaxation to the overall donor decay changes with conformation. We show that, due to this change in nonradiative relaxation, fluorescence lifetime measurements underreport the transfer efficiency difference between *kite* and *vase* conformations, highlighting the need to test assumptions about nonradiative processes when measuring FRET in complex environments.

3.2 Synthesis, Variable-Temperature Characterization, and Computed Structures of the BODIPY-Functionalized Resorcin[4]arene Cavitand

Synthesis of the target cavitand **1**, a new compound, was designed based on various precedents in the BODIPY and resorcin[4]arene literatures as indicated below. The process commenced with preparation of BODIPY-functionalized walls **2a** and **2b** (Figure 3.1). Condensation of commercially available nitrobenzaldehyde **3** with 2,4-dimethylpyrrole (**4**)

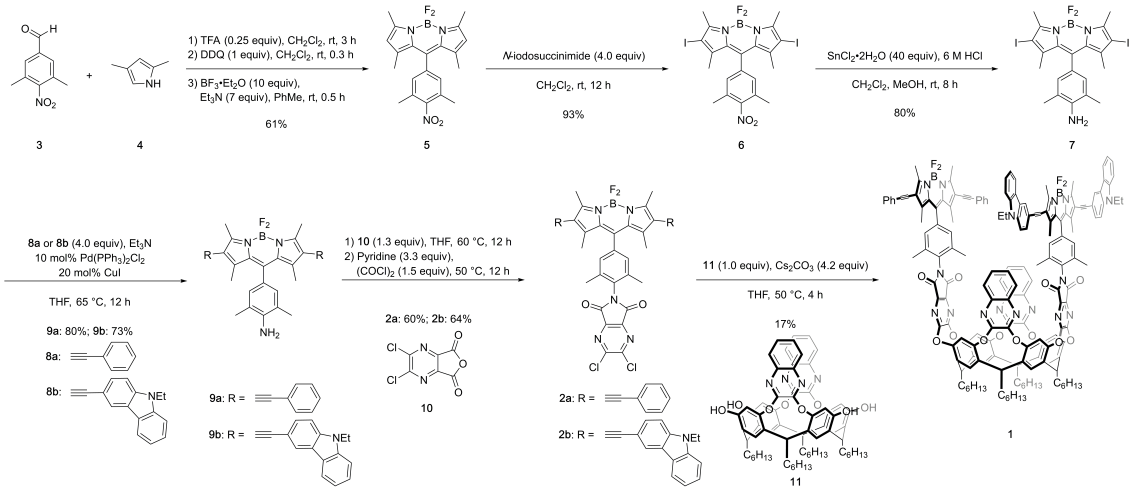

Figure 3.1: Synthesis of cavitand **1**

provided the nitro-BODIPY core **5** [48]. Treatment of nitro-BODIPY **5** with 4 equiv N-iodosuccinimide yielded diiodo-BODIPY **6**, which was subsequently converted to anilino-BODIPY **7** using stannous chloride to selectively reduce the nitro moiety without affecting the iodides [49]. Sonogashira cross-coupling of anilino-BODIPY **7** with phenylacetylene (**8a**) yielded donor dye **9a**; acceptor dye **9b** was prepared analogously using N-ethylcarbazoyl alkyne **8b** [41]. Condensation of donor dye **9a** and acceptor dye **9b** with anhydride **10** afforded walls **2a** and **2b**, respectively [35]. Final assembly of cavitand **1**, which involves four nucleophilic substitutions, was achieved in a one-pot procedure with 17% yield, wherein a mixture of tetrol **11** and both walls, **2a** and **2b**, were treated with cesium carbonate. Target cavitand **1** was purified from the resultant mixture using flash column chromatography, followed by recycling gel permeation chromatography. The successful installation of two different walls on tetrol **11** in one pot to access cavitand **1** represents an alternative to previously reported consecutive installation methods for synthesizing non-symmetrically-substituted resorcin[4]arene cavitands. This new method eliminates the need for multiple purification steps which reduce overall yield [35].

Temperature-dependent conformational behavior of cavitand **1** was characterized by variable-temperature 1H NMR [34], absorption, and fluorescence spectroscopies [35]. As

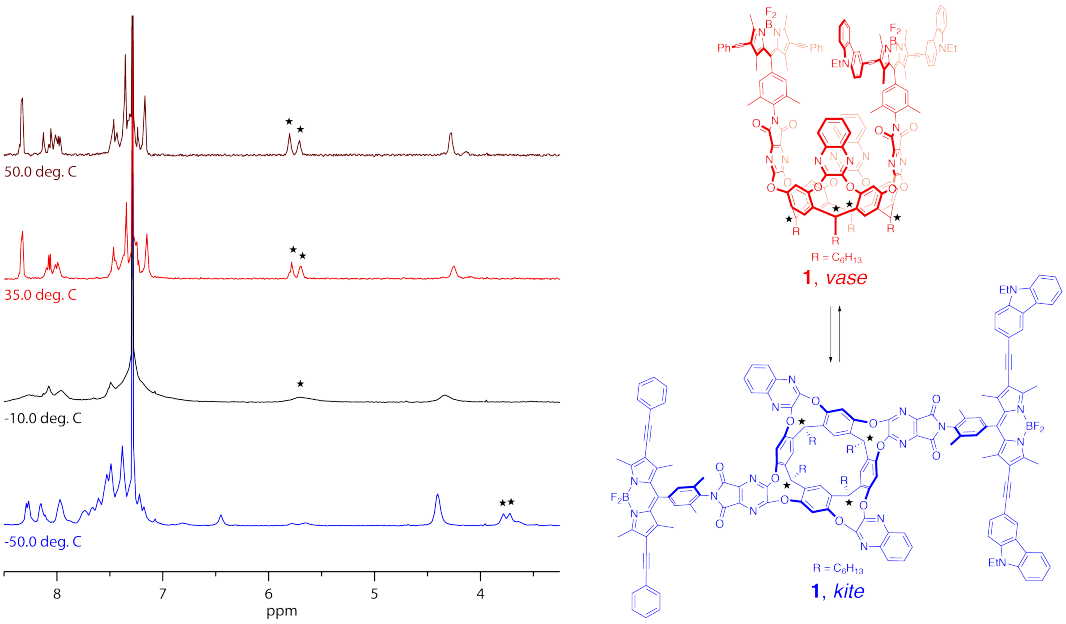

Figure 3.2: ^{1}H NMR spectra of cavitand **1** in $CDCl_3$ at various temperatures.

shown in Figure 1, the ^{1}H NMR spectrum of cavitand **1** at 323 K exhibits two sets of sharp multiplets between 5.7 and 5.8 ppm, corresponding to the resorcin[4]arene methine protons ($\star$) and are indicative of the *vase* conformation. Cooling the sample to 223 K resulted in a diagnostic upfield shift of these methine proton signals to *ca.* 3.8 ppm due to increased shielding from the proximity of the aromatic wall flaps in the *kite* conformation. Consistent with previous reports, the *vase*-to-*kite* transition was also observed upon addition of acid [35].

The temperature-dependent conformational switching of cavitand **1** was corroborated by fluorescence and absorption spectroscopies, as depicted in Figure 3.3. The *vase* conformation of cavitand **1** predominates at 294 K (Figure 3.3a), evidenced by a blue-shift of the absorption maximum of cavitand **1** relative to that of the dye mixture; interactions between the donor and acceptor dyes in the *vase* conformation of cavitand **1** result in shifts of their ground- and excited-state energies. At 193 K, the absorption spectrum of cavitand **1** resembles that of the dye mixture, which is consistent with the lack of interaction between the donor and acceptor dyes in the *kite* conformation (Figure 3.3b). Fluorescence spectra of the cavitand **1**

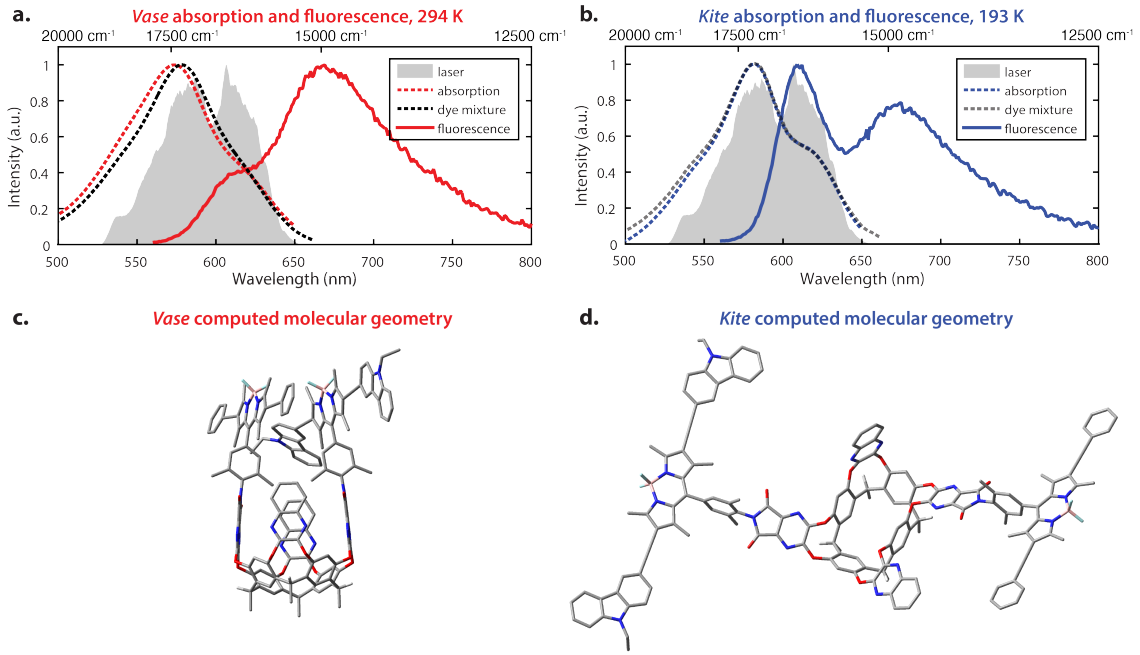

Figure 3.3: Optical properties and corresponding calculated structures of the *vase* and *kite* conformations of cavitand **1**. a) Absorption (red dashed line) and fluorescence (solid line, excitation at 525 nm) of cavitand **1** in the *vase* conformation at 294 K; absorption of donor-acceptor mixture, 1:1 molar ratio at 294 K (black dashed line); laser spectrum (filled grey area). b) Absorption (blue dashed line) and fluorescence (solid line, excitation at 525 nm) of cavitand **1** in the *kite* conformation at 193 K; absorption of donor-acceptor mixture, 1:1 molar ratio at 193 K (dark grey dashed line); laser spectrum (filled grey area). c) Optimized geometry of the *vase* conformation calculated at the B3LYP/3-21G(d) level of theory. d) Optimized geometry of the *kite* conformation calculated at the B3LYP/3-21G(d) level of theory. In c and d, terminal C_6H_{13} groups have been replaced with CH_3.

at 294 K and 193 K (excitation at 525 nm for both conformations) show a clear increase in donor emission at 610 nm with a concurrent decrease in acceptor emission at 670 nm as the temperature is lowered. These fluorescence changes indicate a decrease in FRET efficiency and an increase in the distance between the donor and acceptor dye at lower temperature, which is consistent with conversion of *vase* to *kite* with decreasing temperature.

Computational studies provided further structural insights into the two conformations of cavitand **1**. The geometries of the *vase* and *kite* conformations were optimized using density functional theory calculations (B3LYP/3-21G(d)) in the Gaussian 09 software package [50], and are depicted in Figure 3.3c-d, respectively. In both configurations, terminal C_6H_{13} groups have been replaced with CH_3. In the *vase* conformation, the donor and acceptor are sterically constrained to an orientation that promotes dipole-dipole coupling. The donor-acceptor distance in the *vase* conformation is *ca.* 0.5 nm, which is too close for independent solvation of the two chromophores, suggesting that they interact vibrationally, as well as electronically. In contrast, the donor and acceptor are separated by *ca.* 3 nm in the *kite* conformation, providing the chromophores with relative orientational freedom. Although the donor and acceptor are separated by less than R_0, they interact weakly enough that the approximations made by FRET theory accurately describe their interaction. Having successfully synthesized cavitand **1** and confirmed that its conformation and transfer dynamics could be externally controlled by temperature, we next sought to probe the excited-state dynamics of cavitand **1**, focusing on the interactions between nonradiative relaxation and FRET processes.

3.3 Two-Dimensional Electronic Spectroscopy

Two-dimensional electronic spectroscopy (2DES) is a four-wave mixing technique that uses three ultrafast pulses at controlled time delays to interact with a sample, generating a third-order nonlinear signal. Two frequency axes, ω_τ and ω_t, are produced via Fourier transformation over the first and third time delays (coherence time, τ, and rephasing time, t). These

axes represent the frequencies of excitation and detection, respectively, and correspond to the horizontal (ω_τ) and vertical (ω_t) axes on all 2D spectra shown in this paper. Plotted as the change in transmitted light (ΔT), positive features can be attributed to stimulated emission (SE) or to ground state bleach (GSB; a decrease in absorption caused by depletion of the ground state population). Negative features are due to excited state absorption (ESA). Signal recorded at a series of waiting times T can reveal the time dynamics of the interrogated sample over 5-6 orders of magnitude, ranging from femtoseconds to nanoseconds.

2D spectra are frequency-frequency correlation maps, describing the optical response of a system (recorded on ω_t axis) at a series of waiting times, T, after initial excitation at ω_τ. Signals along the diagonal indicate features detected at the same energy as their excitation, while signals above or below the diagonal indicate coupling or population transfer between excited states. Additionally, the lineshapes of 2D signals provide information on the mechanisms that lead to broad spectral signals [51]. Inhomogeneous broadening (extension along the diagonal) gives insight into static variation in chemical environments, which perturb the excitation energies of individual chromophores [52]. In contrast, homogeneous broadening (which determines antidiagonal linewidth) occurs when frequency fluctuations due to bath interactions occur quickly compared with the experimental timescale, such that an individual chromophore experiences all configurations of its local environment during a given measurement and thus represents the entire ensemble [53]. In the homogeneous limit, one can estimate the dephasing time of a transition (the time required to lose phase correlation in the ensemble of sample molecules) by its homogeneous linewidth [54].

3.4 Two-Dimensional Electronic Spectra of the BODIPY-Functionalized Cavitand

We performed 2DES measurements on cavitand **1** at both 193 K and 294 K in two sets of waiting times: one from -20 to 1000 fs with a 10 fs stepsize, and the other from -5 to

800 ps with a 5 ps stepsize. Representative real-valued 2D spectra for the *kite* and *vase* conformations of the dimer are shown in Figure 3.4, which contains logarithmically spaced time series and highlights time points for comparison. The 2D spectra of each conformation in Figure 3.4c are normalized to the maximum of 2D spectrum at T=0 fs in both datasets, and the frames in the highlighted spectra (Figure 3.4a, Figures 3.4b, Figure 3.4d, and Figure 3.4e) are normalized individually.

At T=20 fs, 2D spectra of both *vase* (Figure 3.4a) and *kite* (Figure 3.4d) show an inhomogeneously broadened peak along the diagonal at roughly 17100 cm^{-1}. This signal corresponds to the initial absorption of the donor, because at 20 fs the system has not yet relaxed past this starting point. Vibrational relaxation (aka Stokes shift) from this initial absorption occurs within the first 100 fs, leading to the below diagonal cross peak in all subsequent spectra.

At T=260 ps (Figures 3.3b and e), two dominant features are present in both 2D spectra —a diagonal peak at 17100 cm^{-1} (white star) and a crosspeak at 17100 cm $^{-1}$ (585 nm) in ω_τ and 16400 (610 nm) cm^{-1} in ω_t (black star). The diagonal feature at T=260 ps is due to ground state bleach on the donor, because Stokes shift from the initial excitation has completed by this time. The below-diagonal crosspeak corresponds primarily to stimulated emission from the Stokes shifted excited state of the donor. Along the anti-diagonal direction, all features are very broad along the anti-diagonal direction, indicating the homogeneity of excited donor molecules. The width of these homogeneously broadened features is caused by rapid dephasing on the scale of tens of fs (Figure 3.7). A red shift in early time dynamics of the complex occurs on the same timescale, (see Figure 3.8) and the processes driving the red shift may also be the cause of this rapid dephasing.

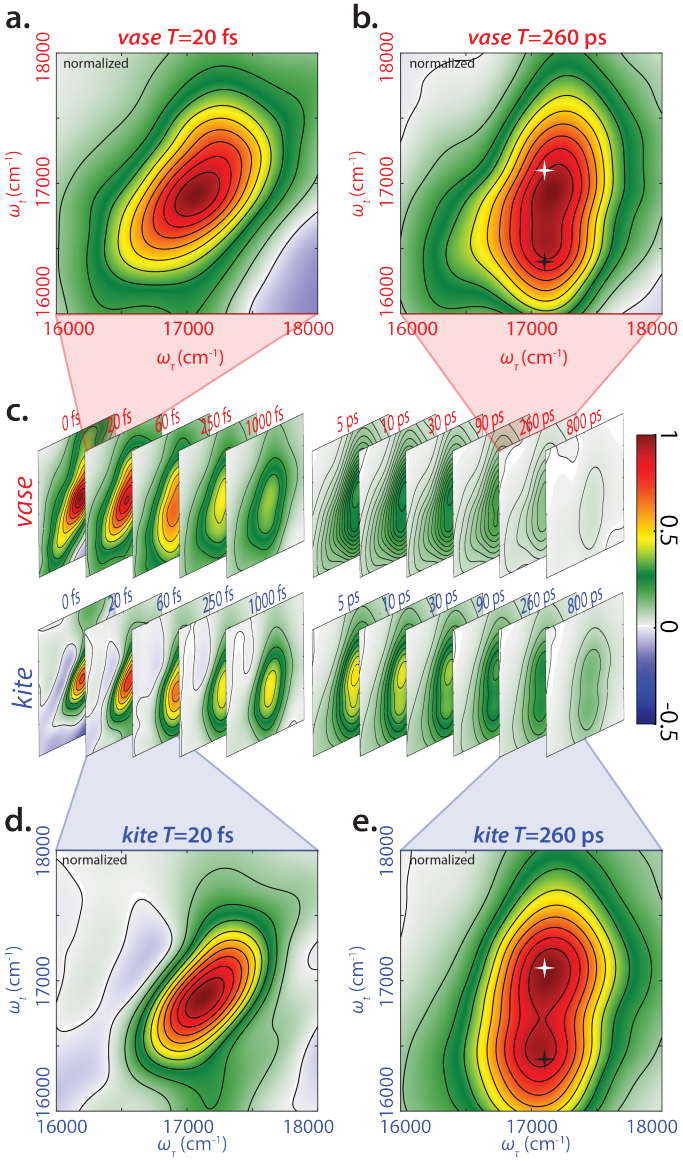

Figure 3.4: Representative real-valued phased 2DES spectra for *vase*/*kite* conformation. (a) 2DES spectra of *vase* at 20 fs waiting time. (b) 2DES spectra of *vase* at 260 ps waiting time. Highlighted points are 17100 cm^{-1} (585 nm) diagonal (white star) and crosspeak (black star) at the same ω_τ (17100 cm^{-1}, 585 nm) and ω_t of 16400 cm^{-1} (610 nm). (c) Time series of 2D spectra ranging 0-1000 fs and 5-800 ps for both *vase* and *kite*, normalized to T=0. An expanded version can be seen in Figure 3.15. (d) 2DES spectra of *kite* at 20 fs waiting time. (e) 2DES spectra of *kite* at 260 ps waiting time, with same highlights as in b. Spectra in a and d are normalized independently for the two conformations at 20 fs, while spectra b and e are normalized independently for the two conformations at 260 ps. The growth of the cross peak (black star, 17100 cm^{-1} in ω_τ and 16400 cm^{-1} in ω_t) corresponds to donor relaxation to donor fluorescence as well as FRET transfer to acceptor absorption during waiting time.

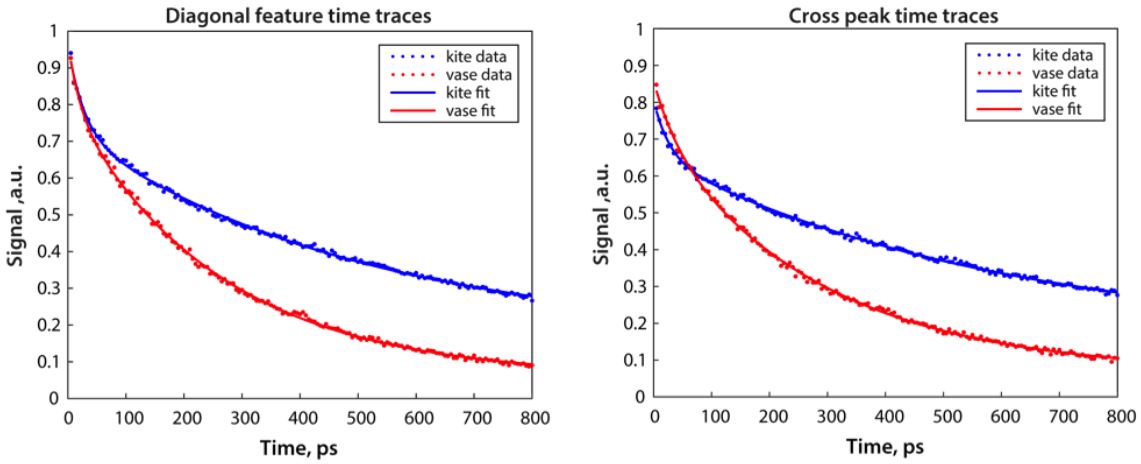

Figure 3.5: Representative picosecond time traces from the diagonal at 17100 cm^{-1} and at the cross peak at 17100 cm^{-1} and 16400 cm^{-1}, corresponding to white and black indicators in Figure 3.4 Fit parameters are listed in table 3.1.

diagonal	A_1	τ_1 (ps)	A_2	τ_2 (ps)	A_3
RT	0.17 ± 0.02	20 ± 3	0.746 ± 0.007	261 ± 7	0.059 ± 0.005
-80°C	0.23 ± 0.01	27 ± 3	0.568 ± 0.009	500 ± 30	0.16 ± 0.01
crosspeak	A_1	τ_1 (ps)	A_2	τ_2 (ps)	A_3
RT	0.14 ± 0.03	40 ± 20	0.66 ± 0.03	290 ± 20	0.06 ± 0.01
cold	0.15 ± 0.02	27 ± 8	0.50 ± 0.03	600 ± 90	0.15 ± 0.04

Table 3.1: Fit parameters with 95% confidence intervals for time traces shown in Figure 3.5.

3.5 Decay-Associated Spectra

Decay-associated spectra (DAS) are generated from global fitting of the decay dynamics of each pixel in a 2D spectrum, and quantifying the contributions of various pathways to the overall signal. This and similar approaches have previously been applied to 2D spectra by the Engel group [55] and others [56, 57]. We performed DAS analysis on the long waiting time (5 ps resolved) 2D data, specifically from 5 ps to 800 ps. The waiting time decay dynamics were fit to the following equation

$$S(T) = A_1 e^{-T/\tau_1} + A_2 e^{-T/\tau_2} + A_3 \tag{3.4}$$

where τ_1 and τ_2 are globally optimized decay constants for different transfer or relaxation processes (see table 3.3). The A_i values correspond to the contribution of each process with A_3 corresponding to the contribution of signals with decay constant $\tau_3 \gg 800$ ps (our experimental timescale). A detailed description of how the maps are generated can be found in the methods section at the end of this chapter.

The left (grey) column in Figure 3.6 shows a fast ($\sim$ 25ps) decay for the cavitand **1** in the *vase* (294 K, top) and *kite* (193 K, bottom) conformations. These lifetimes are consistent with reports of a decay in the 15-30 ps range for analogous meso-aryl substituted boron dipyrrin structures [38, 39]. We assign this fast decay to a nonradiative, vibrationally driven relaxation arising from a combination of flexing in the dipyrrin backbone and from rotation

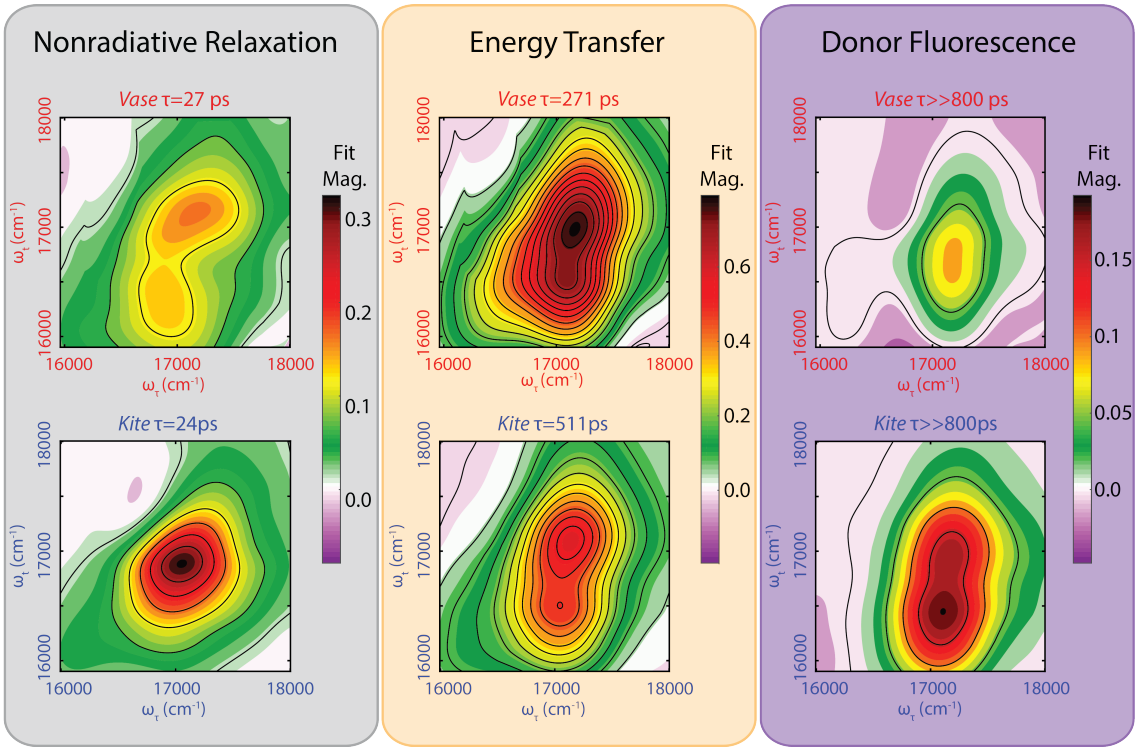

Figure 3.6: Decay-associated spectra (DAS) reveal lineshapes of decay dynamics. DAS demonstrate relative distribution and strength (indicated by colorbar) of features decaying at the labeled rate. Sum of all DAS for a given conformation equals the normalized real-valued 2D spectra at T = 5 ps. The grey, yellow, and purple columns correspond to nonradiative relaxation, energy transfer (FRET), and donor fluorescence processes respectively.

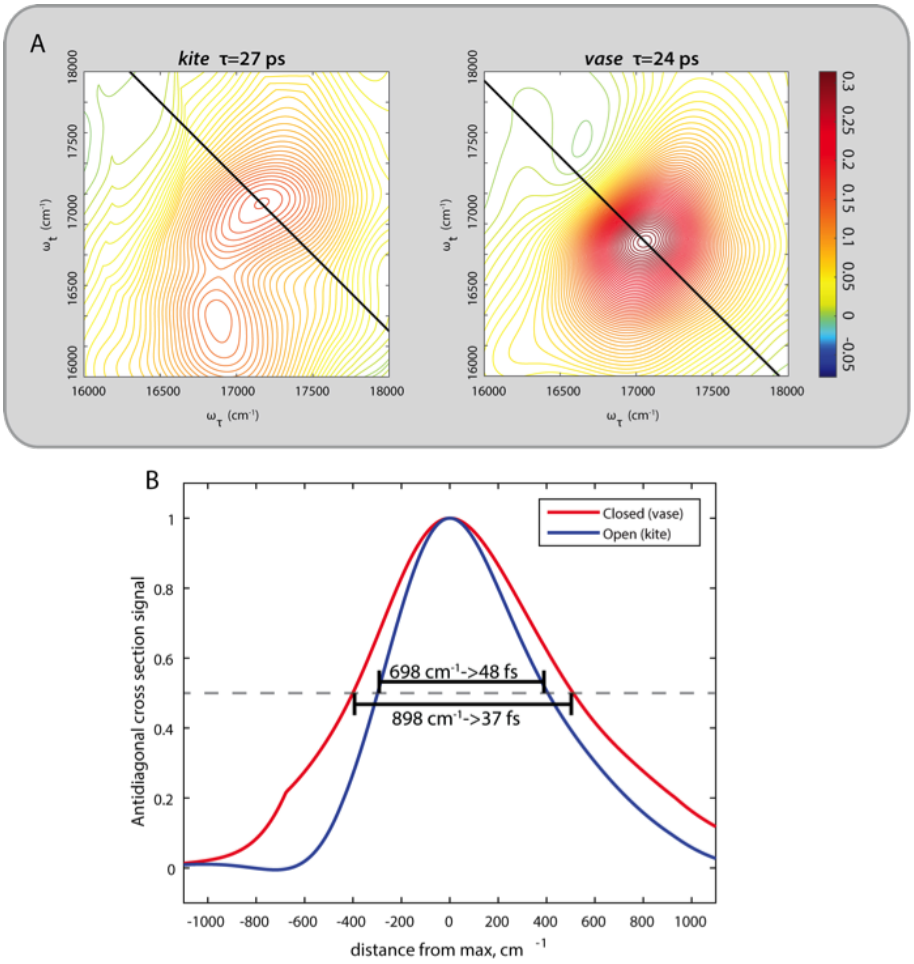

Figure 3.7: Dephasing lifetimes derived from nonradiative relaxation signals. (a) Nonradiative relaxation lifetime maps of *kite* and *vase* conformation. The top figures show the same data as Figure 3.10 in the main text, overlaid with location of antidiagonal cut, which is aligned with max signal. (b) Antidiagonal profile with inset FWHM and corresponding dephasing lifetimes, calculated as the inverse of the frequency FWHM. [54]

of the aryl group as suggested by Li *et al.* [38] and Kee *et al.* [39]. The multi-exponential nature of the decay means that this process (corresponding to the fastest exponential decay) does not compete kinetically with the processes observed in the other two exponential decays. This observation may be explained by a multi-well potential energy surface for the excited donor, as illustrated in Figure 4 and observed by Li *et al.* [38].

While the lifetimes of this nonradiative relaxation pathway are very similar for both conformations, the corresponding lineshapes in the 2D lifetime map differ notably. In the *kite* spectrum (Figure 3.6, lower left plot, grey), the signal is primarily due to one homogeneously

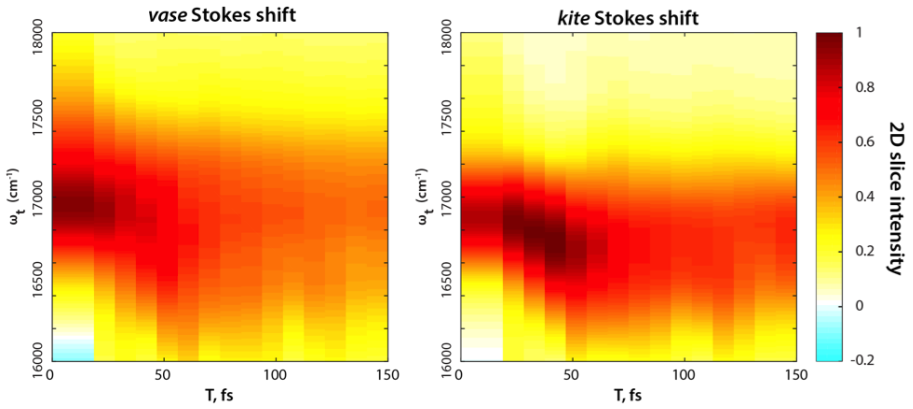

Figure 3.8: Stokes shift in *vase* and *kite* measured by ultrafast 2DES. A vertical slice of the 2D spectrum taken at ω_τ =17100 cm^{-1} from 0 to 150 fs waiting time is shown. Vertical axis ω_t is the same as in all other 2D spectra shown. Initial excitations relax on the order of 30-50 fs, consistent with dephasing lifetimes calculated from Figure 3.7.

broadened feature at 17000 cm^{-1}. The antidiagonal full width at half maximum (FWHM) of this feature corresponds to a homogeneous process with a dephasing lifetime of 48 fs, coincident with the timescale of relaxation within the electronic excited state as seen via Stokes shift in femtosecond resolved 2DES (Figure 3.7 and 3.8). By comparison, the *vase* spectrum (Figure 3.6, upper left plot) shows an inhomogeneously broadened diagonal feature at 17100 cm^{-1}, as well as a crosspeak feature at an excitation frequency of 17000 cm^{-1} and detection frequency of 16400 cm^{-1}. Inhomogeneous broadening indicates that subsections of the sample population have differing energetic environments, such as those arising from conformational variation, that persist on the timescale of the experiment.

The middle (orange) column in Figure 3.6 represents the strength of signal that decays with a lifetime of several hundred ps. This decay lifetime is not observed in fluorescence lifetime measurements of the donor solution. We assign this signal to energy transfer between donor and acceptor (FRET). The energy of the diagonal feature matches with GSB from the donor, while the energy of the below-diagonal feature matches SE from the Stokes-shifted excited donor, as well as the absorption of the acceptor. Both features decay due to FRET transfer to the acceptor. Because the initial vibrational relaxation in the donor excited state is complete within 100 fs, all signal at the diagonal observed on this timescale is due to GSB

of the donor, meaning that only the loss of donor excitation is observed. The below-diagonal features may contain signal from the acceptor and have longer lifetimes than features on the diagonal (Table 3.1 and Figure 3.5). Hence, the diagonal feature is used for donor lifetime measurements. This FRET transfer pathway contributes to the majority of the signal, particularly in the *vase* conformation where the chromophores are in close proximity to one another.

The right (purple) column in figure 3.6 shows the portion of the 2D signal that does not decay on the timescale of 800 ps. We assign this signal to residual donor fluorescence based on the measured fluorescence lifetime of the donor (2-3 ns, Figure 3.12). The double peak lineshape of this signal can be described by a combination of GSB at the diagonal (corresponding to the original absorption) and SE at the crosspeak (corresponding to Stokes shifted emission). Simulated spectra generated from the absorption and fluorescence of the donor alone (Figure 3.9) qualitatively match the lineshape of this long-lived signal for both conformations, further supporting our assignment.

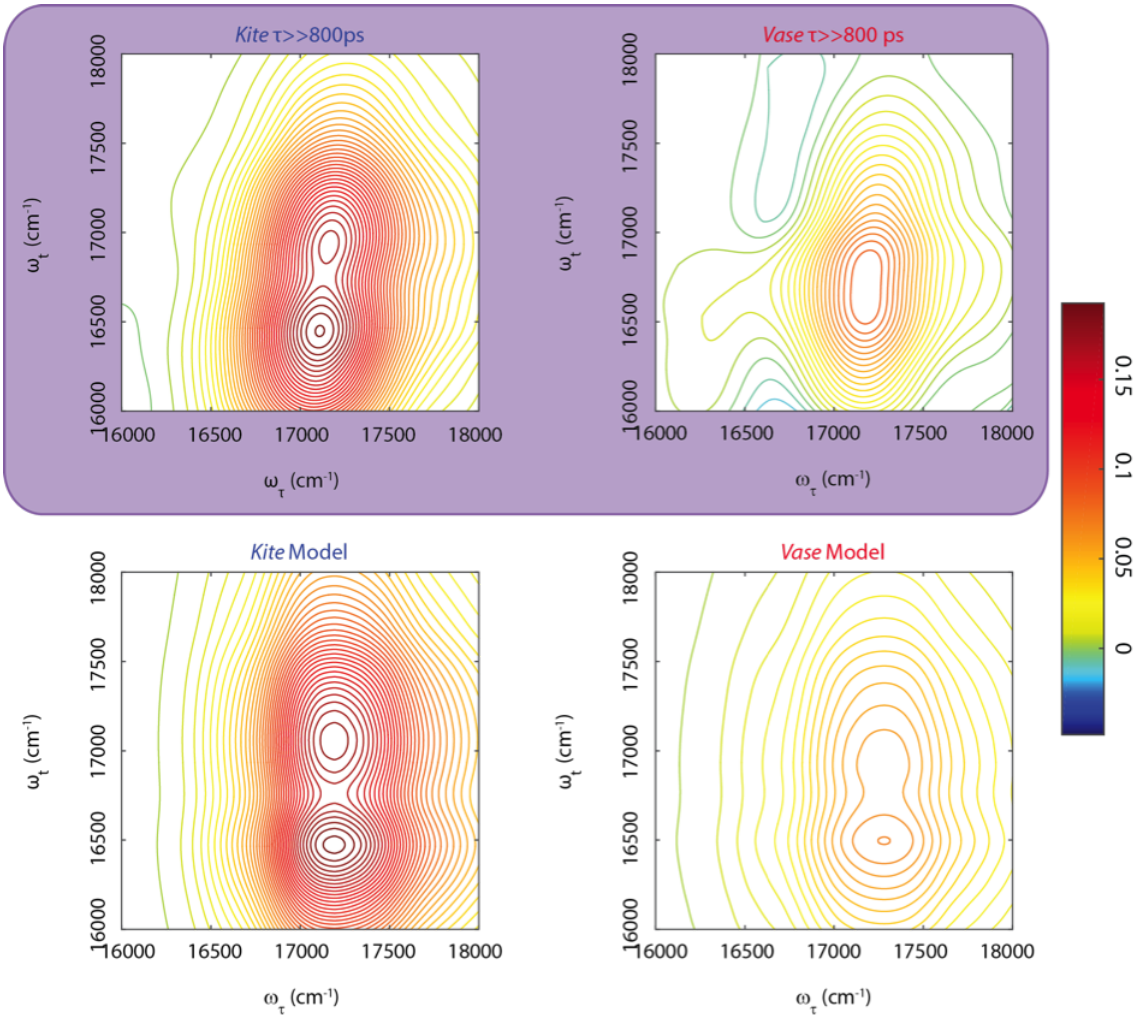

Figure 3.9: Comparison between residual fluorescence features in Figure 3.12 with simulated spectra of donor. Top row shows long time lifetime maps for both *kite* (-80°C) and *vase* (RT) configurations. Bottom row shows simulated spectra made from a convolution of the donor absorption with the sum of the donor absorption and fluorescence. Simulated spectra were also convoluted (twice in ω_{tau} and once in ω_t) with a measured laser spectrum to produce the expected 2D signal.

3.6 Conformation-Dependent Changes in Excited-State Dynamics and Effects on FRET

The excited-state dynamic processes in cavitand 1 elucidated by 2DES and DAS analyses are summarized in Figure 3.10. After absorption in the donor from ground state D_0 to initial excited state D', rapid vibrational relaxation on the excited state surface occurs within the first 100 fs, as shown in inset 1 of Figure 3.10. Excitations relax into (at least) two local minima, with one containing 20-30% of the original excited state population leading to nonradiative relaxation on a ∼25 ps timescale. All remaining excitations relax into the local minimum corresponding to dipole-driven relaxation, either as FRET or fluorescence. At this juncture, the available population of FRET donors is limited again, but by a distribution of dipole orientations between donor and acceptor. Inset 2 of Figure 3.10 shows two example chromophore orientations in the *kite* conformation, one in which FRET occurs readily (bottom) and one in which FRET is prohibited as dipole coupling approaches zero (top). This distribution of dipole orientations leads to the two remaining decays illustrated in Figure 3.6, one due to energy transfer (orange in Figure 4, dashed orange arrows in Figure 3.10), and one due to residual fluorescence (purple in Figure 3.6, dark purple arrow in Figure 3.10). With a rate of a few hundred ps, FRET is the dominant dipole-driven relaxation pathway for the donor, regardless of conformation. The acceptor then quickly relaxes out of our laser bandwidth and is not observed. While FRET remains the dominant pathway, conformational change between *vase* and *kite* affects both the transfer rate and the relative fractions of excited donor molecules decaying along all three paths.

While we identify the second of the three lifetimes as corresponding to energy transfer, it should be noted that the measured lifetime is distinct from the time actually required for transfer. FRET relies upon the same dipole coupling between ground and excited states that leads to donor fluorescence, meaning that fluorescence always occurs along with FRET and that the branching ratio between them is determined by their relative rates. As such,

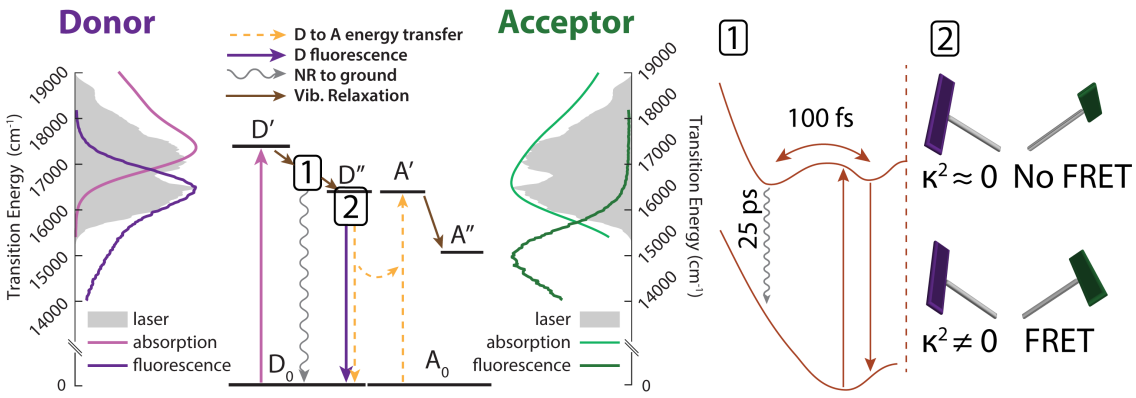

Figure 3.10: Energy diagram interpretation of the observed dynamics. Initial excitation to D′ (light purple) quickly relaxes vibrationally into one of two wells (see inset 1). Excited donors then relax back to the ground state either nonradiatively (wavy grey arrow) or via dipole coupling from well D″ (straight dark purple arrow). Part of the decay from D″ transfers energy to the acceptor via FRET (dashed orange arrows), and part decays without transfer, as shown in inset 2. Side panels show donor (purple) and acceptor (green) absorption and emission spectra (light and dark lines) overlaid with the laser spectrum (solid grey). Inset 1 shows relaxation into multiple wells in the excited state (top) leading to nonradiative relaxation (wavy grey arrow) and dipole relaxation (straight brown arrow). Inset 2 shows example dipole orientations in the kite conformation. A distribution of dipole orientations is responsible for multiple lifetimes of dipole-based donor relaxation.

the measured decay in excited state population will have a rate k_{2D} such that

$$k_{2D} = k_{tr} + k_{d,0} \tag{3.5}$$

where k_{tr} is the transfer rate, k_{2D} is the observed decay rate, and $k_{d,0}$ is the fluorescence decay rate of the unperturbed donor. [53] As before, any rate k is defined as the inverse of the respective lifetime τ. Using this approach with k_{2D} as the rate labeled "energy transfer," we estimate the FRET lifetimes to be 303 ± 10 ps for the *vase* conformation and 602 ± 58 ps for the *kite* conformation.

In addition to determining transfer lifetimes, we can calculate the branching ratio of FRET in this system using eq. 3.1, where τ_{DA} is the lifetime we assign to energy transfer in DAS and τ_D is the fluorescence decay lifetime of the donor in solution, measured via time-correlated single photon counting (TCSPC). This method results in a calculated transfer efficiency of 92.1 ± 1.3% transfer for the *vase* conformation and 78.0 ± 2.9% for the *kite*

conformation. This approach only accounts for kinetic competition, however, and therefore only determines the efficiency of the subpopulation measured in DAS. If we use the peak diagonal intensities from DAS to approximate branching between the three subpopulations, we obtain overall FRET efficiencies of 68.7 ± 1.1% for the *vase* conformation and 44.3 ± 1.8% for the *kite* conformation, a significant reduction in overall values and a dramatically greater difference between conformations than the difference measured via Eq. 3.1.

3.7 Conclusions

The results above highlight how conformation-dependent variations in nonradiative relaxation processes affect the accuracy of lifetime-based FRET measurements. These effects should be considered in situations where the chromophore structure(s) or their relative orientations result in either: 1) breakdown of the ideal dipole approximation (IDA); or 2) appreciable competition in the excited state population between FRET and nonradiative relaxation. The former is relevant to chromophore structures that exhibit delocalized transition densities [58, 59] or to systems in which chromophore orientations are restricted such that isotropic dipole distributions that might mitigate IDA breakdown cannot be achieved [60, 61]. The latter situation might arise in donor chromophore structures that exhibit either modest quantum yields or conformational freedom that exacerbates nonradiative relaxation processes [39]. In addition to considering the effect of variations in nonradiative relaxation on FRET measurements, these variations might also be exploited productively as probes for changing viscosity in cell environments via motion-induced change in emission measurements (MICE) [62].

3.8 Spectroscopic Methods

3.8.1 Fluorescence Quantum Yield

The quantum yields of the donor and acceptor are shown in table 3.2 and Figure 3.11. All spectra for the quantum yield measurement were recorded using a Horiba Fluorolog 3 with the Quanta-Phi integrating sphere attachment. Actual calculation of quantum yields was performed via the software packaged with the instrument, and the values are recorded below in Table 3.2. Scatter-corrected absorption is determined by subtracting the scatter signal at from the fluorophore solution from that of a solvent blank, measured with the same excitation source. Scatter-corrected emission is similarly determined by subtracting solvent blank signal from the fluorophore emission spectrum. The ratio of integrated fluorophore emission counts to absorption counts defines the quantum yield. In this case, acceptor emission spectra are scaled by a factor of 1/100 to account for a 100x longer integration time due to weak signal.

Quantum Yield (%)	
Donor	30.6 ± 0.8
Acceptor	4.40 ± 0.02

Table 3.2: Fluorescence quantum yield of donor and acceptor.

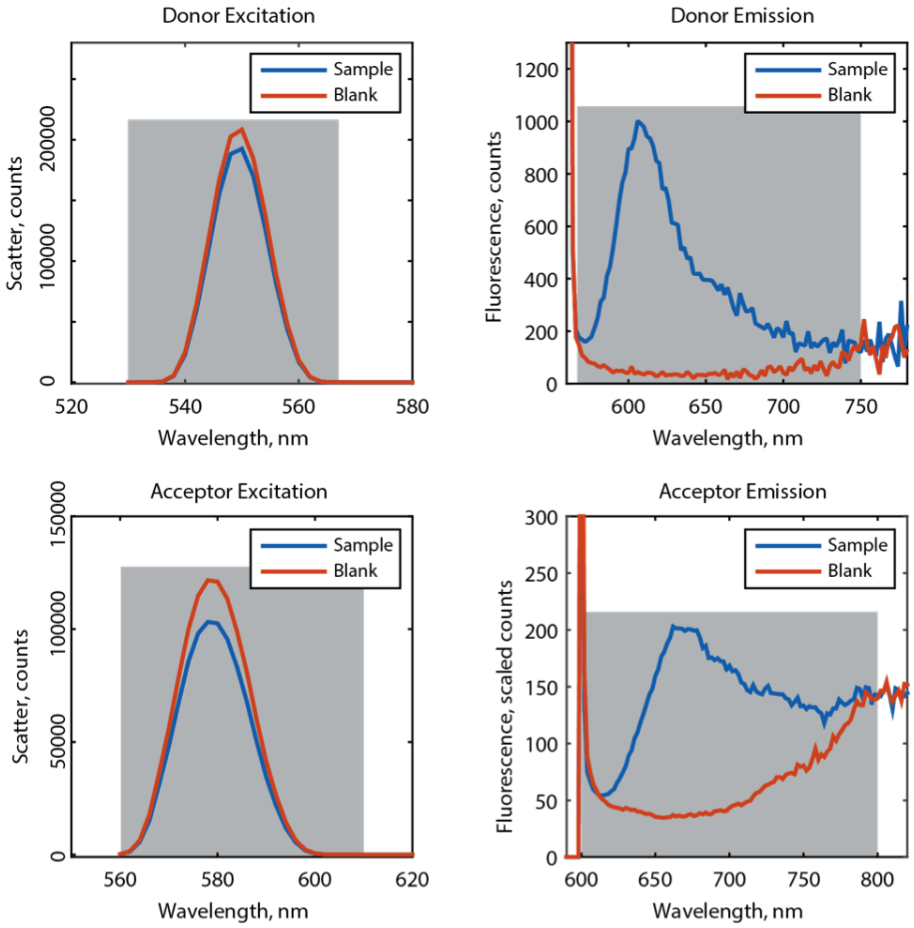

Figure 3.11: Excitation and emission spectra (with reference solvent blank) for fluorescence quantum yield calculation. Grey boxes indicate bounds of integration for quantum yield calculations.

3.8.2 Absorption spectra

UV/Vis absorption spectra of the BODIPY-cavitand dimer were recorded using a Cary 5000 dual-beam UV/VIS/NIR spectrophotometer and the steady state fluorescence spectra were measured via a Horiba Fluorolog 3. Absorption and fluorescence spectra of the *vase* conformation at 294 K and *kite* conformation at 193 K are shown in Figure 3.3a and Figure 3.3b. Comparison of the BODIPY-cavitand dimer absorption spectra (dashed red/blue lines) to that of a 1:1 mixture of donor and acceptor in solution at the two temperatures (dashed black/grey lines) highlights the change in electronic coupling that occurs with conformational switching. The *kite* spectra resembles that of the dye mixture, but the *vase* absorption blue-shifts relative to the dye mixture, indicating interactions between the donor and acceptor that shift their ground and excited state energies. Fluorescence spectra of *vase* (red solid line in Figure 3.3a) and *kite* (blue solid line in Figure 3.3b) dimers show a clear increase in donor emission and concurrent decrease in acceptor emission when the BODIPY-cavitand dimer switches from *kite* to *vase*. These fluorescence intensity changes suggest a decrease in FRET efficiency when the donor-acceptor distance increases, indicating that the BODIPY-cavitand dimer performs as designed.

3.8.3 Fluorescence Lifetimes

The fluorescence lifetimes were measured on a ChronosBH lifetime fluorometer (ISS, Inc.) using Time-Correlated Single Photon Counting (TCSPC) methods. The fluorometer contained Becker-Hickl SPC-130 detection electronics and an HPM-100-40 Hybrid PMT detector. Tunable picosecond pulsed excitation at 560nm was provided by a Fianium SC400-2 supercontinuum laser source with integrated pulse picker and AOTF. Emission wavelengths were selected with bandpass filters (Chroma HQ615/85nm). The Instrument Response Function (IRF) was measured to be approximately 120 ps FWHM in a 1% scattering solution of Ludox LS colloidal silica. Multi-component exponential decay lifetimes were fit via a forward convolution method in the Vinci control and analysis software.

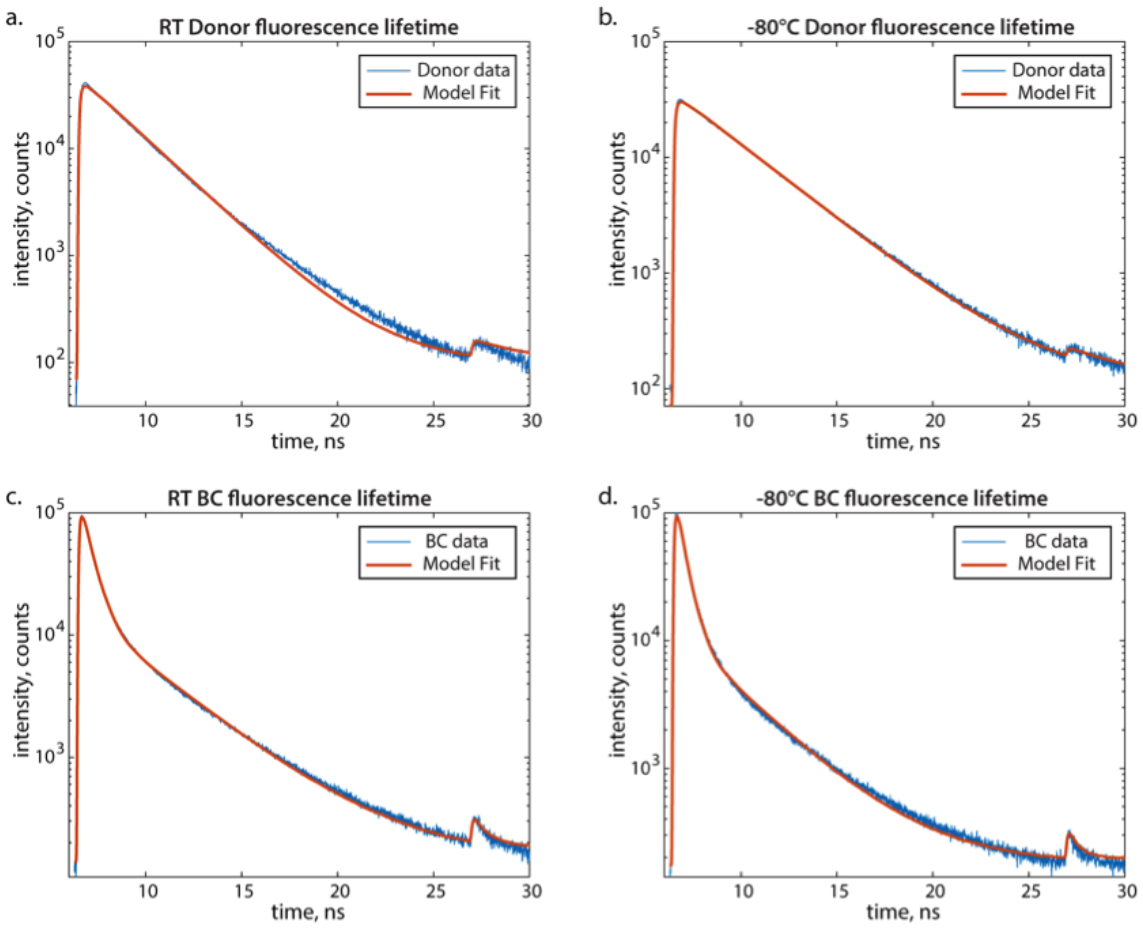

Figure 3.12: Fluorescence lifetimes measured by TCSPC. The measured data (in blue) are fitted to exponential decays convoluted with a measured instrument response function (in red) using software provided with the instrument. The jump at 27 ns is due to a small bleed through in the pulse picker used to control excitation pulse timing.

	Temperature (K)	τ_1 (ps)	A_2	E(%)
Cavitand **1** *kite*	193	411 ± 1	3090 ± 4	87.5 ± 0.1
Cavitand **1** *vase*	294	497 ± 1	3560 ± 4	78.0 ± 0.1
Donor	193	3300 ± 1	-	-
Donor	294	2600 ± 1	-	-

Table 3.3: Fluorescence lifetimes and FRET efficiencies measured by TCSPC.

3.8.4 Two-Dimensional Electronic Spectra

Two-dimensional electronic spectra of the BODIPY-cavitand dimer were acquired using a homebuilt instrument that has been described previously [45]. A Ti:Sapphire oscillator and regenerative amplifier (Micra and Legend Elite, Coherent) generate a 5kHz, 100fs pulse train that is directed into a noncollinear optical parametric amplifier (NOPA, TOPAS). The output of the NOPA is then compressed using a prism pair followed by a spatial light modulator array (FemtoJock, Biophotonics). The resulting pulse (12 fs, 530-650 nm FWHM) is then split into four via a beamsplitter and a transmissive grating. The four beams are directed to the sample with a boxcar geometry. The time delays are controlled by paired glass wedges (coherence time, τ) and a translational stage (waiting time, T). Beam 1, 2 and 3 interacts with sample to generate the third-order signal. Beam 4 is attenuated by three orders of magnitude and serves as local oscillator for heterodyne detection. Signal, along with the local oscillator, is directed to a spectrometer and the resulting interferogram is recorded on a CCD array (Andor).

3.8.5 Phasing of 2D Spectra

Phasing was performed as described in previous publications [63, 64]. From the projection slice theorem, the real part of a 2D spectrum summed along ω_τ should match a symmetric pump-probe spectrum generated from the same light at the same waiting time. To correct for phase errors in our experimental setup, we fit the 2D spectra with an added phase function to pump probe data collected on a separate instrument. Our phase error is time independent, so all waiting times have the same phase correction applied. To further ensure comparable

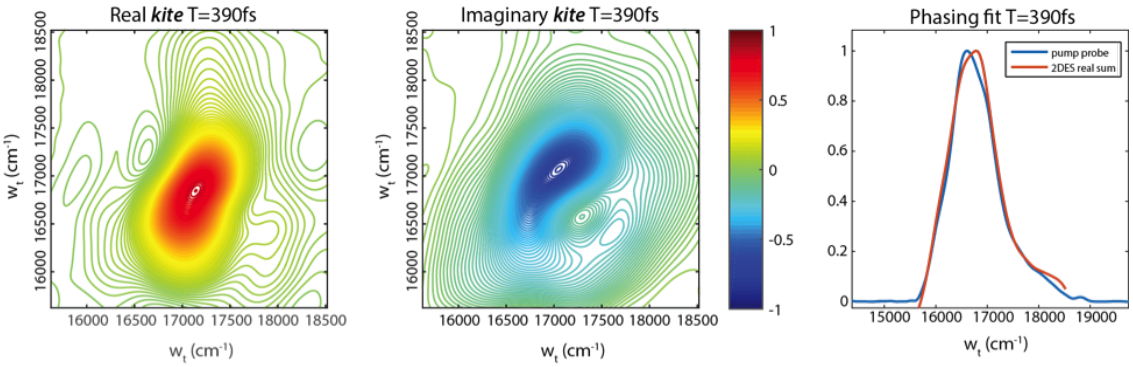

Figure 3.13: Representative phased data at T = 390 fs. The third plot shows the resulting fit of real value phased 2D data summed across ω_τ (2DES real sum, red) to the pump probe spectrum at the same waiting time (pump probe, blue).

datasets, the same phase adjustments were applied to both the -80 °C and RT datasets. The phase function applied includes a constant phase plus terms linear and quadratic in ω_t and ω_τ.

$$S_{2D}^{phased} = a_1 S_{2D} e^{i(a_2 + a_3(\omega_t - \omega_{t,0}) + a_4(\omega_t - \omega_{t,0})^2 + a_5(\omega_\tau - \omega_{\tau,0}) + a_6(\omega_\tau - \omega_{\tau,0})^2)} \tag{3.6}$$

$$S_{pump\ probe} = \int \Re[S_{2D}^{phased}] d\omega_\tau \tag{3.7}$$

Pump probe spectra were recorded with a separate instrument, as described previously [64]. Ultrafast (fs-resolved) 2DES were used for phasing to pump probe, and the same phasing correction parameters were applied to all datasets. All 2D datasets were collected on the same instrument within a 36 hour period. Representative phased data from this short time experiment, as well as fitting results from phasing, are shown below.

3.8.6 Decay-Associated 2D Spectra

To obtain the lifetime maps shown in Figure 3.4, the following approach was taken: First, lifetimes were determined using a binned dataset (10x in both frequency dimensions) with waiting times from 5 ps to 800 ps. Time traces associated with each pixel in the 2D spectra

were fit to a bi-exponential decay with an offset

$$S(T) = A_1 e^{-T/\tau_1} + A_2 e^{-T/\tau_2} + A_3 \tag{3.8}$$

Results of this fit were used to filter out points with less than 10% total signal from the first or second lifetime. The remaining signal was then least-squares fit to the same model, but with τ_1 and τ_2 constant across the dataset (to optimize those values, listed in Table 3.4). These lifetimes were then used to generate the maps shown in Figure 3.4 using an unbinned dataset. For this, each pixel in frequency space was normalized and least-squares fit to the same model with the global times. The resulting map of pre-exponentials (which summed to one in each pixel) was then weighted by the signal at $T = 5$ ps (the first nonzero waiting time) to give the plots in Figure 3.4.

	τ_1 (ps)	τ_2 (ps)
kite	24 ± 3	510 ± 40
vase	27 ± 5	271 ± 8

Table 3.4: Lifetimes used to generate lifetime maps.

Confidence bounds for the pre-exponentials are shown in Figure 3.14. To generate the maps shown in Figure 3.14, we scaled one side of the 95% confidence bound for the given parameter by the intensity of the starting value (same scaling as in Figure 3.4 in main text).

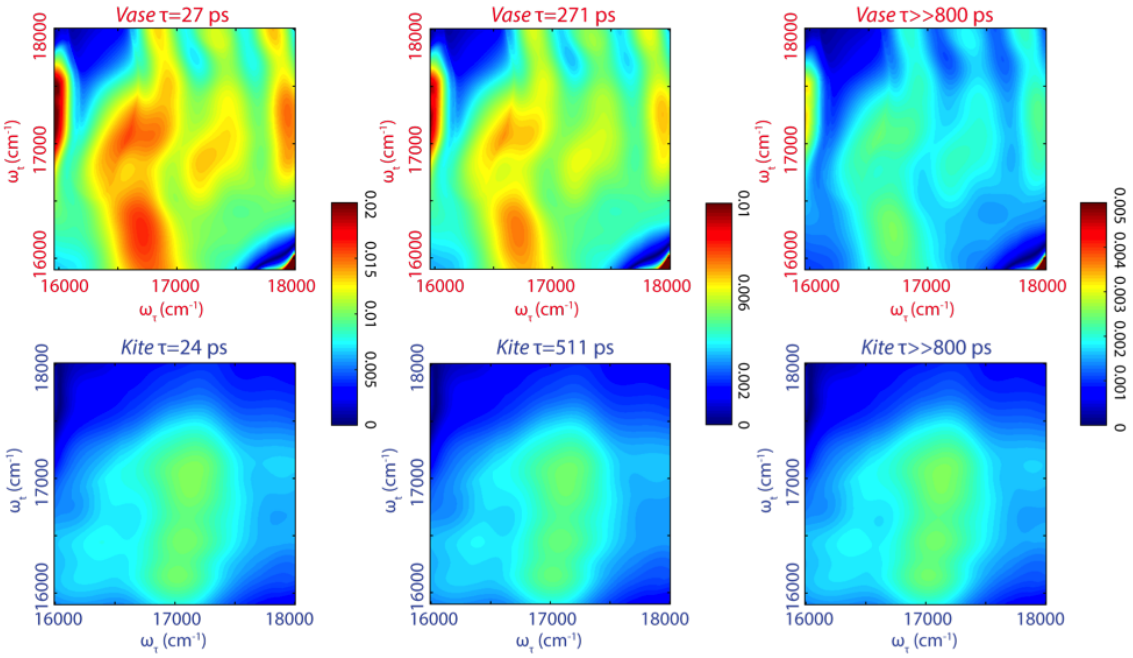

Figure 3.14: Absolute value of 95% confidence bounds for fitting maps presented in Figure 3.6. Generated by multiplying one side of the symmetrical 95% confidence range of the relevant fit parameter (absolute value) with the starting real value signal as is done in Figure 3.6.

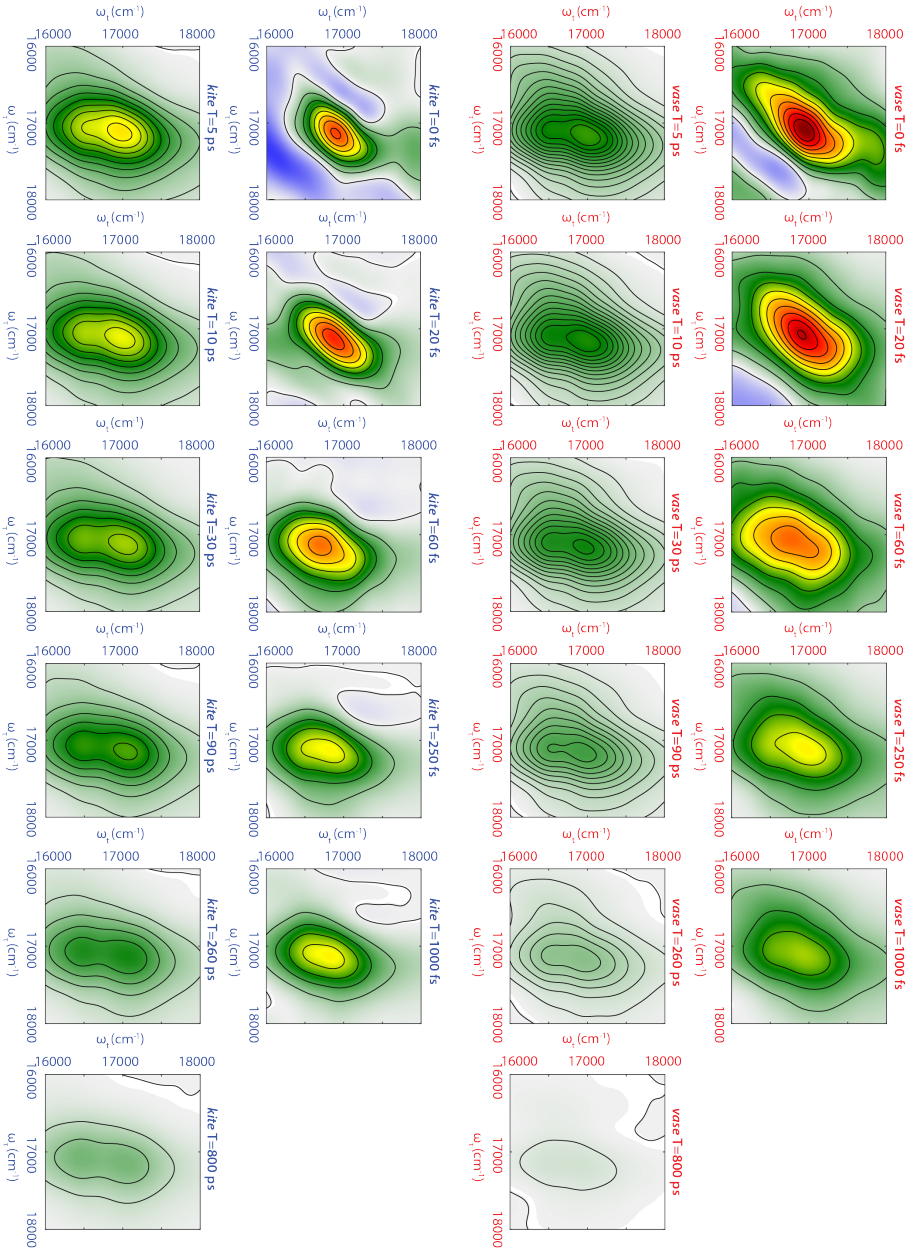

Figure 3.15: 2D spectral data shown in stacked form in Figure 3.4 part c.

REFERENCES

[1] T. Förster. Energiewanderung und Fluoreszenz. *Naturwissenschaften*, 33:166–175, 1946.

[2] T. Förster. *Istanbul Lectures, Part III: Action of Light and Organic Crystals*. Academic Press, New York, 1965.

[3] Robert M. Clegg. Fluorescence resonance energy transfer. *Current Opinion in Biotechnology*, 6(1):103–110, 1995.

[4] Paul R. Selvin. The renaissance of fluorescence resonance energy transfer. *Nat Struct Mol Biol*, 7(9):730–734, 2000.

[5] P. G. Wu and L. Brand. Resonance energy transfer: Methods and applications. *Analytical Biochemistry*, 218(1):1–13, 1994.

[6] L. Stryer and R. P. Haugland. Energy transfer: a spectroscopic ruler. *Proceedings of the National Academy of Sciences*, 58(2):719–726, 1967.

[7] Cristobal G. dos Remedios and Pierre D. J. Moens. Fluorescence resonance energy transfer spectroscopy is a reliable "ruler" for measuring structural changes in proteins. *Journal of Structural Biology*, 115(2):175–185, 1995.

[8] Richard N. Day, Ammasi Periasamy, and Fred Schaufele. Fluorescence resonance energy transfer microscopy of localized protein interactions in the living cell nucleus. *Methods*, 25(1):4–18, 2001.

[9] Ben N. G. Giepmans, Stephen R. Adams, Mark H. Ellisman, and Roger Y. Tsien. The fluorescent toolbox for assessing protein location and function. *Science*, 312(5771):217, 2006.

[10] Marc Tramier, Isabelle Gautier, Tristan Piolot, Sylvie Ravalet, Klaus Kemnitz, Jacques Coppey, Christiane Durieux, Vincent Mignotte, and Maïté Coppey-Moisan. Picosecond-

hetero-FRET microscopy to probe protein-protein interactions in live cells. *Biophysical Journal*, 83(6):3570–3577, 2002.

[11] Steven S. Vogel, Christopher Thaler, and Srinagesh V. Koushik. Fanciful FRET. *Science's STKE*, 2006(331):re2, 2006.

[12] Vladimir V Didenko. DNA probes using fluorescence resonance energy transfer (FRET): Designs and applications. *BioTechniques*, 31(5):1106–1121, 11 2001.

[13] Chun-Yang Zhang, Hsin-Chih Yeh, Marcos T. Kuroki, and Tza-Huei Wang. Single-quantum-dot-based dna nanosensor. *Nature Materials*, 4(11):826–831, 2005.

[14] Sohila Zadran, Steve Standley, Kaylee Wong, Erick Otiniano, Arash Amighi, and Michel Baudry. Fluorescence resonance energy transfer (FRET)-based biosensors: visualizing cellular dynamics and bioenergetics. *Applied Microbiology and Biotechnology*, 96(4):895–902, 2012.

[15] A. Hillisch, M. Lorenz, and S. Diekmann. Recent advances in FRET: distance determination in protein-DNA complexes. *Current Opinion in Structural Biology*, 11(2):201–207, 2001.

[16] Philippe I. H. Bastiaens and Anthony Squire. Fluorescence lifetime imaging microscopy: spatial resolution of biochemical processes in the cell. *Trends in Cell Biology*, 9(2):48–52, 1999.

[17] Rajesh Babu Sekar and Ammasi Periasamy. Fluorescence resonance energy transfer (FRET) microscopy imaging of live cell protein localizations. *The Journal of Cell Biology*, 160(5):629, 2003.

[18] Kevin Truong and Mitsuhiko Ikura. The use of FRET imaging microscopy to detect protein–protein interactions and protein conformational changes *in vivo*. *Current Opinion in Structural Biology*, 11(5):573–578, 2001.

[19] Horst Wallrabe and Ammasi Periasamy. Imaging protein molecules using FRET and FLIM microscopy. *Current Opinion in Biotechnology*, 16(1):19–27, 2005.

[20] W. Becker. Fluorescence lifetime imaging: techniques and applications. *Journal of Microscopy*, 247(2):119–136, 2012.

[21] Elizabeth A. Jares-Erijman and Thomas M. Jovin. FRET imaging. *Nature Biotechnology*, 21(11):1387–1395, 2003.

[22] Elizabeth A. Jares-Erijman and Thomas M. Jovin. Imaging molecular interactions in living cells by FRET microscopy. *Current Opinion in Chemical Biology*, 10(5):409–416, 2006.

[23] David W. Piston and Gert-Jan Kremers. Fluorescent protein FRET: the good, the bad and the ugly. *Trends in Biochemical Sciences*, 32(9):407–414, 2007.

[24] A. Paul Alivisatos, Weiwei Gu, and Carolyn Larabell. Quantum dots as cellular probes. *Annual Review of Biomedical Engineering*, 7(1):55–76, 2005.

[25] Xiaoqin Chi, Dengtong Huang, Zhenghuan Zhao, Zijian Zhou, Zhenyu Yin, and Jinhao Gao. Nanoprobes for *in vitro* diagnostics of cancer and infectious diseases. *Biomaterials*, 33(1):189–206, 2012.

[26] Aaron R. Clapp, Igor L. Medintz, and Hedi Mattoussi. Förster resonance energy transfer investigations using quantum-dot fluorophores. *ChemPhysChem*, 7(1):47–57, 2006.

[27] Philip D. Howes, Rona Chandrawati, and Molly M. Stevens. Colloidal nanoparticles as advanced biological sensors. *Science*, 346(6205), 2014.

[28] Kim E. Sapsford, Lorenzo Berti, and Igor L. Medintz. Materials for fluorescence resonance energy transfer analysis: Beyond traditional donor–acceptor combinations. *Angewandte Chemie International Edition*, 45(28):4562–4589, 2006.

[29] Lin Yuan, Weiying Lin, Kaibo Zheng, and Sasa Zhu. FRET-based small-molecule fluorescent probes: Rational design and bioimaging applications. *Accounts of Chemical Research*, 46(7):1462–1473, 2013.

[30] Claude Berney and Gaudenz Danuser. FRET or No FRET: A quantitative comparison. *Biophysical Journal*, 84(6):3992–4010, 2003.

[31] Ulai Noomnarm and Robert M. Clegg. Fluorescence lifetimes: fundamentals and interpretations. *Photosynthesis Research*, 101(2):181–194, 2009.

[32] V. A. Azov, A. Schlegel, and F. Diederich. Geometrically precisely defined multinanometer expansion/contraction motions in a resorcin[4]arene cavitand based molecular switch. *Angewandte Chemie International Edition*, 44(29):4635–4638, 2005.

[33] V. A. Azov, A. Beeby, M. Cacciarini, A. G. Cheetham, F. Diederich, M. Frie, J. K. Gimzewski, V. Gramlich, B. Hecht, B. Jaun, T. Latychevskaia, A. Lieb, Y. Lill, F. Marotti, A. Schlegel, R. R. Schlittler, P. J. Skinner, P. Seiler, and Y. Yamakoshi. Resorcin[4]arene cavitand-based molecular switches. *Advanced Functional Materials*, 16:147–156, 2006.

[34] J. R. Moran, S. Karbach, and D. J. Cram. Cavitands: Synthetic molecular vessels. *Journal of the American Chemical Society*, 104:5826–5828, 1982.

[35] Igor Pochorovski, Benjamin Breiten, W. Bernd Schweizer, and François Diederich. FRET studies on a series of BODIPY-dye-labeled switchable resorcin[4]arene cavitands. *Chemistry –A European Journal*, 16(42):12590–12602, 2010.

[36] Igor Pochorovski and François Diederich. Fluorophore-functionalized and top-covered resorcin[4]arene cavitands. *Israel Journal of Chemistry*, 52(1-2):20–29, 2012.

[37] Igor Pochorovski, Tim Knehans, Daniel Nettels, Astrid M. Müller, W. Bernd Schweizer, Amedeo Caflisch, Benjamin Schuler, and François Diederich. Experimental and com-

putational study of BODIPY dye-labeled cavitand dynamics. *Journal of the American Chemical Society*, 136(6):2441–2449, 2014.

[38] Feirong Li, Sung Ik Yang, Yangzhen Ciringh, Jyoti Seth, Charles H. Martin, Deepak L. Singh, Dongho Kim, Robert R. Birge, David F. Bocian, Dewey Holten, and Jonathan S. Lindsey. Design, synthesis, and photodynamics of light-harvesting arrays comprised of a porphyrin and one, two, or eight boron-dipyrrin accessory pigments. *Journal of the American Chemical Society*, 120(39):10001–10017, 1998.

[39] Hooi Ling Kee, Christine Kirmaier, Lianhe Yu, Patchanita Thamyongkit, W. Justin Youngblood, Matthew E. Calder, Lavoisier Ramos, Bruce C. Noll, David F. Bocian, W. Robert Scheidt, Robert R. Birge, Jonathan S. Lindsey, and Dewey Holten. Structural control of the photodynamics of borondipyrrin complexes. *The Journal of Physical Chemistry B*, 109(43):20433–20443, 2005.

[40] L. Wang, I. S. Tamgho, L. A. Crandall, J. J. Rack, and C. J. Ziegler. Ultrafast dynamics of a new class of highly fluorescent boron difluoride dyes. *Physical Chemistry Chemical Physics*, 17(4):2349–2351, 2015.

[41] Y. Wang, D. Zhang, H. Zhou, J. Ding, Q. Chen, Y. Xiao, and S. Qian. Nonlinear optical properties and ultrafast dynamics of three novel boradiazaindacene derivatives. *Journal of Applied Physics*, 108(3):033520, 2010.

[42] Gabriela S. Schlau-Cohen, Akihito Ishizaki, and Graham R. Fleming. Two-dimensional electronic spectroscopy and photosynthesis: Fundamentals and applications to photosynthetic light-harvesting. *Chemical Physics*, 386(1–3):1–22, 2011.

[43] Peter D. Dahlberg, Andrew F. Fidler, Justin R. Caram, Phillip D. Long, and Gregory S. Engel. Energy transfer observed in live cells using two-dimensional electronic spectroscopy. *The Journal of Physical Chemistry Letters*, 4(21):3636–3640, 2013.

[44] Elisabetta Collini, Cathy Y. Wong, Krystyna E. Wilk, Paul M. G. Curmi, Paul Brumer, and Gregory D. Scholes. Coherently wired light-harvesting in photosynthetic marine algae at ambient temperature. *Nature*, 463(7281):644–647, 2010.

[45] Dugan Hayes, Graham B. Griffin, and Gregory S. Engel. Engineering coherence among excited states in synthetic heterodimer systems. *Science*, 340(6139):1431, 2013.

[46] Artem A. Bakulin, Sarah E. Morgan, Tom B. Kehoe, Mark W. B. Wilson, Alex W. Chin, Donatas Zigmantas, Dassia Egorova, and Akshay Rao. Real-time observation of multiexcitonic states in ultrafast singlet fission using coherent 2D electronic spectroscopy. *Nature Chemistry*, 8(1):16–23, 2016.

[47] Chanelle C. Jumper, Jessica M. Anna, Anna Stradomska, Juleon Schins, Mykhaylo Myahkostupov, Valentina Prusakova, Daniel G. Oblinsky, Felix N. Castellano, Jasper Knoester, and Gregory D. Scholes. Intramolecular radiationless transitions dominate exciton relaxation dynamics. *Chemical Physics Letters*, 599:23–33, 2014.

[48] Vladimir A. Azov, Bernhard Jaun, and François Diederich. NMR investigations into the vase-kite conformational switching of resorcin[4]arene cavitands. *Helvetica Chimica Acta*, 87(2):449–462, 2004.

[49] J.-B. Wang, Q.-Q. Wu, Y.-Z. Min, Y.-Z. Liu, and Q.-H. Song. A novel fluorescent probe for Au(III)/Au(I) ions based on an intramolecular hydroamination of a BODIPY derivative and its application to bioimaging. *Chemical Communications*, 48(744-746), 2012.

[50] Michael J. Frisch, G. W. Trucks, H. Bernhard Schlegel, Gustavo E. Scuseria, Michael A. Robb, James R. Cheeseman, Giovanni Scalmani, Vincenzo Barone, Benedetta Mennucci, G. A. Petersson, H. Nakatsuji, M. Caricato, Xiaosong Li, H. P. Hratchian, Artur F. Izmaylov, Julien Bloino, G. Zheng, J. L. Sonnenberg, M. Hada, M. Ehara, K. Toyota, R. Fukuda, J. Hasegawa, M. Ishida, T. Nakajima, Y. Honda, O. Kitao,

H. Nakai, T. Vreven, J. A. Montgomery Jr., J. E. Peralta, François Ogliaro, Michael J. Bearpark, Jochen Heyd, E. N. Brothers, K. N. Kudin, V. N. Staroverov, Rika Kobayashi, J. Normand, Krishnan Raghavachari, Alistair P. Rendell, J. C. Burant, S. S. Iyengar, Jacopo Tomasi, M. Cossi, N. Rega, N. J. Millam, M. Klene, J. E. Knox, J. B. Cross, V. Bakken, C. Adamo, J. Jaramillo, R. Gomperts, R. E. Stratmann, O. Yazyev, A. J. Austin, R. Cammi, C. Pomelli, J. W. Ochterski, R. L. Martin, K. Morokuma, V. G. Zakrzewski, G. A. Voth, P. Salvador, J. J. Dannenberg, S. Dapprich, A. D. Daniels, Ödön Farkas, J. B. Foresman, J. V. Ortiz, J. Cioslowski, and Douglas J. Fox. Gaussian 09, 2009.

[51] Minhaeng Cho. Coherent two-dimensional optical spectroscopy. *Chemical Reviews*, 108(4):1331–1418, 2008.

[52] Igor Stiopkin, Tobias Brixner, Mino Yang, and Graham R. Fleming. Heterogeneous exciton dynamics revealed by two-dimensional optical spectroscopy. *The Journal of Physical Chemistry B*, 110(40):20032–20037, 2006.

[53] Abraham Nitzan. *Chemical Dynamics in Condensed Phases: Relaxation, Transfer and Reactions in Condensed Molecular Systems*. Oxford University Press, New York, 2006.

[54] P. Hamm and M. T. Zanni. *Concepts and methods of 2D infrared spectroscopy*. Cambridge University Press, New York, 2011.

[55] C. Wang, Moira L. Flanagan, Ryan D. McGillicuddy, H. Zheng, Alan R. Ginzburg, X. Yang, K. Moffat, and Gregory S. Engel. Bacteriophytochrome photoisomerization proceeds homogeneously despite heterogeneity in ground state. *Biophysical Journal*, 111(10):2125–2134, 2016.

[56] Evgeny E. Ostroumov, Rachel M. Mulvaney, Richard J. Cogdell, and Gregory D. Scholes. Broadband 2d electronic spectroscopy reveals a carotenoid dark state in purple bacteria. *Science*, 340(6128):52–56, 2013.

[57] Jakub Dostál, Barbora Benešová, and Tobias Brixner. Two-dimensional electronic spectroscopy can fully characterize the population transfer in molecular systems. *The Journal of Chemical Physics*, 145(12):124312, 2016.

[58] Y. R. Khan, T. E. Dykstra, and G. D. Scholes. Exploring the Förster limit in a small FRET pair. *Chemical Physics Letters*, 461(4-6):305–309, 2008.

[59] H. Sahoo, D. Roccatano, M. Zacharias, and W. M. Nau. Distance distributions of short polypeptides recovered by fluorescence resonance energy transfer in the 10 Å domain. *Journal of the American Chemical Society*, 128(25):8118–8119, 2006.

[60] A. Muñoz-Losa, C. Curutchet, B. P. Krueger, L. R. Hartsell, and B. Mennucci. Fretting about FRET: Failure of the ideal dipole approximation. *Biophysical Journal*, 96(12):4779–4788, 2009.

[61] J. D. Spiegel, S. Fulle, M. Kleinschmidt, H. Gohlke, and C. M. Marian. Failure of the IDA in FRET systems at close inter-dye distances is moderated by frequent low κ^2 values. *The Journal of Physical Chemistry B*, 120(34):8845–8862, 2016.

[62] D. Su, C. L. Teoh, L. Wang, X. Liu, and Y. T. Chang. Motion-induced change in emission (MICE) for developing fluorescent probes. *Chemical Society Reviews*, 46(16):4833–4844, 2017.

[63] Moira L. Flanagan, Phillip D. Long, Peter D. Dahlberg, Brian S. Rolczynski, Sara C. Massey, and Gregory S. Engel. Mutations to *r. sphaeroides* reaction center perturb energy levels and vibronic coupling but not observed energy transfer rates. *The Journal of Physical Chemistry A*, 120(9):1479–1487, 2016.

[64] Justin R. Caram, Haibin Zheng, Peter D. Dahlberg, Brian S. Rolczynski, Graham B. Griffin, Dmitriy S. Dolzhnikov, Dmitri V. Talapin, and Gregory S. Engel. Exploring size and state dynamics in CdSe quantum dots using two-dimensional electronic spectroscopy. *The Journal of Chemical Physics*, 140(8):084701, 2014.

CHAPTER 4

VIBRONIC COUPLING IN AN H-TYPE INDODICARBOCYANINE DIMER ON DNA

4.1 Coupling and Energy Transfer in Scaffold-Dye Structures

4.1.1 Beyond Förster theory for DNA-based cyanine dimers

Recent work in DNA nanotechnology has demonstrated the capability for creating complex 3D structures out of the biopolymer [1], and novel approaches to replication have shown promise for large scalablity of these structures [2]. Combined with the high degree of local control on molecular environments that DNA provides, these nanostructures provide a path to manmade light harvesting complexes as a test-bed for designs mimicing the protein-pigment complexes ubiquitous in photosynthesis. Significant previous work has shown success using DNA scaffolds to create controllable FRET pathways in multiple geometries [3] but a recent study [4] has shown that interactions between dyes attached at single digit base pair separations can no longer be adequately described via the point dipole approximation (which forms the basis of FRET theory). This breakdown is likely due to vibronic interactions, which are particularly strong in H-type dimers and aggregates [5], as I will later show is the case here. Understanding this breakdown in detail will lead to optimization of vibronic interactions for more effective light harvesting and faster, more efficient energy transfer throughout these nanostructured systems.

4.1.2 Vibronic coupling plays an important role in photosynthetic light harvesting

The role of vibronic coupling between chromophores in ultrafast electronic energy transfer is one that has drawn significant attention [6], particularly in reference to oscillatory dynamics in two dimensional electronic spectroscopy [7]. These oscillations have been observed in

various forms of photosynthetic bacteria [8, 9], including *in vivo* [10, 11] as well as higher organisms such as algae [12]. Oscillatory dynamics in 2D spectroscopy and their relevance to photosynthetic energy transfer have been given assignments ranging from purely electronic coherence between excitons [8] to purely vibrational motion [13], although the consensus appears to be that vibrational and electronic contributions are both important [14]. Regardless of assignment, oscillatory dynamics continue to be a hotly debated [15, 16] point of study in photosynthetic light harvesting, and may represent a part of future light harvesting designs informed by biology [17].

4.1.3 Previous synthetic approaches to vibronic and excitonic coherence

Previous approaches to creating coherence in synthetic systems undertaken by the Engel group and others have revealed some of the design principles required. Hayes et al. showed in 2013 the importance of relative rigid linkers that hold chromophores in fixed relative positions [18]. Halpin et al. showed that oscillations in an indocarbocyanine homodimer cannot be described as purely electronic or vibrational, and are instead vibronic [19]. Later, Wang et al. showed that oscillatory interactions are strongly amplified by the presence of a vibrational mode resonant with electronic transitions, and that the requisite rigidity could be achieved through the use of an external scaffold, in this case through Van der Waals interactions with a single-walled carbon nanotube [20]. Others have recently shown that signatures of coherent interactions can be seen in dyes coupled through DNA, either through forcing dye interactions through covalent attachments to the DNA polymer [21] or through induced aggregation within the dsDNA helix groove [22].

4.1.4 2D Spectroscopy as a tool for exploring coherent interactions

Two-dimensional spectroscopy has emerged as a powerful tool for investigating coupling and energy transfer in strongly interacting chromophore systems, due to its ability to separate features in both excitation and detection axes and its short time resolution. It is widely

regarded as the preferred tool for investigating electronic and vibrational coherences [23], and provides information on chromophore inhomogeneity through spectral lineshapes [24]. Through analysis of beating patterns and decay dynamics, 2D spectroscopy has enabled the discovery of various light harvesting design principles, particularly regarding coherent interactions [20].

4.2 Experimental Methods

2D spectra were recorded using the GRadient Assisted Photon Echo Spectroscopy (GRAPES) instrument, which has been described previously [25, 26, 27]. Briefly, the output of a 5 kHz ultrafast regenerative amplifier ((Legend Elite USP, Coherent) centered at 800 nm was focused through a 2.25 m tube of argon gas held at 17 psi. The broadened light was compressed via a pair of negative GVD mirrors (Layertec) and refocused through the argon tube, and the resulting white light was compressed using another pair of negative GVD mirrors and a pulse shaper using a multiphoton intrapulse interference phase scan (MIIPS) algorithm [28] (MIIPS Box 640, Biophotonics Solutions). The resulting spectrum spanned 580-720 nm and had a pulse duration of about 10 fs FWHM.

The compressed pulse was divided in two, with half the light sent to a retroreflecting delay line (Aerotech) to control the waiting time. Each beam was then sent to a wedged beamsplitter configuration consisting of a 40% reflective beamsplitter (Chroma) and a silver mirror angled at roughly 1.5 degrees, replacing the wedged glass beamsplitters used in previous iterations of the GRAPES instrument. The wedged beamsplitters create a set of four beams in a modified boxcar geometry, which are overlapped vertically using flat mirrors and focused to a line with a cylindrical mirror, creating a gradient of coherence time at the sample ranging several hundred femtoseconds.

The resulting signal from the 2DES experiment copropagates with beam 4, and both are focused through an imaging spectrometer onto a 2D CMOS array (Andor Neo) collecting frames at 20 Hz and streaming to a solid-state hard drive via Labview control software using

a producer/consumer design. The wavelength-resolved axis on the camera (from the spectrometer) contains heterodyne information on the rephasing time, which can be recovered by interpolating the signal to be linear in frequency and then using a Fourier transform to generate rephasing time. The vertical axis of the camera is resolved in coherence time from the geometric tilt of beam 1, but the data must be restructured as in [25] to create the 2D spectrum. The use of a chopper wheel and windowing functions as described previously [10] removes the majority of unwanted scatter contributions, leaving only the signal generated by the sample. Briefly, the chopper wheel blocks beams 1 and 2 for every other image the camera records, providing a measurement of scatter from beams 3 and 4 that is then subtracted. Scatter corresponding to beams 1 and 2 produces a heterodyne signal with beam 4 that oscillates at the optical frequency in waiting time. Subsampling this oscillation allows for removal of this unwanted signal via a Fourier window. Phase information is recovered by fitting to pump-probe spectra using the projection-slice theorem as previously described [29, 30].

DNA oligomers were purchased from Integrated DNA Technologies. Single strands were combined by thermal cycling to 90 °C on a hot plate. All samples are held in a 1x TAE buffer in water.

4.3 Short-distance cyanine homodimers on DNA

The DNA-dye constructs studied in this chapter are described in Figure 4.1. The monomer consists of a single indodicarbocyanine (Cy5) dye doubly attached to the phosphate backbone of an 18 base pair double-stranded DNA segment. Dimers are attached in the same fashion, with the zero base pair separated dimer (labeled "0 bp") having dyes placed on directly opposing sites in the DNA backbone, and the one base pair separated dimer (labeled "1 bp") having dye positions offset by one base pair position.

Absorption spectra for the monomer and two dimers are shown in Figure 4.2. Monomer and 1 bp dimer spectra are fit to a pair of Gaussian functions each, with center values shown

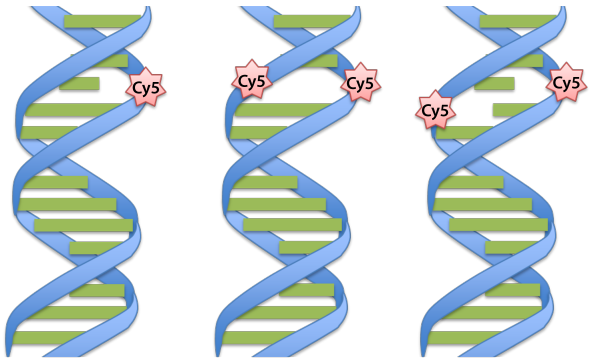

Monomer	5′-CTCGTCATTGCTAGACCAGCTTG 3′-GAGCAGTAACG*TCTGGTCGAAC
0 bp	5'-CTCGTCATTGC*AGACCAGCTTG 3'-GAGCAGTAACG*TCTGGTCGAAC
1 bp	5′-CTCGTCATTGC*AGACCAGCTTG 3′-GAGCAGTAACGA*CTGGTCGAAC

Figure 4.1: DNA-templated dimers described in this work. The above schematic shows approximate relative locations of dyes in the monomer, 0 base pair separated dimer, and 1 base pair separated dimer. Bottom of figure shows sequences used.

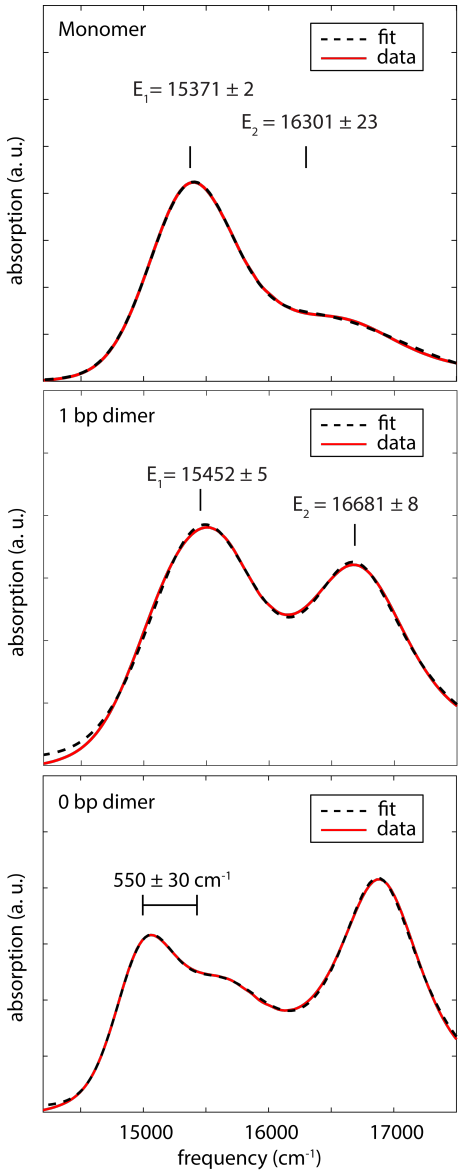

Figure 4.2: Fitted absorption spectra for cyanines on DNA. Monomer and 1 bp dimer were fit to two Gaussian features with centers shown. 0 bp dimer was fit to two Gaussians near 15000 cm^{-1} and 15500 cm^{-1}, and a Lorentzian near 16800 cm^{-1}, with the energy gap between the two gaussian features shown.

.

in the figure. The broad Gaussian features may be indicative of inhomogeneous broadening, although this is more clearly determined via 2D spectra. For the 0 bp dimer, the fit includes two Gaussian features on the red side of the spectrum near 15000 cm^{-1} and one Lorentzian feature near 17000 cm^{-1}. The Lorentzian lineshape for the higher-energy peak is supported by a fast 55 fs decay for that peak in the 2D spectrum (data not shown). The two Gaussian features are separated by 550 cm^{-1}, which 2D spectra will show corresponds to a vibrational mode that couples to the electronic transition.

4.4 Two-dimensional Spectra of DNA-dye structures

Two-dimensional electronic spectra at waiting times of T= 0 fs and T= 250 fs for all three samples are shown in Figure 4.3. The top two plots show spectra from the zero base pair separated dimer, while the middle two show spectra from the one base pair separated dimer and the bottom two show spectra from the monomer control. The left column shows spectra at a waiting time of 0 fs, where all three samples show signs of structure around the peak at approximately 15000 cm^{-1}. While all three samples show some amount of negative signal, corresponding to photoinduced (excited state) absorption, this signal vanishes in the spectra shown at 250 fs (right column) except in the case of the zero base pair separated dimer in the top right. In the diagonal feature near 15000 cm^{-1}, the two dimer samples show elongation along the diagonal that is not present in the monomer, suggestive of inhomogeneous broadening as discussed further in Figure 4.4. Additionally, both dimers show increased cross-peak strength both above and below the diagonal for the features at approximately 15000 cm^{-1} and 16700 cm^{-1}. These may be indicative of the increased vibronic coupling present in H-type dimers and aggregates [5].

The shape of spectral features in two-dimensional spectra informs on the interaction between chromophores and their surroundings. In particular, the frequency-frequency correlation function,

$$C(\tau) = \langle \delta\omega(\tau)\delta\omega(0) \rangle \tag{4.1}$$

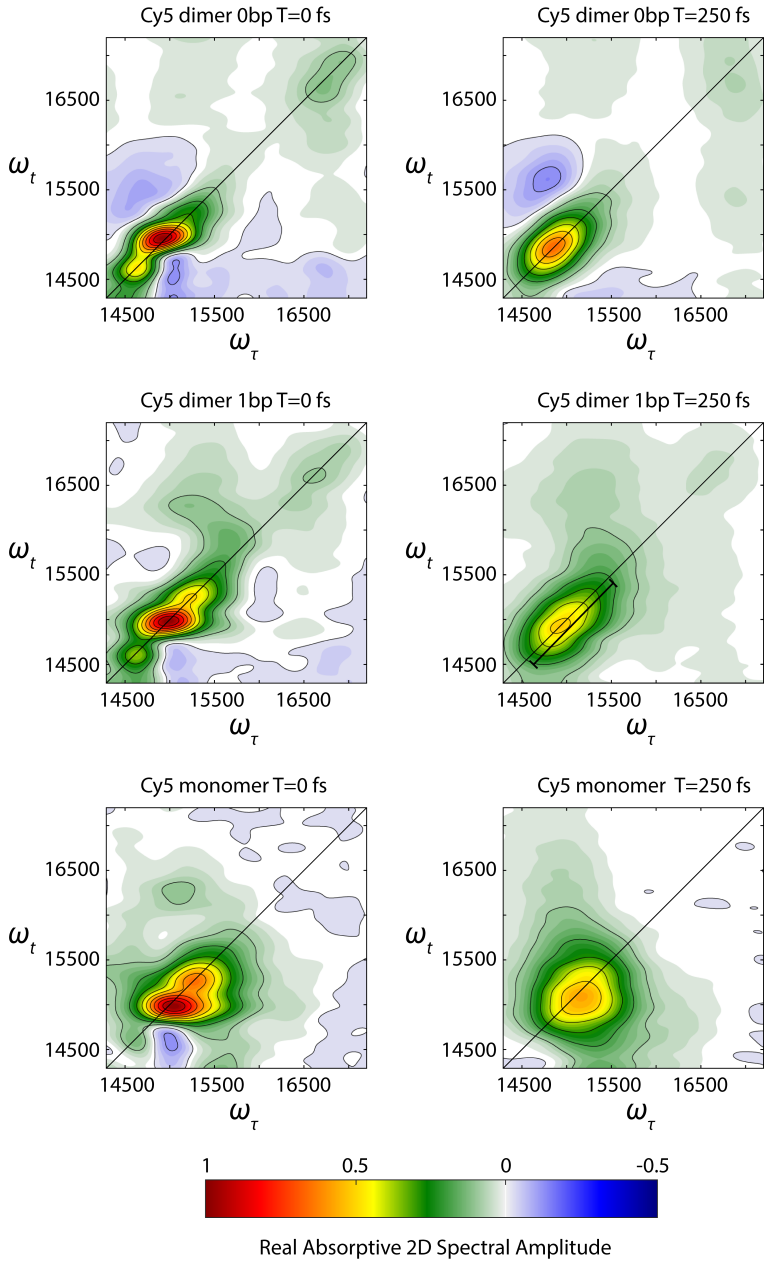

Figure 4.3: Two-dimensional spectra of Cy5-DNA species. Spectra for each sample are normalized to the maximum of the real-valued absorptive data for that sample.

which describes how frequencies fluctuate across time, can be used to describe the spectral diffusion of a given system. This correlation can be extracted from 2D spectral lineshapes via the ellipticity, $\frac{a^2-b^2}{a^2+b^2}$, where a and b correspond to the diagonal and antidiagonal linewidths respectively [24]. Figure 4.4 shows the calculation of ellipticity for the lowest-energy feature in all three DNA-dye samples. The 2D spectra on the right show the location where linewidths (as full width at half maximum) are measured, while the plots on the right show the evolution of those widths and the calculated ellipticity across waiting time. While there is significant oscillation due to vibrational interactions, the monomer ellipticity clearly decays to near zero over the first few hundred femtoseconds, showing a loss of frequency correlation across time. By contrast, both of the dimers show long lived frequency correlations that suggest inhomogeneity in the sample population, with some chromophores at higher energies than others throughout the timescale of this experiment.

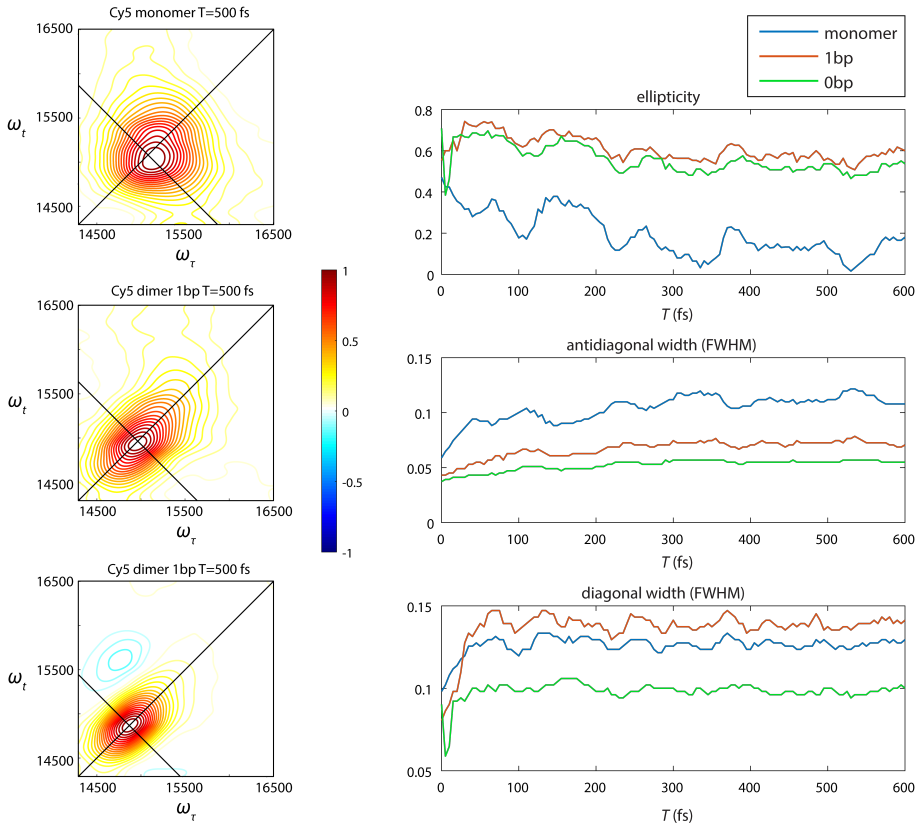

Figure 4.4: Lineshape analysis of two-dimensional spectra. 2D spectra shown are real-valued absorptive spectra at $T = 500$ fs, with lines showing position of diagonal and antidiagonal traces. Traces were recorded at each waiting time in 5 fs steps from 0 to 600, with FWHM widths plotted as shown. Ellipticity is calculated as $(a^2 - b^2)/(a^2 + b^2)$, where a and b correspond to diagonal and antidiagonal widths respectively, and corresponds to the frequency-frequency correlation function as reported in [24].

4.5 Evidence of vibronic interactions

4.5.1 Beating analysis and 3D spectra

One of the more widely-discussed phenomena observed in two-dimensional spectra is the presence of oscillatory dynamics in the waiting time, caused by coherent superpositions of electronic or vibrational states. A convenient approach to analyzing these oscillations uses a Fourier transform across the waiting time to produce a frequency-frequency-frequency cube sometimes referred to as a 3D spectrum [23, 31]. Fourier transformation over the complex-valued spectrum produces spectra at both positive and negative beating frequencies which contain different information and can be used to identify the source of oscillations based on available Feynman pathways. This approach has been used to identify vibrational motion on both the ground and excited electronic potential energy surface [32] and to distinguish between vibrational and electronic oscillations [23].

Figure 4.5 shows the 3D spectral slices at $\pm$ 550 cm^{-1} for the Cy5 monomer on DNA following the formalism of [23]. Color maps represent spectral power (amplitude squared), and black contours show the real valued absorptive 2D spectrum at a waiting time of 100 fs. Dot spectra correspond to expected positions of beating spectra based on the Feynman pathways shown for each slice.

Of particular interest are the beating patterns corresponding to vibrations on the excited electronic potential energy surface, as these would be expected to change with interchromophore coupling in the dimers. Figure 4.6 shows the two slices that include only excited state oscillatory contributions for the three samples, with each slice independently normalized. As the dyes are brought closer together, coupling increases and beating intensity shifts in all cases from the lower rephasing frequency feature to the higher frequency one. This shift shows clear interactions between the dimer coupling and the 550 cm^{-1} beating, suggesting that this vibration may be involved in the splitting seen in the 0 bp dimer absorption spectrum.

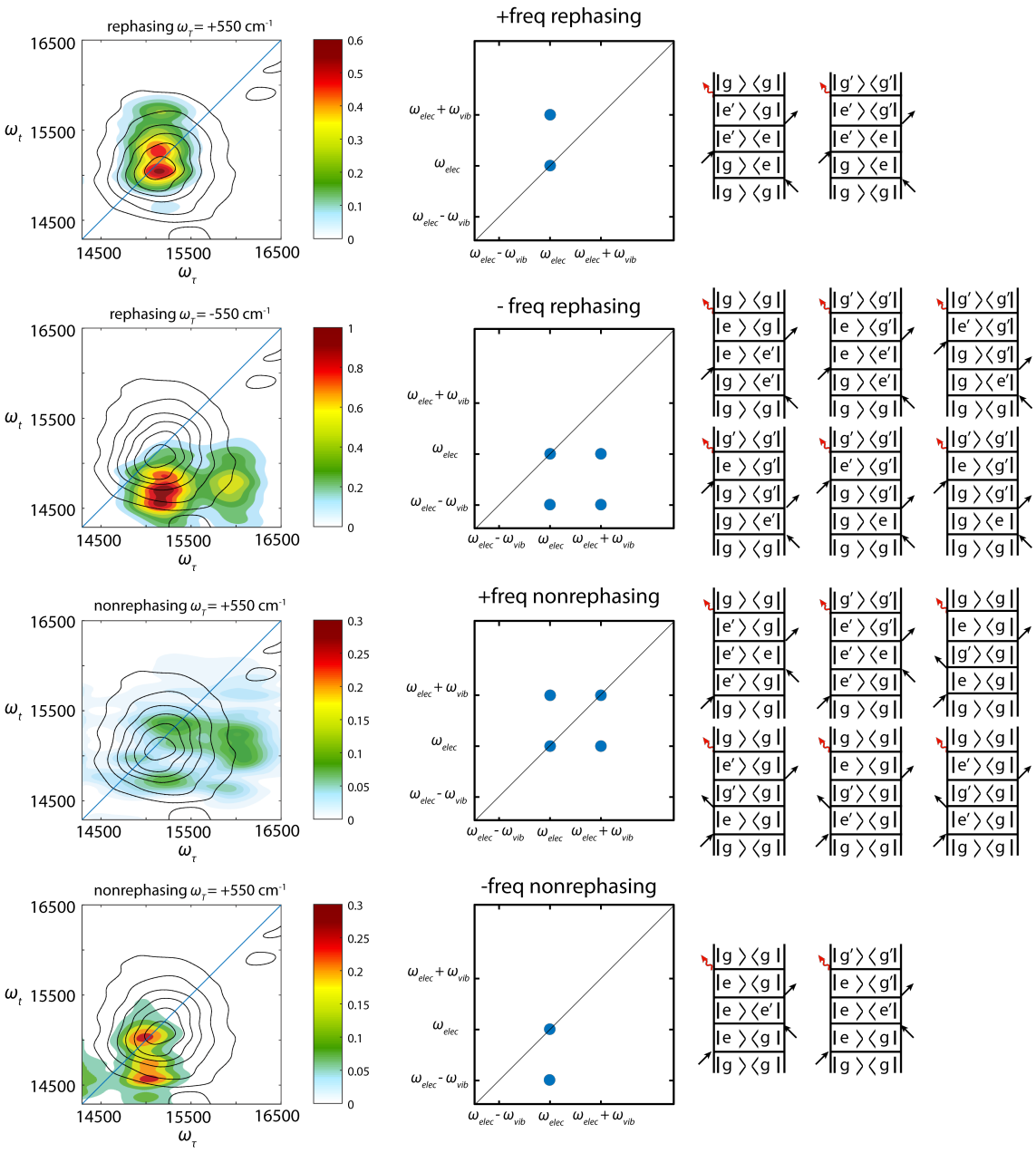

Figure 4.5: 3D spectral slice of Cy5 monomer on DNA at $\pm$ 550 cm^{-1}. Color refers to power spectral intensity, with all four spectra normalized to the same maximum. Contours are of real absorptive 2D at $T = 100$ fs. Dot spectra correspond to locations specified by Feynman diagrams.

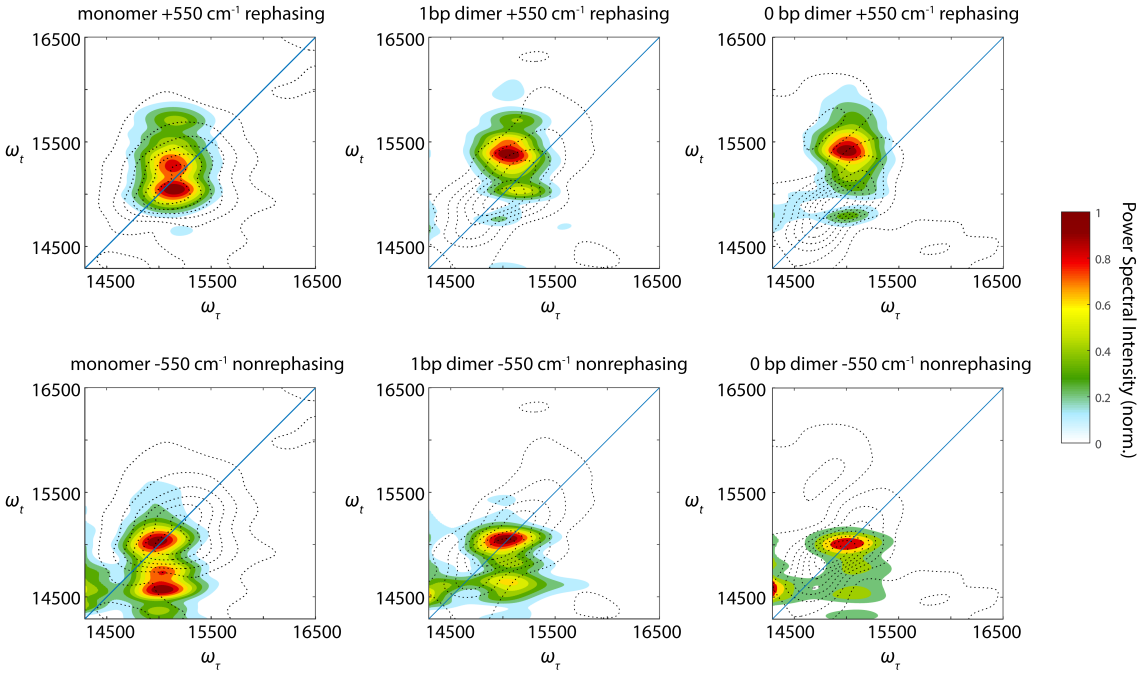

Figure 4.6: Comparison of excited state vibrational pathways between monomers and dimer. Color refers to power spectral intensity, with each spectrum individually normalized. Contours are of real absorptive 2D for the relevant sample at $T = 45$ fs.

4.5.2 Simulation and Modeling of 0 bp dimer

Based on the dipole orientation and distance results from the MD simulation shown in Figure 4.7, we can estimate the coupling using a point-dipole model, where

$$V = \frac{\kappa \mu^2}{4\pi\epsilon_0 n^2 R^3} \tag{4.2}$$

where n is the index of refraction (here using 1.33 for water), R is the interchromophore spacing, and μ is the transition dipole strength, which we can estimate from the linear absorption spectrum of the monomer by integration to a value of approximately 15 Debye. Combining with the MD simulation results of 19.5 Å for the interchromophore spacing R and a κ value of 1, we get a predicted dipole coupling of roughly 75 cm^{-1}.

By contrast, the vibronic model in the lower part of Figure 4.7 is based on a single-mode vibronic model from Cunningham et al. [33], which is in turn based on theoretical work from

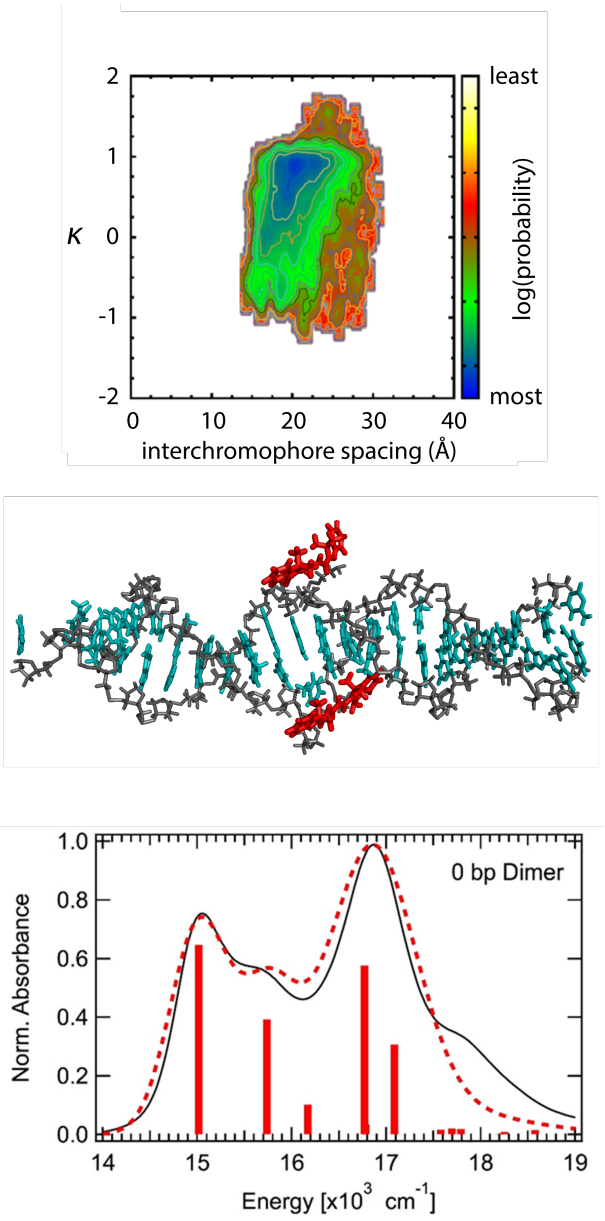

Figure 4.7: Simulation and modeling results for 0 bp dimer. The MD simulation was run for 1 μs using a TIP3 water model and a salt concentration of 350 mM Na^+. Top figure shows log-scaled probability as a function of κ, the dipole orientation factor, and the interchromophore spacing, with blue indicating the higher probability configurations. The middle figure shows a representative configuration near the most likely probability, with dyes in a parallel orientation separated by roughly 19.5 Å. Bottom shows a model of the absorption spectrum using a single-mode vibronic model described in text.

Kuhn, Renger, and May [34]. The model accurately reproduces spectra in Cy3 dimers [33], but even the qualitative reproduction of the spectrum shown here can only be done with significantly stronger coupling (roughly 640 cm^{-1}) with a vibrational mode at 1210 cm^{-1}.

4.6 Conclusions

DNA nanomaterials provide a promising path to manmade light harvesting devices following the design principles from photosynthetic pigment-protein complexes. One important characteristic from photosynthetic complexes is vibronic enhancement of energy transfer, where vibrational motion on the excited state aids in exciton relaxation throughout coupled chromophores. Here, we study a series of cyanine dyes attached to a DNA duplex, and show that a 550 cm^{-1} mode couples to the electronic transition. This vibrational mode matches energetically with a splitting observed in the most closely coupled dimer, and current single-mode models using the higher energy mode near 1200 cm^{-1} cannot reproduce the spectrum with a coupling that is consistent with structural simulations. These observations suggest that a multimode vibronic model incorporating both the high energy mode near 1200 cm^{-1} and the mode at 550 cm^{-1} could more accurately describe the coupling between these dyes. Accurate modeling of vibrational coupling is particularly important in H-type dimers like these, where vibrational interactions are comparable or stronger than electronic interactions.

REFERENCES

[1] Nadrian C. Seeman and Hanadi F. Sleiman. DNA nanotechnology. *Nature Reviews Materials*, 3:17068, 2017.

[2] Florian Praetorius, Benjamin Kick, Karl L. Behler, Maximilian N. Honemann, Dirk Weuster-Botz, and Hendrik Dietz. Biotechnological mass production of DNA origami. *Nature*, 552:84, 2017.

[3] Susan Buckhout-White, Christopher M. Spillmann, W. Russ Algar, Ani Khachatrian, Joseph S. Melinger, Ellen R. Goldman, Mario G. Ancona, and Igor L. Medintz. Assembling programmable FRET-based photonic networks using designer DNA scaffolds. *Nature Communications*, 5:5615, 2014.

[4] Paul D. Cunningham, Ani Khachatrian, Susan Buckhout-White, Jeffrey R. Deschamps, Ellen R. Goldman, Igor L. Medintz, and Joseph S. Melinger. Resonance energy transfer in DNA duplexes labeled with localized dyes. *The Journal of Physical Chemistry B*, 118(50):14555–14565, 2014.

[5] A. Eisfeld and J.S. Briggs. The j- and h-bands of organic dye aggregates. *Chemical Physics*, 324(2):376 – 384, 2006.

[6] Franklin D. Fuller, Jie Pan, Andrius Gelzinis, Vytautas Butkus, S. Seckin Senlik, Daniel E. Wilcox, Charles F. Yocum, Leonas Valkunas, Darius Abramavicius, and Jennifer P. Ogilvie. Vibronic coherence in oxygenic photosynthesis. *Nature Chemistry*, 6:706, 2014.

[7] Gregory D. Scholes, Graham R. Fleming, Lin X. Chen, Alán Aspuru-Guzik, Andreas Buchleitner, David F. Coker, Gregory S. Engel, Rienk van Grondelle, Akihito Ishizaki, David M. Jonas, Jeff S. Lundeen, James K. McCusker, Shaul Mukamel, Jennifer P. Ogilvie, Alexandra Olaya-Castro, Mark A. Ratner, Frank C. Spano, K. Birgitta Whaley,

and Xiaoyang Zhu. Using coherence to enhance function in chemical and biophysical systems. *Nature*, 543:647, 2017.

[8] Gregory S. Engel, Tessa R. Calhoun, Elizabeth L. Read, Tae-Kyu Ahn, Tomáš Mančal, Yuan-Chung Cheng, Robert E. Blankenship, and Graham R. Fleming. Evidence for wavelike energy transfer through quantum coherence in photosynthetic systems. *Nature*, 446:782, 2007.

[9] Gitt Panitchayangkoon, Dugan Hayes, Kelly A. Fransted, Justin R. Caram, Elad Harel, Jianzhong Wen, Robert E. Blankenship, and Gregory S. Engel. Long-lived quantum coherence in photosynthetic complexes at physiological temperature. *Proceedings of the National Academy of Sciences*, 107(29):12766–12770, 2010.

[10] Peter D. Dahlberg, Andrew F. Fidler, Justin R. Caram, Phillip D. Long, and Gregory S. Engel. Energy transfer observed in live cells using two-dimensional electronic spectroscopy. *The Journal of Physical Chemistry Letters*, 4(21):3636–3640, 2013.

[11] Peter D. Dahlberg, Graham J. Norris, Cheng Wang, Subha Viswanathan, Ved P. Singh, and Gregory S. Engel. Communication: Coherences observed *in vivo* in photosynthetic bacteria using two-dimensional electronic spectroscopy. *The Journal of Chemical Physics*, 143(10):101101, 2015.

[12] Jacob C. Dean, Tihana Mirkovic, Zi S. D. Toa, Daniel G. Oblinsky, and Gregory D. Scholes. Vibronic enhancement of algae light harvesting. *Chem*, 1(6):858–872, 2018.

[13] Vivek Tiwari, William K. Peters, and David M. Jonas. Electronic resonance with anticorrelated pigment vibrations drives photosynthetic energy transfer outside the adiabatic framework. *Proceedings of the National Academy of Sciences*, 110(4):1203–1208, 2013.

[14] Aurélia Chenu and Gregory D. Scholes. Coherence in energy transfer and photosynthesis. *Annual Review of Physical Chemistry*, 66(1):69–96, 2015.

[15] Hong-Guang Duan, Valentyn I. Prokhorenko, Richard J. Cogdell, Khuram Ashraf, Amy L. Stevens, Michael Thorwart, and R. J. Dwayne Miller. Nature does not rely on long-lived electronic quantum coherence for photosynthetic energy transfer. *Proceedings of the National Academy of Sciences*, 114(32):8493–8498, 2017.

[16] Margherita Maiuri, Evgeny E. Ostroumov, Rafael G. Saer, Robert E. Blankenship, and Gregory D. Scholes. Coherent wavepackets in the Fenna–Matthews–Olson complex are robust to excitonic-structure perturbations caused by mutagenesis. *Nature Chemistry*, 10:177, 2018.

[17] Elisabet Romero, Vladimir I. Novoderezhkin, and Rienk van Grondelle. Quantum design of photosynthesis for bio-inspired solar-energy conversion. *Nature*, 543:355, 2017.

[18] Dugan Hayes, Graham B. Griffin, and Gregory S. Engel. Engineering coherence among excited states in synthetic heterodimer systems. *Science*, 340(6139):1431–1434, 2013.

[19] Alexei Halpin, Philip J. M. Johnson, Roel Tempelaar, R. Scott Murphy, Jasper Knoester, Thomas L. C. Jansen, and R. J. Dwayne Miller. Two-dimensional spectroscopy of a molecular dimer unveils the effects of vibronic coupling on exciton coherences. *Nature Chemistry*, 6:196, 2014.

[20] Lili Wang, Graham B. Griffin, Alice Zhang, Feng Zhai, Nicholas E. Williams, Richard F. Jordan, and Gregory S. Engel. Controlling quantum-beating signals in 2D electronic spectra by packing synthetic heterodimers on single-walled carbon nanotubes. *Nature Chemistry*, 9:219, 2017.

[21] M. Cipolloni, B. Fresch, I. Occhiuto, P. Rukin, K. G. Komarova, A. Cecconello, I. Willner, R. D. Levine, F. Remacle, and E. Collini. Coherent electronic and nuclear dynamics in a rhodamine heterodimer-DNA supramolecular complex. *Phys. Chem. Chem. Phys.*, 19:23043–23051, 2017.

[22] Étienne Boulais, Nicolas P. D. Sawaya, Rémi Veneziano, Alessio Andreoni, James L. Banal, Toru Kondo, Sarthak Mandal, Su Lin, Gabriela S. Schlau-Cohen, Neal W. Woodbury, Hao Yan, Alán Aspuru-Guzik, and Mark Bathe. Programmed coherent coupling in a synthetic DNA-based excitonic circuit. *Nature Materials*, 17:159, 2017.

[23] Daniel B. Turner, Rayomond Dinshaw, Kyung-Koo Lee, Michael S. Belsley, Krystyna E. Wilk, Paul M. G. Curmi, and Gregory D. Scholes. Quantitative investigations of quantum coherence for a light-harvesting protein at conditions simulating photosynthesis. *Phys. Chem. Chem. Phys.*, 14:4857–4874, 2012.

[24] Sean T. Roberts, Joseph J. Loparo, and Andrei Tokmakoff. Characterization of spectral diffusion from two-dimensional line shapes. *The Journal of Chemical Physics*, 125(8):084502, 2006.

[25] S.H. Sohail, P. D. Dahlberg, M. A. Allodi, P.C. Ting, S.C. Massey, E.C. Martin, C.N. Hunter, and G. S. Engel. Communication: Broad manifold of excitonic states in Light-Harvesting Complex 1 promotes efficient unidirectional energy transfer *in vivo*. *Journal of Chemical Physics*, 147:131101, 2017.

[26] Elad Harel, Andrew F. Fidler, and Gregory S. Engel. Real-time mapping of electronic structure with single-shot two-dimensional electronic spectroscopy. *Proceedings of the National Academy of Sciences*, 107(38):16444–16447, 2010.

[27] Elad Harel, Andrew F. Fidler, and Gregory S. Engel. Single-shot gradient-assisted photon echo electronic spectroscopy. *Journal of Physical Chemistry A*, 115(16):3787–3796, 2011.

[28] Vadim V. Lozovoy, Igor Pastirk, and Marcos Dantus. Multiphoton intrapulse interference: Ultrashort laser pulse spectral phase characterization and compensation. *Opt. Lett.*, 29(7):775–777, 2004.

[29] Marco A. Allodi, John P. Otto, Sara H. Sohail, Rafael G. Saer, Ryan E. Wood, Brian S. Rolczynski, Sara C. Massey, Po-Chieh Ting, Robert E. Blankenship, and Gregory S. Engel. Redox conditions affect ultrafast exciton transport in photosynthetic pigment-protein complexes. *The Journal of Physical Chemistry Letters*, 9(1):89–95, 2018.

[30] Tobias Brixner, Tomáš Mančal, Igor V. Stiopkin, and Graham R. Fleming. Phase-stabilized two-dimensional electronic spectroscopy. *The Journal of Chemical Physics*, 121(9):4221–4236, 2004.

[31] Dugan Hayes and Gregory S. Engel. Extracting the excitonic hamiltonian of the Fenna-Matthews-Olson complex using three-dimensional third-order electronic spectroscopy. *Biophysical Journal*, 100(8):2043–2052, 2011.

[32] Justin R. Caram, Andrew F. Fidler, and Gregory S. Engel. Excited and ground state vibrational dynamics revealed by two-dimensional electronic spectroscopy. *The Journal of Chemical Physics*, 137(2):024507, 2012.

[33] Paul D. Cunningham, Young C. Kim, Sebastián A. Díaz, Susan Buckhout-White, Divita Mathur, Igor L. Medintz, and Joseph S. Melinger. Optical properties of vibronically coupled Cy3 dimers on DNA scaffolds. in review, 2018.

[34] Oliver Kühn, Thomas Renger, and Volkhard May. Theory of exciton-vibrational dynamics in molecular dimers. *Chemical Physics*, 204(1):99 – 114, 1996.

CHAPTER 5

FUTURE DIRECTIONS

5.1 DNA nanostructures as a scalable approach to ultrafast energy transfer

In chapter 4, I use two-dimensional electronic spectroscopy to explore the vibronic nature of a cyanine homodimer attached to DNA, highlighting how a vibronic coupling model using only a single mode does not accurately describe the system. Here, I will discuss some of the further-reaching goals of the study of dyes attached to DNA templates, and describe future lanes of investigation that can aid in reaching these goals. These proposed projects draw not just upon the work performed in chapter 4, but provide a path to follow up the findings of chapters 2 and 3, which also investigated how the chemical structure surrounding chromophores determines their electronic and optical characteristics.

The primary step in photosynthesis is light harvesting, almost universally through some form chlorophyll or bacteriochlorophyll containing antenna complex. These complexes are arranged around some form of photoenzyme, which uses the light energy to produce some longer-lived form of energy storage, typically chemical in nature [1]. What is particularly remarkable about photosynthetic antenna complexes is the degree to which biology has developed a wide variety of highly efficient light harvesters with only a few base molecules - mainly chlorophylls and carotenoids [2]. By arranging these molecules in closely-packed, highly controlled orientations, proteins couple these few chromophores together to create a wide array of exciton configurations with useful optical properties, such as large absorption cross sections and efficient ultrafast energy transfer through electronic delocalization [3].

Designing a manmade light harvesting antenna in the style of a pigment-protein complex requires both a high degree of structural control on the scale of individual chromophores and a convenient pathway to larger-scale production. One route to such an antenna is through the use of DNA nanotechnology. The "programmable" nature of DNA enables the construction

of large scale structures composed of many individual building blocks, including the creation of complex three-dimensional shapes [4, 5]. Small scale control of DNA assembly can lead to rigid blocks [6], which may provide rigidity comparable to the protein backbone in existing photosynthetic compexes. In fact, recent work has shown the viability of DNA to control the creation of chromophore aggregates for the purposes of enhanced energy transfer [7]. Combined with modern bacteriophage-based synthesis techniques that allow for large scale generation of DNA origami structures [8], this molecular-level control could lead to new light harvesting materials that rival those made by biology.

5.1.1 Approaches to light-harvesting building blocks in DNA

A number of approaches to designing energy transfer in DNA-based light harvesting strucutres have been demonstrated. By far the most common are approaches that make use of Förster Resonance Energy Transfer (FRET) [9]. FRET describes well the transfer between the individual antenna complexes that compose larger photosynthetic units [1] and the ability to carefully control FRET through DNA structures is an important step in the development of DNA-based light harvesting. The use of DNA structuring in multiple dimensions allows for multiple FRET pathways, increasing transfer efficiency [10] and, through the use of multiple donors, enhancing the number of excitations that can reach a given point [11]. Through the use of multiple transfer steps, an absorbed exciton can be transferred through space via the use of "photonic wires" composed of repeating chromophores [12].

The photonic wire approach offers a convenient platform for the study of energy transfer through multiples of the same dye, allowing optimization of a small light harvesting component. An example can be seen in Figure 5.1, which illustrates a key finding from these "homo-FRET" studies [12]. Here, a 20 base pair DNA strand has a donor (Pacific Blue) and acceptor (Cy3) attached to its two ends, with varying amounts of the intercalating dye oxazole yellow (YO) used to facilitate energy transfer. YO selectively intercalates non-cooperatively in a nearest-neighbor exclusion pattern [13], and is not fluorescent in aqueous

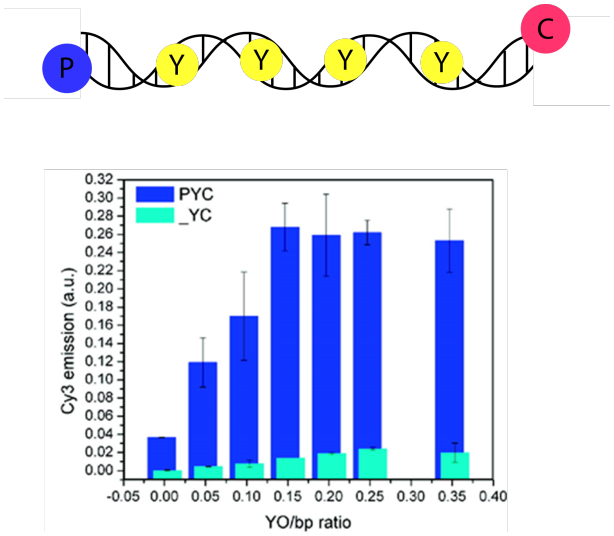

Figure 5.1: Relationship between chromophore density and transfer efficiency. A study on a donor-transmitter-acceptor DNA wire (*top*) was performed with varying concentrations of the intermediate dye oxazole yellow. Transfer efficiency (*bottom*) at first increases with dye concentration, but levels off due to competing interactions. Figure adapted from [12], used with permission.

solution, although it fluoresces while intercalated or in high-viscosity solvents [14]. As the graph in the figure shows, transfer efficiency from the donor to acceptor in this wire is small with no YO added, and efficiency at first increases with YO density, but levels off after a certain threshold is reached. This saturation behavior is driven by competing factors; for example, smaller interchromophore distances mean more efficient transfer per step, but also more steps from donor to acceptor. In the case of YO intercalation, high concentrations may lead to alternative binding modes that are less conducive to energy transfer [12]. These observations drive home the importance of local environment control around chromophores in the design of light harvesting and energy transfer units in DNA-dye nanostructures.

Of particular interest in light harvesting is the ability to use strongly-coupled chromophores to take advantage of delocalized exciton states and the possibility of coherent energy transfer [16]. Ever since it was observed in a photosynthetic complex just over a decade ago [17], significant progress has been made in the development of synthetic systems that show signs of coherence [18] and our understanding of design principles that enable co-

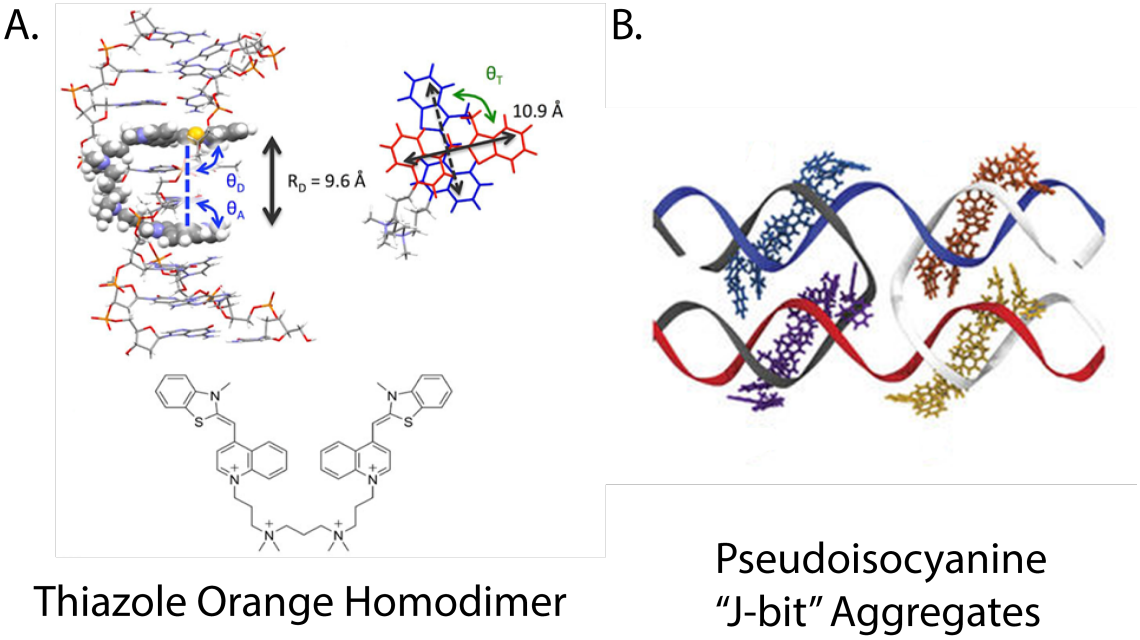

Figure 5.2: Intercalating Dye Considerations. A.) Intercalating dimers such as the thiazole orange dimer provide some potential for well-controlled energy transfer, but current designs have dyes coupled at an orientation leading to weak coupling. B.) Self-assembled aggregates in the DNA groove, here composed of pseudoisocyanine, may provide a path towards efficient transfer through the use of delocalized excitons. Additionally, brick-like DNA structures like the one shown here may allow for more favorable orientations of intercalated dimers by binding each chromophore to a different strand. Figures adapted from [15] and [7], used with permission.

herent transfer [19]. Current understanding of coherent transfer is that it requires a resonant vibration that matches the gap between electronic states and that chromophores must be held somewhat rigidly (must share a vibrational environment).

Progress has been made in creating DNA-templated aggregates that show promise for coherent transport [20, 21, 22] including structures with FRET between aggregates[7]. A potential path to designing coherent transport in DNA aggregates is through the use of intercalating dyes such as oxazole yellow [12] or thiazole orange [15] as these are held in well-defined orientations by the DNA helix.

A description of two potential control schemes for DNA intercalating dyes is seen in Figure 5.2. Previous work by Cunningham et al. at the Naval Research Lab (NRL) [15] has shown that coupling between the thiazole orange homodimer TOTO is limited by an unfavorable dipole orientation when intercalated into a standard dsDNA helix. A potential path towards the development of a more favorable dye orientation are shown in part B, where pseudoisocyanine aggregates, which have delocalized excitons and large transition dipoles, are used in place of single dyes in an energy transfer scheme [7]. While the assembly of small aggregates in this manner shows promise, another possibility is the use of "brick-like" DNA structures such as this one or the ones described in [6] with intercalating dimers such as TOTO. TOTO preferentially binds between specific base pair combinations over others, so structures could be designed that drive intercalation across multiple helices, allowing for greater control over dipole orientations as a path towards stronger coupling in a rigidly held orientation. This design, or more likely variants using heterodimers with tuned energy gaps to match with local vibrations, may lead to coherent interactions that will enhance energy transfer.

5.2 Nonlinear Spectroscopy as a Light-Harvesting Design Tool

5.2.1 Two-dimensional spectroscopy as a quantification of coupling

Engineering new systems for light harvesting requires detailed characterization of electronic structure and dynamics. To determine which light-harvesting building blocks are sufficiently promising to incorporate into larger structures, we require an experimental measurement of relevant properties such as exciton delocalization, structural and energetic inhomogeneity, and inter-exciton coupling. Throughout this dissertation, I have shown how nonlinear spectroscopy, and in particular two-dimensional electronic spectroscopy, has this characterization capability. In particular, the ability of two-dimensional spectroscopy to quantify vibrational, vibronic, and electronic interactions [23, 24] will be vital to the engineering process.

An initial expansion of reported work is the measurement of vibronic interactions in closely-bound cyanine heterodimers, such as the Cy5-Cy5.5 dimer described in figure 5.3, where dyes are attached on opposite sides of a dsDNA strand. This dimer represents a part of a series of heterodimers used as a direct follow-up to the work performed in Chapter 4 on Cy5 homodimers, simply replacing one of the Cy5 dyes with the red-shifted Cy5.5. Compared to the homodimers, where no net energy transfer is expected, here we may be able to observe interchromophore exciton transport as a function of base pair separation. These dimers will also allow an opportunity to test our claims about vibronic coupling in the homodimers. Similar to the homodimers, preliminary 2D data of the 0 bp Cy5-Cy5.5 heterodimer shows strong oscillatory behavior, although here the strongest oscillation occurs at 300 cm^{-1} rather than the 550 cm^{-1} beating seen previously. This difference likely arises from the additional aromatic ring structures present in Cy5.5. Investigations of these oscillations and of population transfer dynamics in this and other similar heterodimers are ongoing.

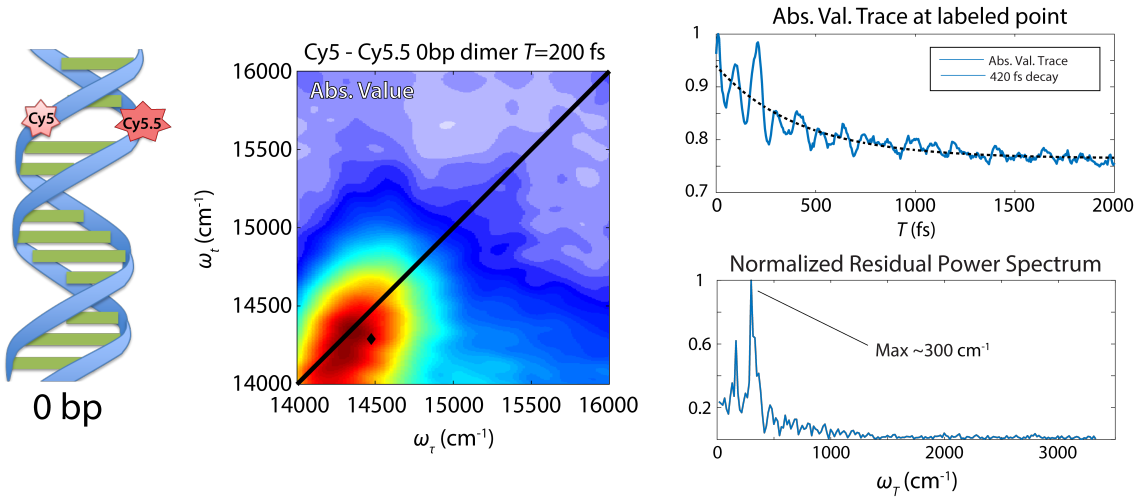

Figure 5.3: Preliminary Heterodimer 2DES shows oscillatory dynamics.

5.2.2 Polarization control provides structural information

Experiments that use controlled polarization of light can inform on relative orientations of transition dipoles, enabling detailed assignment of spectral signals and providing detailed structural information. The use of an XXYY polarization scheme, where pulses 3 and 4 have a polarization orthogonal to that of pulses 1 and 2, can be combined with the typical all-parallel polarization scheme in two dimensional spectroscopy to measure 2D anisotropy, incorporating the structural insights from pump-probe anisotropy and the electronic information provided by 2DES. This technique has been demonstrated with chemical [25] and materials [26] systems, and more recently was used by the Engel group to track the orientation of excited states in a photosynthetic antenna complex [27]. Anisotropy could be a particularly useful measurement in the study of covalently linked cyanine dimers, such as those described in Figure 5.3 and in Chapter 4, where there is believed to be a distribution of dipoles [28] but this distribution has not been experimentally measured. 2D anisotropy would enable the observation of sub-ensembles within this distribution, allowing a direct comparison of differing geometries and their role on energy transfer. In the intercalated dye samples, anisotropy can aid in the structural characterization and provide a quantitative measure of the rigidly held dipole orientations required for coherent interactions.

Chirality of dipole orientations leads to a further use of polarization to explore structural contributions to energy transfer. Because DNA is itself chiral, many of the aggregates constructed as light-harvesting building blocks are chiral as well. Chiral chromophore structures respond differently to left and right circularly polarized light, and previous work in the Engel group has shown the ability to track localization of an intially delocalized excitation through the use of chiral 2DES [29]. Similar studies on DNA-templated chiral aggregates could help determine the spatial extent of delocalization and energy transfer, further enabling the engineering of novel light-harvesting designs.

REFERENCES

[1] Robert E. Blankenship. *Molecular Mechanisms of Photosynthesis*. Wiley/Blackwell, Chichester, West Sussex, second edition, 2014.

[2] Gregory D. Scholes, Graham R. Fleming, Alexandra Olaya-Castro, and Rienk van Grondelle. Lessons from nature about solar light harvesting. *Nature Chemistry*, 3:763, 2011.

[3] Francesca Fassioli, Rayomond Dinshaw, Paul C. Arpin, and Gregory D. Scholes. Photosynthetic light harvesting: excitons and coherence. *Journal of The Royal Society Interface*, 11(92), 2014.

[4] Nadrian C. Seeman and Hanadi F. Sleiman. DNA nanotechnology. *Nature Reviews Materials*, 3:17068, 2017.

[5] Rémi Veneziano, Sakul Ratanalert, Kaiming Zhang, Fei Zhang, Hao Yan, Wah Chiu, and Mark Bathe. Designer nanoscale DNA assemblies programmed from the top down. *Science*, 352(6293):1534–1534, 2016.

[6] Matthew R. Jones, Nadrian C. Seeman, and Chad A. Mirkin. Programmable materials and the nature of the DNA bond. *Science*, 347(6224), 2015.

[7] Étienne Boulais, Nicolas P. D. Sawaya, Rémi Veneziano, Alessio Andreoni, James L. Banal, Toru Kondo, Sarthak Mandal, Su Lin, Gabriela S Schlau-Cohen, Neal W Woodbury, Hao Yan, Alán Aspuru-Guzik, and Mark Bathe. Programmed coherent coupling in a synthetic DNA-based excitonic circuit. *Nature Materials*, 17:159, 2017.

[8] Florian Praetorius, Benjamin Kick, Karl L. Behler, Maximilian N Honemann, Dirk Weuster-Botz, and Hendrik Dietz. Biotechnological mass production of DNA origami. *Nature*, 552:84, 2017.

[9] Susan Buckhout-White, Christopher M. Spillmann, W. Russ Algar, Ani Khachatrian, Joseph S. Melinger, Ellen R. Goldman, Mario G. Ancona, and Igor L. Medintz. As-

sembling programmable FRET-based photonic networks using designer DNA scaffolds. *Nature Communications*, 5:5615, 2014.

[10] Joseph S. Melinger, Ani Khachatrian, Mario G. Ancona, Susan Buckhout-White, Ellen R. Goldman, Christopher M. Spillmann, Igor L. Medintz, and Paul D. Cunningham. Fret from multiple pathways in fluorophore-labeled dna. *ACS Photonics*, 3(4):659–669, 2016.

[11] Elisa A. Hemmig, Celestino Creatore, Bettina Wünsch, Lisa Hecker, Philip Mair, M. Andy Parker, Stephen Emmott, Philip Tinnefeld, Ulrich F. Keyser, and Alex W. Chin. Programming light-harvesting efficiency using DNA origami. *Nano Letters*, 16(4):2369–2374, 2016.

[12] Jonas K. Hannestad, Peter Sandin, and Bo Albinsson. Self-assembled DNA photonic wire for long-range energy transfer. *Journal of the American Chemical Society*, 130(47):15889–15895, 2008.

[13] Anette Larsson, Christina Carlsson, Mats Jonsson, and Bo Albinsson. Characterization of the binding of the fluorescent dyes YO and YOYO to DNA by polarized light spectroscopy. *Journal of the American Chemical Society*, 116(19):8459–8465, 1994.

[14] Christina Carlsson, Anette Larsson, Mats Jonsson, Bo Albinsson, and Bengt Norden. Optical and photophysical properties of the oxazole yellow DNA probes YO and YOYO. *The Journal of Physical Chemistry*, 98(40):10313–10321, 1994.

[15] Paul D. Cunningham, William P. Bricker, Sebastián A. Díaz, Igor L. Medintz, Mark Bathe, and Joseph S. Melinger. Optical determination of the electronic coupling and intercalation geometry of thiazole orange homodimer in DNA. *The Journal of Chemical Physics*, 147(5):055101, 2017.

[16] Gregory D. Scholes, Graham R. Fleming, Lin X. Chen, Alán Aspuru-Guzik, Andreas Buchleitner, David F. Coker, Gregory S. Engel, Rienk van Grondelle, Akihito Ishizaki,

David M. Jonas, Jeff S. Lundeen, James K. McCusker, Shaul Mukamel, Jennifer P. Ogilvie, Alexandra Olaya-Castro, Mark A. Ratner, Frank C. Spano, K. Birgitta Whaley, and Xiaoyang Zhu. Using coherence to enhance function in chemical and biophysical systems. *Nature*, 543:647, 2017.

[17] Gregory S. Engel, Tessa R. Calhoun, Elizabeth L. Read, Tae-Kyu Ahn, Tomáš Mančal, Yuan-Chung Cheng, Robert E. Blankenship, and Graham R. Fleming. Evidence for wavelike energy transfer through quantum coherence in photosynthetic systems. *Nature*, 446:782, 2007.

[18] Dugan Hayes, Graham B. Griffin, and Gregory S. Engel. Engineering coherence among excited states in synthetic heterodimer systems. *Science*, 340(6139):1431–1434, 2013.

[19] Lili Wang, Graham B. Griffin, Alice Zhang, Feng Zhai, Nicholas E. Williams, Richard F. Jordan, and Gregory S. Engel. Controlling quantum-beating signals in 2D electronic spectra by packing synthetic heterodimers on single-walled carbon nanotubes. *Nature Chemistry*, 9:219, 2017.

[20] Hiroyuki Asanuma, Taiga Fujii, Tomohiro Kato, and Hiromu Kashida. Coherent interactions of dyes assembled on DNA. *Journal of Photochemistry and Photobiology C: Photochemistry Reviews*, 13(2):124 – 135, 2012.

[21] Markus Probst, Simon M. Langenegger, and Robert Haner. A modular LHC built on the DNA three-way junction. *Chem. Commun.*, 50:159–161, 2014.

[22] Brittany L. Cannon, Donald L. Kellis, Lance K. Patten, Paul H. Davis, Jeunghoon Lee, Elton Graugnard, Bernard Yurke, and William B. Knowlton. Coherent exciton delocalization in a two-state DNA-templated dye aggregate system. *The Journal of Physical Chemistry A*, 121(37):6905–6916, 2017.

[23] V. P. Singh, M. Westberg, C. Wang, P. D. Dahlberg, T. Gellen, A. T. Gardiner, R. J. Cogdell, and G. S. Engel. Towards quantification of vibronic coupling in photosynthetic antenna complexes. *The Journal of Chemical Physics*, 142(21):212446, 2015.

[24] Daniel B. Turner, Rayomond Dinshaw, Kyung-Koo Lee, Michael S. Belsley, Krystyna E. Wilk, Paul M. G. Curmi, and Gregory D. Scholes. Quantitative investigations of quantum coherence for a light-harvesting protein at conditions simulating photosynthesis. *Phys. Chem. Chem. Phys.*, 14:4857–4874, 2012.

[25] Joshua S. Ostrander, Robert Knepper, Alexander S. Tappan, Jeffrey J. Kay, Martin T. Zanni, and Darcie A. Farrow. Energy transfer between coherently delocalized states in thin films of the explosive pentaerythritol tetranitrate (PETN) revealed by two-dimensional infrared spectroscopy. *The Journal of Physical Chemistry B*, 121(6):1352–1361, 2017.

[26] Randy D. Mehlenbacher, Jialiang Wang, Nicholas M. Kearns, Matthew J. Shea, Jessica T. Flach, Thomas J. McDonough, Meng-Yin Wu, Michael S. Arnold, and Martin T. Zanni. Ultrafast exciton hopping observed in bare semiconducting carbon nanotube thin films with two-dimensional white-light spectroscopy. *The Journal of Physical Chemistry Letters*, 7(11):2024–2031, 2016.

[27] Sara C. Massey, Po-Chieh Ting Shu-Hao Yeh, Peter D. Dahlberg, Sara H. Sohail, Marco A. Allodi, Elizabeth C. Martin, C. Neil Hunter, Sabre Kais, and Gregory S. Engel. Orientational dynamics of transition dipoles and exciton relaxation in LH2 from ultrafast two-dimensional anisotropy. in preparation.

[28] Paul D. Cunningham, Young C. Kim, Sebastián A. Díaz, Susan Buckhout-White, Divita Mathur, Igor L. Medintz, and Joseph S. Melinger. Optical properties of vibronically coupled Cy3 dimers on DNA scaffolds. in review, 2018.

[29] Andrew F. Fidler, Ved P. Singh, Phillip D. Long, Peter D. Dahlberg, and Gregory S. Engel. Dynamic localization of electronic excitation in photosynthetic complexes revealed with chiral two-dimensional spectroscopy. *Nature Communications*, 5:3286, 2014.

CHAPTER 6

CONCLUSIONS

Light harvesting plays a fundamental role in the sustenance of nearly all life on earth, and will need to play an increasing role in human energy generation in the coming decades. From bulk power generation to portable, low energy devices, sunlight provides an ample source of energy that greatly exceeds our needs, so long as we can make use of it. In an effort to enable better designs for light harvesting materials, I have spent the course of my degree investigating the role played by the chromophore environment in ultrafast electron dynamics. This study has ranged from observations of existing biological light harvesting complexes to detailed characterizations of novel structures designed to mimic biology, in all cases using nonlinear spectroscopy as a probe of intrachromophore interactions.

I have focused my research on the following questions:

1. What can biology teach us about the design of robust, self-moderating light harvesting?

2. How does nuclear motion within a chromophore affect energy transfer?

3. Can we use nuclear motion as a tool to enhance electronic interactions?

In order to explore these questions, I worked with scientists from a number of institutions, drawing on the expertise of others in protein growth and molecular synthesis, with my own contribution being the spectroscopic investigations I describe in chapters 2 through 4. In order to aid in understanding of the material in the research chapters, the first chapter in this thesis provides the background and context relevant to my work.

In chapter 1, I introduced two commonly referenced limits to energy transfer theory: point-dipole coupling as described by Förster resonance energy transfer (FRET), and relaxation of delocalized excitons as described in Redfield theory. Energy transfer through the Fenna-Matthews-Olson (FMO) complex, described in chapter 2, is closer to the Redfield limit, while the work described in chapters 3 and 4 examine the edges of where the FRET

approximations provide an accurate description of transfer. The goal of the experiments proposed in chapter 5 is to move the interactions measured in chapter 4 closer to the Redfield regime.

Chapter 1 also describes the response function and Feynman diagram approaches to understanding two-dimensional electronic spectroscopy, a tool used throughout this work to probe electron dynamics. Additionally, it explains two different experimental approaches to 2D spectroscopy, one using a BOXCARS geometry with three controlled time delays, and one that uses a geometric gradient to record 2D spectra in a single shot.

The first of my research questions is addressed in Chapter 2, which explores a potential photoprotection mechanism in the FMO pigment protein complex from *C. tepidum*. Branching out from a previous study that had seen evidence for redox-sensitive changes to the electronic structure of the complex, I used 2DES to measure how redox affected ultrafast energy transfer in both wild-type and mutant complexes. We hypothesized that the redox changes would affect the coupling between excitons, leading to faster, more efficient energy transfer in the anoxygenic samples compared to those that had been oxygen exposed. This hypothesis was confirmed by our results, but a second result was unexpected: In the previous work, removal of cysteine residues effectively removed oxygen sensitivity, but we found that on an ultrafast timescale there were still significant differences in dynamics based on the presence or absence of oxygen. This difference was traced to a series of tyrosine and tryptophan residues in a structure known to move charges in and out of the active site of redox enzymes, but which had not been previously observed in photosynthetic antenna complexes. As a result, this study led to two key answers to the first question:

- Reduction potential of structures surrounding chromophores can be used to tune chromopohre coupling, and therefore energy transfer.
- Just as we hope to take lessons from biology to build better light harvesting systems, biology adopts structural motifs from redox enzymes to help regulate energy transfer in an antenna complex.

My second question was slightly more applied, and as such required a test system designed with our experiment in mind. My collaborators and I used a pair of modified BODIPY dyes attached to a cavitand molecular switch, which changed between two configurations based on temperature. This configurational switch was used to control the orientation and spacing of the donor and acceptor dyes. Comparison of the ultrafast dynamics with those expected from FRET theory informed on how nuclear motion affects energy transfer in this system. Using 2DES and decay-associated 2D spectra, I was able to separate energy transfer dynamics from internal vibrational relaxation on the donor as well as a third pathway caused by a restriction on energy transfer due to dipole orientation. At least in this case, I found the answer to my question to be that vibrational motion provides a population sink that depletes transfer. In doing so, I also highlighted a potential source of significant error in the lifetime-based FRET measurements common in microscopy.

After seeing how vibrational motion served as competition to energy transfer in the cavitand system, I wanted to explore how it could be used instead to aid in intermolecular coupling and transfer. Vibronic coupling is known to be especially strong in H-aggregates, so in chapter 4, I explored vibronic interactions in a set of cyanine homodimers attached to DNA such that they form an H-dimer configuration. As discussed further in Chapter 5, DNA nanotechnology provides a promising path towards manmade light harvesting systems that closely mimic those present in photosynthesis, but fundamental details relating to chromophore-chromophore and chromophore-environment interactions have yet to be determined. Here, I observed how interchromophore coupling interacts with intrachromophore vibrational-electronic coupling, and showed that a single-vibration model cannot accurately reproduce the optical spectra without electronic coupling far beyond that expected based on structural simulations. A deep understanding of how vibrations affect interchromophore electronic coupling in cyanines and similar vibronic dyes is a required step in the design of light harvesting systems that make use of these dyes, and this work represents a step along the path to that understanding.

While I was able to observe (in Chapter 4) effects of vibrational motion on the electronic coupling, I have not yet fully answered my third question. With that in mind, chapter 5 describes a path for future research, where I believe we can show clear enhancement of energy transfer through the use of vibronic coupling. The ideas presented in this chapter combine the lessons learned about environmental effects on energy transfer and vibronic interactions in an effort to build novel light harvesting devices that mimic photosynthesis. Expanding from the work presented in Chapters 2-4, I propose that DNA nanostructures can be used to take advantage of exciton delocalization for rapid, efficient energy transfer in manmade light harvesting devices. In particular, I imagine the role of the Engel group as leading the design and evaluation of small building blocks to be incorporated in larger structures. While initial studies have been performed with cyanine dyes doubly linked to the phosphate backbone of dsDNA, I believe that the most promising approaches for delocalized excitons and coherent transfer are ones that make use of intercalation and guided aggregation. These systems would be a close manmade analog to light harvesting pigment-protein complexes present in many photosynthetic organisms, and would provide an opportunity to apply the lessons learned here and in other work on the design principles of light harvesting in photosynthesis.

My work shows that the electronic environment around chromophores can be used to control energy transfer. I also found that vibrational motion can compete with energy transfer by depleting excited state populations. In a quest to use vibrations to enhance transfer, I determined that multiple modes play a role in H-type vibronic coupling, and I have proposed future work that I hypothesize will lead to coherent vibronic transport in DNA nanostructures. Overall, my work has shown the significant effects that the environment surrounding chromophores can have on their ultrafast electronic dynamics, and that by taking an example from how biology reuses structural motifs in varied environments, we can use lessons from these systems to build robust, efficient light harvesting devices.